Models for Assessment of Flaws in Pressure Tubes of CANDU Reactors

by

Anup Kumar Sahoo

A thesis
presented to the University of Waterloo
in fulfilment of the
thesis requirement for the degree of
Doctor of Philosophy
in
Civil Engineering

Waterloo, Ontario, Canada, 2009

Author's declaration

I hereby declare that I am the sole author of this thesis. This is a true copy of the thesis, including any required final revisions, as accepted by my examiners.

I understand that my thesis may be made electronically available to the public.

Abstract

Probabilistic assessment and life cycle management of engineering components and systems in a nuclear power plant is intended to ensure safe and efficient operation of energy generation over its entire life. The CANDU reactor core consists of 380-480 pressure tubes, which are like miniature pressure vessels that contain natural uranium fuel. Pressure tubes operate under severe temperature and radiation conditions, which result in degradation with ageing. Presence of flaws in a pressure tube makes it vulnerable to delayed hydride cracking (DHC), which may lead to rupture or break-before-leak situation. Therefore, assessment of flaws in the pressure tubes is considered an integral part of a reactor core assessment program. The main objective of the thesis is to develop advanced probabilistic and mechanical stress field models for the assessment of flaws.

The flaw assessment models used by the industries are based on deterministic upper/lower bound values for the variables and they ignore uncertainties associated with system parameters. In this thesis, explicit limit state equations are formulated and first order reliability method is employed for reliability computation, which is more efficient than simulation-based methods. A semi-probabilistic approach is adopted to develop an assessment model, which consists of a mechanics-based condition (or equation) involving partial factors that are calibrated to a specified reliability level. This approach is applied to develop models for DHC initiation and leak-before-break assessments. A novel feature of the proposed method is that it bridges the gap between a simple deterministic analysis and complex simulations, and it is amenable to practical applications.

The nuclear power plant systems are not easily accessible for inspection and data collection due to exposure to high radiation. For this reason, small samples of pressure tubes are inspected at periodic intervals and small sample of data so collected are used as input to probabilistic analysis. The pressure tube flaw assessment is therefore confounded by large sampling uncertainties. Therefore, determination of adequate sample size is an important issue. In this thesis, a risk informed approach is proposed to define sample size requirement for flaw assessment.

Notch-tip stress field is a key factor in any flaw assessment model. Traditionally, linear elastic fracture mechanics (LEFM) and its extension, serves the basis for determination of notch-tip stress field for elastic and elastic-perfectly-plastic material, respectively. However, the LEFM solution is based on small deformation theory and fixed crack geometry, which leads to singular stress and strain field at the crack-tip. The thesis presents new models for notch and crack induced stress fields based on the deformed geometry. In contrast with the classical solution based on small

deformation theory, the proposed model uses the Cauchy's stress definition and boundary conditions which are coupled with the deformed geometry. This formulation also incorporates the rotation near the crack-tip, which leads to blunting and displacement of the crack-tip. The solution obtained based on the final deformed configuration yields a non-singular stress field at the crack-tip and a non-linear variation of stress concentration factor for both elastic and elastic-perfectly-plastic material.

The proposed stress field formulation approach is applied to formulate an analytical model for estimating the threshold stress intensity factor (K_{IH}) for DHC initiation. The analytical approach provides a relationship between K_{IH} and temperature that is consistent with experimental results.

Acknowledgments

I would like to express my sincere gratitude to my supervisor, Professor Mahesh D. Pandey, for his constant guidance, refreshing encouragement and financial supports throughout my doctorate program. His constructive criticism has helped me grow professionally. I always admire his simplicity and clarity in expressing his thoughts while preparing a technical document. Without his help the thesis could not have completed.

I wish to express my greatest gratitude to Professor R. N. Dubey and Professor J. C. Thompson for sharing their knowledge with me. They helped me constantly in understanding the fundamentals of stress analysis. Without them I would still have been struggling in some basic stress analysis concepts.

I would like to extent my thanks to the committee members Prof. W. C. Xie, Prof. S. Potapenko and Prof. Hamid Jahed for their constructive criticism and suggestions during the course of my thesis.

I would like to offer my special thanks to my friends and colleagues; Alok Mishra, Ying An, Min Wang, Suresh V. Datla, Xianxin Yuan, Guru Prakash, Arun Viramany and lately, Sushanta bhai and Punam bhauja without them my stay in Waterloo wouldn't be enjoyable and memorable.

I am greatly indebted to my father Mr. Dibakar Sahoo, father-in-law Mr. Prahallad Sahoo, mother-in-law Ms. Sukanti Sahoo, and my wife Saswatee for their tremendous patience, love, support and encouragement during my thesis preparation. Also special thanks to my brothers, sister and sister-in-law, for their constant support, affection and encouragement.

Dedicated To My Parents
Mr. Dibakar Sahoo and Late Smt. Ratimani Sahoo

Contents

List of Figures

List of Tables

Chapter 1

Introduction

1.1 Background

Reliable infrastructure systems such as communication systems, transportation systems, energy transmission systems, nuclear power systems etc. are key components for the success and advancement of human society. As service time progresses these systems deteriorates and hence its serviceability, efficiency and reliability decreases. The aging and deterioration of these infrastructure systems has an adverse effect to the safety and economy of the society. For example, consider a nuclear power generation industry. The nuclear industry is, at present, at a crucial juncture, where it has to decide about the future of the first generation of nuclear plants, which are approaching the end of their licensed service life (figure 1.1). Operating experience has shown that ineffective control of the aging degradation of the major Nuclear Power Plant (NPP) components (caused by unanticipated phenomena and by operating, maintenance, design or manufacturing errors) can jeopardize plant safety and also plant life (IAEA 2001). In Canada particularly, nuclear industries are plan-

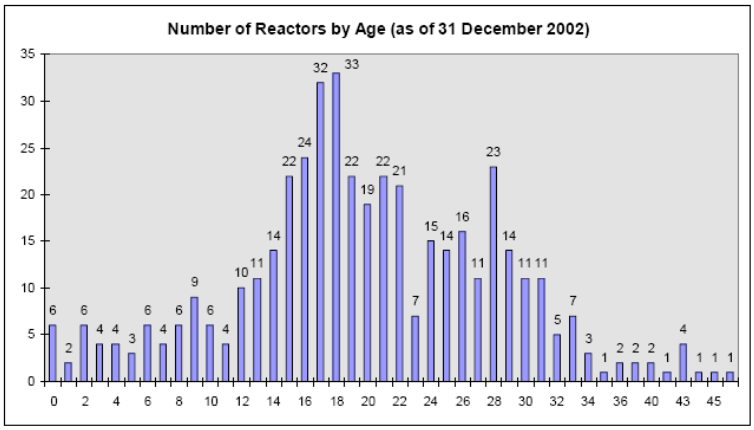

Figure 1.1: Worldwide population of NPPs by age from Start of operation

ning for large scale refurbishment programs to replace or upgrade the deteriorated systems, structures and components. Long term experience and new advances have established the possibility of to extending the life of nuclear power plants beyond their initially licensed life by another 20-30 years. Life extension is considered to bridge the gap between ageing and new plants. NPPs are capital intensive and therefore extension of their operating life will provide a very significant advantage. Extending the operating life of existing NPPs will help to reduce the short term need for new generating capacity without new capital costs. However, these extensions must take place in the context of careful safety analysis and monitoring of equipment ageing concerns.

Aging in the NPPs must therefore be effectively assessed to ensure the availability of design functions throughout the plant service life. From the safety perspective, it has to be demonstrated that adequate safety margins (i.e. integrity and functional capability) remain in excess of minimum safety requirements. To achieve target reliability while designing an engineering system and maintain high performance during its whole service life, engineers rely heavily upon the modern tools

like risk based maintenance and aging management program. Condition based inspection policies are also used for maintenance of deteriorating systems (Castanier et al. 2005). In nuclear industries, many aging management programs such as in-service inspection and surveillance, equipment qualification and reliability centered maintenance have been implemented (Pachener 2002).

Traditionally, reliability characteristics of an item are demonstrated by life testing. Failure time data are collected from life tests and then the lifetime distribution is inferred using survival analysis techniques (Lawless 2003). Once the lifetime distribution is obtained in-service maintenance is scheduled. However, lifetime distribution model is not suitable for condition based maintenance optimization, since it only quantifies the component is failed or not. An intensive aging management program deals with the in-service inspection strategy, degradation level of the component and decision about the maintenance action to be carried out. An challenging feature of the ageing management is - the decision is required to be made under uncertainty and the most important uncertainties are: the uncertainty in the instantaneous degradation level and degradation rate, which describes the present state and remaining life of the component, respectively. For a highly reliable system, the large scale inspection and collection of degradation data during an in-service inspection is difficult and capital intensive. The small sample data, used in probabilistic modeling and assessment is therefore confounded with considerably statistical uncertainties. Also in many cases, approximate deterministic approaches considering upper/lower bounds of the probability distribution are prescribed for the safety assessment (CSA-N285.8 2005). These models do not quantify the safety of the system in probabilistic terms. Therefore, better statistical models are essential for the safety assessment of high risk systems like nuclear power generating systems.

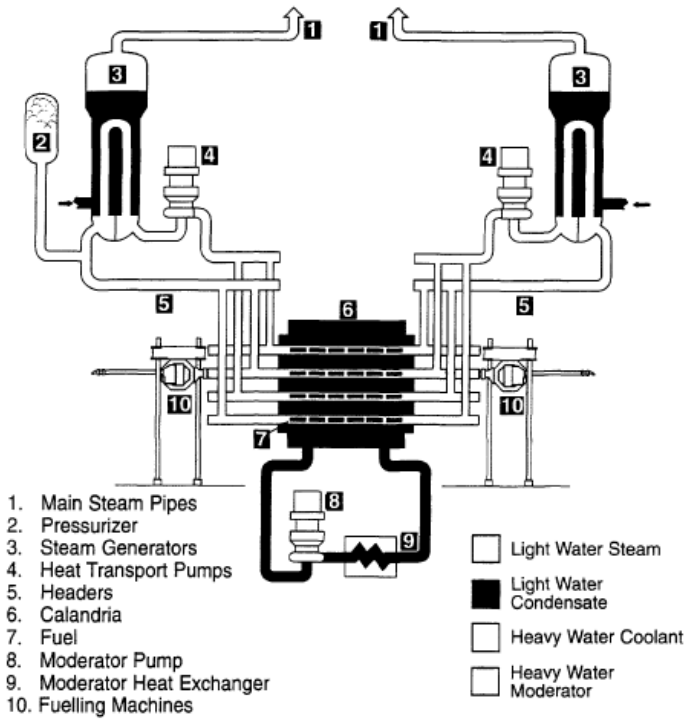

Figure 1.2: Schematic illustration of a CANDU reactor core, its primary heat transport system and it's fueling machines

1.2 The CANDU Reactor

A NPP is a complex technical system consisting of a vast number and variety of engineered subsystems, structures and components (SSCs) that experience uncertain aging and degradation. A schematic flow diagram for a typical CANDU[1] heat transport system (HTS) and moderator system is shown in figure 1.2. An important feature of the CANDU reactor is the use of heavy water both as moderator and as the heat transporter, which allows a critical chain reaction to be sustained

[1]CANadian Deuterium Uranium, is a registered trademark of Atomic Energy of Canada Limited

with natural uranium fuel. A typical CANDU reactor assembly (IAEA 1998) comprised of the low-pressure cylindrical vessel (calandria), two end shields, end shield supports, and the reactor assemblies as shown in figure 1.3. The vertical ends of calandria are joined by a few hundred horizontal calandria tubes (CT). Fuel channel assemblies are essential part of the HTS in a CANDU reactor. The primary purpose of fuel channel is to locate and support the fuel bundles in the reactor core. Each fuel channel (Fig. 1.4) consists of four major components: the pressure tube (PT), the CT, the annulus spacers and the end fitting. Since the fuel bundles reside inside the PTs, heat generation in a CANDU reactor takes place in a few hundred high temperature, high pressure PTs. The ends of each PT is rolled into stainless steel end fittings to form a pressure tight, high strength joint. These end fittings also provide a flow path for primary coolant between the PT and rest of the primary HTS through the feeder pipe attached to each end fitting.

CANDU PTs are exposed to temperature up to 310^0C, internal pressure of about 10 MPa and total fluence of approximately $3{\times}10^{26}$ n/m^2 in 30 years of design life (Puls 1997). The severe operating conditions cause changes in dimensions and material properties resulting sag, elongation, diametral expansion of the tube (IAEA 1998). The PTs are also subjected to corrosion by slightly alkaline heavy water coolant that flows inside them. Due to the aforementioned factors, the PTs are considered to be the most critical component from the aging management point of view. An overview of different degradation mechanisms for CANDU PT leading to break-before-leak or rupture is as illustrated in figure 1.5.

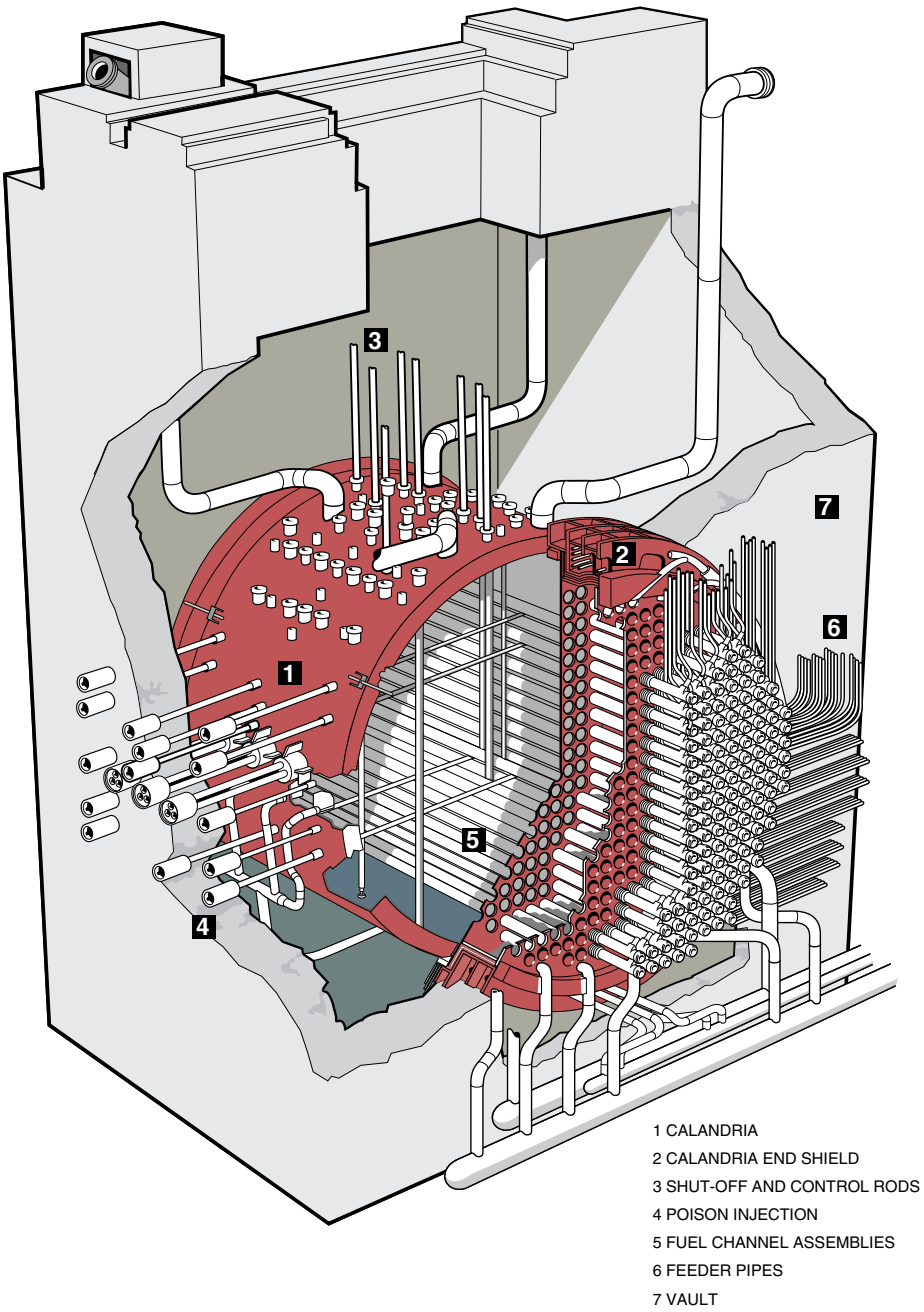

Figure 1.3: CANDU 6 reactor assembly

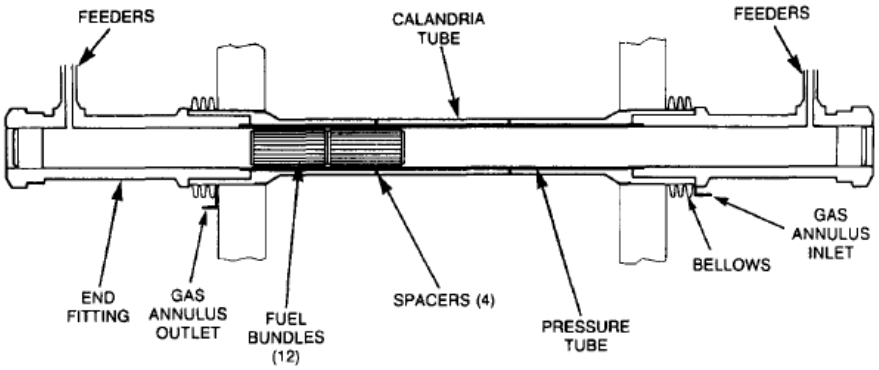

Figure 1.4: Schematic illustration of a CANDU fuel channel

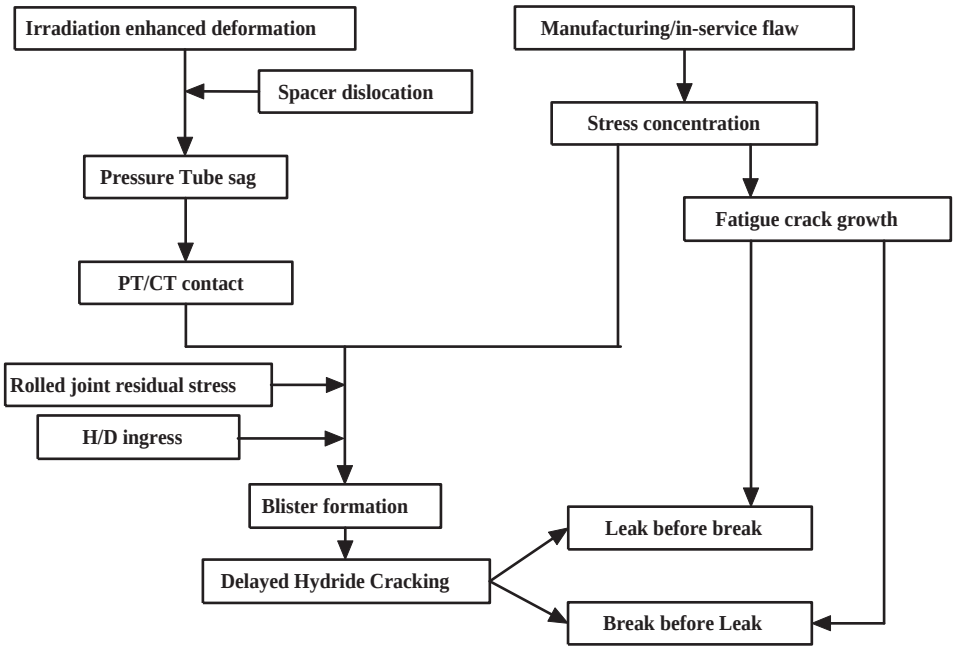

Figure 1.5: CANDU pressure tube failure mechanism

1.3 Research Motivation

The demand for energy is growing day by day and at the same time sources of energy are depleting. Nuclear energy has proved to be a reliable source of energy and helped to solve partially the problem of increasing energy demand. Early CANDU reactors were designed with limited knowledge about ageing related degradations. Although overall performance of PTs in CANDU reactors has been good, some of PTs in early reactors leaked and ruptured due to unanticipated ageing mechanisms (IAEA 1998). Due to the problems concerning manufacturing defects or flaws, imperfect rolled joints, loose spacer design and high hydrogen ingress rate of Zircaloy tubes; many PTs had gone under tube replacement programs. Though each time, design changes e.g. use of Zirconium alloy tube in place of Zircaloy tube, tight spacer design etc. evolved, making the reactors more and more reliable, but the modeling of ageing degradation mechanism taking uncertainties into account still a challenging issue for a scientific life cycle management program. Presently periodic inspection and maintenance programs are carried out in accordance with Canadian standards. The main driving force behind these techniques is to improve safety and reduce unnecessary inspection and maintenance, and hence leading to a more efficient use of resources. Since many nuclear power plants reaching the end of their design life, the life cycle management and ageing related issues should be focused intensively. The structure of probabilistic life cycle management proposal is illustrated in figure 1.6. In data analysis phase the in-service inspection data is analyzed to get valuable information about the population and system condition. The data analysis includes nonparametric analysis for the uncertainties involve with small sample data, parametric statistical model fitting and model testing. The residual life estimation and condition assessment includes probabilistic modeling of

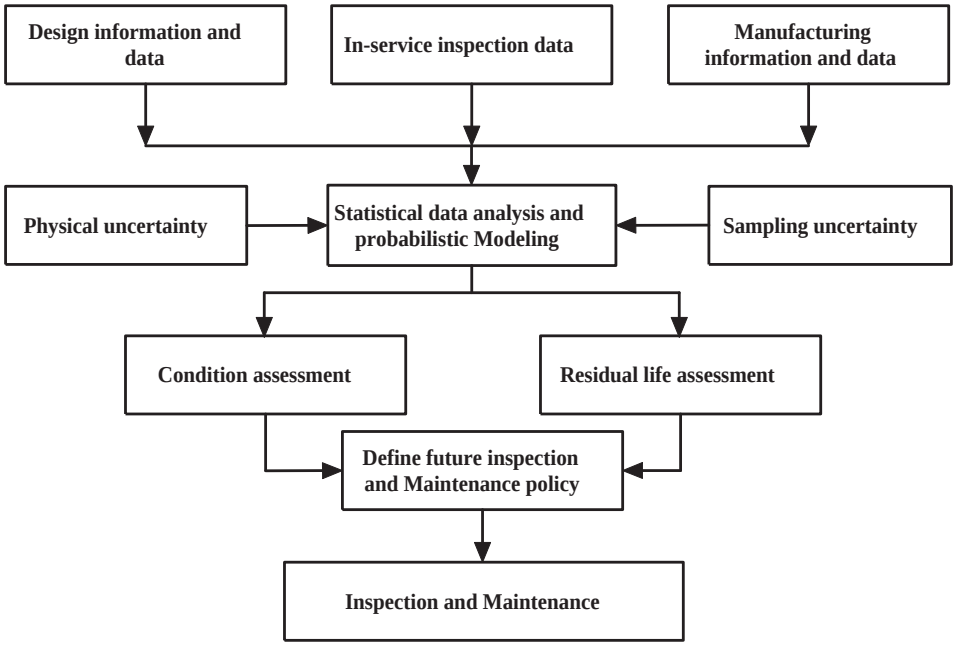

Figure 1.6: Probabilistic life cycle management model

various ageing mechanisms. The result allows decision makers to assess the system performance and implement future inspection and maintenance strategies. Different maintenance actions can be prescribed according to the condition level. For degradation within the acceptance level, controlled operational profile can then be prescribed, where as for degradation above acceptance level, repair and replacement decision can be made.

A few tubes in early CANDU units had a significant tensile stress concentration due to sharp manufacturing defect. In-service wear of PTs in CANDU reactors can be caused by fuel bundle scratching during refueling, bearing pad fretting caused by fuel pencil vibration and fuel bundle bearing pad positions and debris fretting. Such manufacturing and/or operational flaws can cause significant stress concentration, which creates potential cause for delayed hydride cracking (DHC) and rupture

or break-before-leak situation. Due to aforementioned factors flaw assessment is considered as an important part of a reactor core assessment program (IAEA 1998).

In general, the deterioration data (e.g. flaw dimension data) from field inspections during previous outages exhibits considerable variability. The variability in the data provides the scope for the use probabilistic assessment models. However, flaw assessment models proposed in CSA standard (CSA-N285.8 2005) are either deterministic or semi-probabilistic that considers upper/lower bound values for the distributed quantities.

Each CANDU reactor consists of 380 to 480 fuel channels, and it is not possible to inspect all the PTs, which are placed inside the fuel channels. Due to the small sample size, the determination of a representative distribution type becomes difficult, resulting in modeling error. Another consequence of the small sample size is that it hinders an accurate estimation of the distribution parameters. Inference about the population parameters from the finite small samples therefore suffers from above mentioned uncertainties. On the other hand in-service inspection is cost intensive, which does not motivates one to go for large scale inspection. In the case of NPPs periodic in-service inspection and testing of safety systems and their components is performed at periodic intervals. Inspections are carried out on sampling basis. Therefore, decision on quantitative risk based inspection sample size requirement is another important aspects which requires attention.

Apart from the sampling uncertainty, modeling error also plays a vital role in a failure assessment models. In the flaw assessment model, flaw induced stress field or the stress intensity factor serves as the mechanical model. Traditionally, the applied mechanics framework known as linear elastic fracture mechanics (LEFM) and it's extension to plastic zone stress field analysis serves the basis for determination of behavior of cracked bodies. LEFM solution provides reasonable results about the

stress field only up to a limited distance excluding the crack-tip. It leads to singular stress and strain fields at the crack tip. This motivates further research on flaw induced stress field.

1.4 Research Objectives

The main objective of the thesis is to develop models for assessment of flaws in pressure tubes of CANDU reactors. The thesis includes the study of probabilistic assessment and flaw induced stress field models. In particular, the thesis deals with following topics:

- To develop probabilistic flaw assessment models due to limitations of deterministic modeling, when inspection data exhibit considerable variability.
- To develop efficient probabilistic assessment models, avoiding the complexities associated with a simulation based assessment models.
- To develop an risk-informed approach for flaw sample size requirement during an in-service inspection, such that the probabilistic analysis will provide results within an specified amount of prediction error.
- To develop an analytical crack-tip stress field model for linear elastic material under generalized uniaxial and biaxial tensile loading considering the effect of crack-tip blunting.
- To develop analytical crack induced stress field model and plastic zone analysis for elastic-perfectly-plastic material considering the effect of crack-tip blunting.

- To develop analytical model for prediction of threshold stress intensity factor, K_{IH} for delayed hydride cracking initiation from a flaw.

1.5 Thesis Organization

The thesis is organized into nine chapters including this first introductory chapter. Chapter 2 provides a brief literature review on the fundamental concepts of reliability theory, pressure tube degradation mechanism and conventional crack induced stress field modeling. Chapter 3 describes the deterministic bounding flaw procedure for flaw assessment (DHC initiation and leak-before-break) as prescribed by CSA standard (CSA-N285.8 2005) followed by proposed probabilistic model. The limitations of deterministic flaw assessment procedure is also discussed in this chapter. Chapter 4 presents concepts of partial factor based code calibration, followed by a semi-probabilistic approach, for flaw assessment based on the partial factors. Chapter 5 deals with the issue of inspection sample size requirement and associated uncertainty error. A risk based approach is presented to define the required flaw sample size during a scheduled inspection. The proposed approach is illustrated considering the criterion of DHC initiation in the presence of planar flaw type defects. In chapter 6 conventional crack induced stress field model for an linear elastic material is described. The limitations of LEFM solution is discussed and proposed stress field model is presented. In Chapter 7 the proposed stress field model for linear elastic material is used along with the Von Mises yield criterion to model stress field in the plasticity zone of an elastic-perfectly-plastic material. In Chapter 8 the the concept of stress field formulation for elastic-perfectly-plastic material is applied to develop an analytical time dependent threshold stress intensity factor model for delayed hydride cracking initiation. Chapter 9 concludes the research

findings of this thesis. Highlights on the scope of future research topics related to this research is also presented in chapter 9. Finally references are listed at the end of the thesis.

Chapter 2

Literature Review

2.1 Reliability Theory

It is true that all plant, equipment, and components have a finite life, and eventually the very best components will fail. Therefore, without a technical definition of reliability, to which numerical values can be allocated, it would not be possible for engineers to make meaningful decisions and it would not be possible for detailed analysis of component failures in a way towards reliability improvement. Hence, it is vitally important to understand the meaning of reliability. By definition, reliability, is the ability of a component/system to perform its specified function under stated working environment for a specified period of time. Opposite to reliability is failure, referring to the event of failing to perform the required function or failing to conform to performance standards under stated working environment for the specified period of time.

Any Reliability assessment model generally incorporates three sub models: 1) data analysis and statistical model fitting, 2) component reliability estimation and

3) system reliability estimation.

In data analysis phase, the in-service inspection data is analyzed and information about the variability in the data is explored. The data analysis includes non-parametric analysis (Daniel 1990, Desu et al. 2004), parametric statistical model fitting and model testing (Kapur et al. 1977, Benjamin et al. 1970). The parameters of any parametric distribution model are estimated by parameter estimation methods (Lawless 2003) e.g. likelihood methods. Some time confidence interval on the estimated parameters are also explored to examine the sampling uncertainty (Benjamin et al.1970). Component reliability estimation considers various failure and ageing mechanisms and estimate the probability for the event. System reliability estimation utilizes component reliability and the knowledge of the way the components are connected in the system (Hoyland et al. 1994).

Two different models most commonly used for reliability estimation are: 1) stress strength interference (SSI) model and 2) lifetime model. The former is traditionally used in structural engineering, whereas the latter is extensively used for biomedical, social sciences and other engineering areas such as electronic device design and automobile industries.

In the SSI model, failure is the event of the strength being less than the applied stress (Freudenthal 1947). To calculate reliability, first we model the strength and stress as random variables or a function of basic random variables. The probabilistic distribution and their parameters are obtained from statistical analysis of data sets from experiments and/or observations. For time variant rare events such as wind load, extreme value theory (Ochi 1989) is usually employed to find probabilistic distributions of their extreme values. In its simplest form, a structural reliability problem considers load effect S and the resistance or capacity to withstand the load as R. The resistance, R, is a function of material properties and geometrical

properties, while S is a function of loads. The material properties, geometrical properties and loads may be random variables, called basic random variables. The system or component continues to perform as long as its resistance exceeds the effect of the loads placed on it, conversely, failure occurs when the resistance is less than the load. The condition $R = S$ is denoted by *limit state function* of the component or system and the event $R < S$, represents failure condition. If the probability distribution of R and S are known, the probability of failure for a limit state can be determined as,

$$\mathrm{P}_f = \mathrm{P}[R \leq S] = \int_0^\infty F_R(x) f_S(x) dx \tag{2.1}$$

where F_R is the cumulative distribution function (CDF) of R, and f_S is the probability density function (PDF) of S. The limit state probability (Eq. 2.1) provides a quantitative measure of the safety of the component or system that takes explicit account of the uncertainty reflected in the probabilistic properties of R and S. Depending on the nature of randomness, the strength and the stress may be modeled by a stochastic process (Yuan et al. 2006). More detail discussion on the methods for reliability analysis based on the SSI approach can be found in (Ang et al. 1975, Thoft et al. 1982, Madsen et al. 1986, Melchers 1999, Rangnathan 1999).

Due to association of common variables in the limit state equations of failure modes in a system/component with multi failure mode mechanism, the failure modes are sometimes correlated (Pandey 1998). This leads to the correlated joint standardized normal distribution function incase basic variables are normally distributed. Direct numerical integration for multi-normal integration is known to be impractical owing to high computational time and accumulation of numerical errors (Pandey 1998). Therefore, several approximation methods have been de-

veloped e.g. Dunnet and Sobel approximation (Johnson et al. 1972) for solution. Hohenbichler and Rackwitz (Hohenbichler 1983) applied first order concepts to develop an efficient method (FOMN) for multi-normal integration. This approach was later refined (G-FOMN) by Tang and Melchers (Tang et al. 1987). Pandey (Pandey 1998) developed an efficient approach (PCM) by approximating a multi-normal integration by a product of one-dimensional integration. Later, Mori and Cato (Mori et al. 2003) used importance-sampling method for evaluation of multi-normal integration. Effective first order, second order bounding formulas are also developed by many researchers (Ditlevsen 1979, Ramachandran 1984, Song et al. 2002).

All physical systems deteriorates over time and also the environment in which the object works, always changes with time. Hence, reliability is also a time-related concept, leading to the development of lifetime models for reliability analysis. In general, the time at which the object fails to perform the specified function is called the failure time, or life time. The lifetime model treats life time directly as a random variable, without explicit modeling of the stress and strength. The probability distribution of life time characterizes the object's reliability over time. Other reliability characteristics can be estimated directly form the lifetime distribution. Consider the time to failure T is a continuous random variable with PDF $f(t)$. Probability of failure can then be defined as the cumulative time to failure distribution function $F(t)$ and survival function can be defined as $S(t)$. The survival function $S(t)$ is a complementary to $F(t)$, which takes a value one at start and zero as the time approaches to infinity. Hazard rate is defined as a measure of the probability that a component will fail in the next time interval, given that the component is survived up to the beginning of that time interval. The relationship among these functions can be found in many standard textbooks of reliability theory for e.g. (Gertsbakh 2000). Analysis with incomplete information such as censored or missed failure

time data is one of the main themes in the research of lifetime data analysis. For more details on these topics refer to (Gertsbakh 1989, Barlow et al. 1981, Meeker et al. 1998, Lawless 2003).

Although both SSI and lifetime models give the probabilistic measure of reliability, they have their own advantages and disadvantages. One of the advantages of the SSI model is that it provides the sensitivity information about basic variables during reliability analysis. This provides feedback to optimize the design and maintenance policy to achieve target reliability. It's drawback is that it usually gives only the reliability at one point of time and fails to provide explicit interpretation of the variation of reliability along time. Therefore no direct information on the lifetime of engineering systems can be inferred using SSI model. The advantage of lifetime model is that we can easily see from the hazard rate function the deterioration of the system performance as the function of time, which enables us to pre-specify the maintenance policies as early as design stage. Its disadvantage is obvious: it gives no information on the failure mechanisms.

2.2 CANDU Reactor Core Assessment

2.2.1 Degradation Mechanisms

A comprehensive description of fuel channel, PTs and related ageing and maintenance issues are discussed in (IAEA 2001, IAEA 1998). Puls et al. (1997) discussed the importance of understanding PT's aging characteristics for a comprehensive aging management program to ensure safe and economical performance of the reactor. They presented a brief overview on life limiting issues of PTs, methodology for assessment of DHC, aging issues related to material properties and hydrogen builds

up. In summary, the primary ageing mechanisms for PTs in a CANDU reactor are due to:

1. Irradiation Enhanced Deformation
2. Changes in PT Material Properties
3. Flaws and Defects
4. Delayed Hydride Cracking

The deformation of a PT is a complex interaction of elastic, plastic, thermal creep and irradiation effects (Christodoulou 1996) and can be categorized into four types (Park et al. 2002, Kwak et al. 2005): 1) elongation of tube, 2) increase in diameter, 3) decrease in wall thickness, and 4) sag of tube.

It is known from past research on PT materials that irradiation increases the hardness and tensile strengths, and reduces ductility and fracture toughness. Hence susceptibility to fracture in Zr-2.5%Nb tube increases slightly and velocity of DHC increases slightly, particularly at the inlet due to its lower temperature value. Consequence of such changes in material properties are susceptibility to fracture, decrease in margin to leak-before-break (LBB) and increase in probability of PT rupture.

Flaws and defects

In general, flaws and defects can be developed during fabrication, installation, commissioning or operation. In-service wear of PTs in CANDU reactors can be caused by fuel bundle scratching during refueling, bearing pad fretting caused by fuel pencil vibration and fuel bundle bearing pad positions and debris fretting.

A few tubes in early CANDU units had a significant tensile stress concentration due to sharp manufacturing defect. They are prone to opening up during service by an oxidation process. Moreover, hydrogen or deuterium (H/D) may concentrate at large tensile stress region forming hydrides. Since, sufficient hydride formation may create favorable condition for DHC initiation, it is important to eliminate any potential cause of PT tensile stress concentration such as flaws and defects. Two tubes at Bruce unit-2, leaked in 1986 due to the presence of manufacturing flaws, which could not be detected during pre-service inspections. A few similar flaws were also discovered later on by improved inspection, and tubes were replaced.

Delayed hydride cracking

DHC is a form of localized hydride embrittlement phenomenon, which in the presence of a tensile stress field manifests itself as a sub-critical crack growth process (IAEA 2004). It is caused by hydrogen migration up to tensile stress gradient to the region of high stress concentration. Once the local solid solubility is exceeded, brittle hydride platelets precipitate normal to the tensile stress. Growth of hydride precipitate continues till a hydride platelet of critical size is formed. A hydride platelet of the critical size cracks under concentrated stress leading to the growth of the crack. This crack growth is delayed by the time required for hydrogen to reach the crack tip and form hydride platelets of critical size and hence called delayed. Hydrides are always present in PTs at room temperature, while in the range of operating temperature hydrides can form only when hydrogen equivalent concentration is greater than terminal solid solubility (TSS). TSS values, varies from 40 to 70 PPM depending on temperature (low at low temperature). Thus, DHC is a temperature dependent phenomenon. If H/D concentration is low, DHC can occur only when reactor is cold; otherwise if the concentration is significant to

allow hydrides to exist at operating temperature, DHC could occur during operation in the existence of sufficient tensile stress. Crack growth process by DHC is characterized by crack growth rate, called DHC velocity (DHCV).

Detailed physics of DHC phenomena is discussed in (Puls 1997, IAEA 2004, Sagat et al. 2000, Singh et al. 2002). In nutshell, the primary causes leading to DHC initiation and growth of a flaw are: (1) initial hydrogen concentration in the PT, (2) deuterium ingress (Bahurmuz et al. 1993), (3) hydried build up (Sawatzky 1985, Singh et al. 2002), and (4) rolled joint residual stress.

2.2.2 Leak-Before-Break Concept

In a CANDU fuel channel assembly, each PT is located inside a CT with the gas filled annulus between these two tubes insulating the high temperature primary coolant inside the PT from the low temperature moderator outside the CT. Four annulus spacers keep each PT separated from the CT, which surrounds it, while also allowing the CT to provide sag support for the PT. The annular space around the fuel channel is filled with dry CO_2 gas that incorporates moisture-detecting instrumentation to warn about any leak from either the PT or the CT in the annulus. The CANDU annulus gas system is qualified to detect small PT leaks, and procedures are in place to ensure the reactor shut down before a crack grows to the critical size. Most instances of cracking, PTs leaked long before the critical crack size was reached and the leak detection system was capable to detect the condition and the reactor was safely shut down. Thus, the PTs in CANDU reactors exhibited a LBB behavior. This capability was demonstrated when a tube ruptured in 1983 while Pickering unit 2 was operating, and again in 1986 when a tube ruptured during a cold pressurization test at Bruce unit 2. Brief review of LBB concept,

related to the fitness for service guidelines are presented by Wong et al. (1990). The guidelines contain criteria for performing both deterministic and probabilistic LBB analysis. Moan et al. (1990) described deterministic procedure for LBB analysis. The method depends on showing that the time available to detect a crack is much greater than the time required to detect the crack. The time available is a function of crack velocities, crack lengths at instability and crack lengths at penetration of the tube wall. Action for the operators is shown to have a usable margin before tube rupture, supporting continued use of LBB as an operating criterion. Walker (1990) developed a probabilistic methodology and the associated computer code (MARATHON) to calculate the time for first leakage to unstable failure in a probabilistic format. Another probabilistic model (BLOOM), was proposed by Puls et al. (1998), which estimates the cumulative probabilities of break-before-leak (BBL) and LBB considering more complex shut down scenarios. This approach is described in relation to an example of a possible shutdown scenario. The result of past extensive research on LBB evaluation shows considerable confidence with LBB phenomena.

2.2.3 Inspection and Assessment Requirements

In the case of NPPs, non-destructive inspection and testing of safety systems and their components is performed at appropriate intervals classifying, inaugural, baseline and periodic inspections. The purpose of periodic inspection is intended to ensure that an unacceptable degradation in component quality is not occurring and the probability of failure remains acceptably low for the life of the component. Inspections are carried out on sampling basis. The samples are chosen from areas subjected to severe operating conditions. Clause 12 of the Canadian standard CSA-N285.4 (1994) defines the requirements for periodic inspection of fuel channel

Table 2.1: Sample size for periodic inspection program

Plant	**Total Samples**	**High power region**	**Low power region**
Single unit	5	4	1
Multi unit			
1st unit	5	4	1
2nd unit	4	3	1
3rd unit	3	2	1
4th unit	2	1	1

pressure tubes of a CANDU reactor. The number of samples required for each inspection shall be as provided in the Table 2.1.

A complete periodic inspection is performed within 3 year period commencing 4 years after the generation of first power. Subsequent periodic inspection is planned for time intervals not exceeding 6 years or $1/5^{th}$ of the design life for single unit plant. For multi unit plant the periodic inspection for the lead unit is same as for single unit system. For subsequent units the inspection interval is not to exceed 10 years or $1/3^{rd}$ of design life.

The inspection procedures are selected based on capability to detect discontinuities and dimensions. Volumetric inspection methods for flaw detection are based on ultrasonic and wave techniques. Dimensional inspections are used for measurement of PT sag deformation, diameter, wall thickness and fuel channel bearing position. PTs are also tested for material properties in scheduled inspections. During inaugural inspection, fracture toughness and DHC velocity are measured. Base line inspections are scheduled for measurement of hydrogen concentration for at least 6 pressure tubes within 2 years period commencing 9 year after generation of first net power. During periodic inspections hydrogen concentration, fracture toughness and DHC velocity is measured. Incase any pressure is removed for inspection with addition to above measurements, visual inspection of surfaces and position of garter

Table 2.2: Allowable failure probabilities

Core Type	j = 0	j = 1	j = 2	j = 3	j = 4	j = 5
I	0.01	0.005	0.0025	0.00167	0.00125	0.001
II	0.033	0.0165	0.00825	0.0055	0.00413	0.0033

Type I core → *Design basis core*
Type II core → *Updated assessment that demonstrates acceptability of an initiating event failure frequency that is equal to the total allowable value of 0.033 events per reactor year*
j → *Number of known in-service pressure tube degradation mechanism*

springs and volumetric inspection are also carried out.

When a detected flaw does not satisfy the acceptance criteria, (Clause 12 CSA-N285.4 1994), CSA-N285.8 (2005) specifies mandatory technical requirements and non-mandatory evaluation procedures for fitness for service assessments. CSA-N285.8 (2005) specified the allowable failure probabilities applicable to a reactor for various numbers of known in-service degradation mechanisms as presented in Table 2.2.

2.3 Crack Induced Stress Field

The uncertainties associated in any probabilistic assessment can be classified into two types: (1) modeling uncertainty, and (2) statistical modeling uncertainties. The mechanical modeling uncertainty is associated with the deterministic model used for the performance function evaluation. In fracture assessment, the applied mechanics framework known as fracture mechanics serves the basis for determination of behavior of cracked bodies and the concept of stress intensity factor is central to the theory of linear elastic fracture mechanics (LEFM). Therefore, a brief literature review on the development of classical fracture mechanics theory for crack induced stress field is discussed below.

2.3.1 Linear Elastic Fracture Mechanics

A material fractures when sufficient stress are applied on the atomic level to break the bonds that holds atom together. The theoretical cohesive strength of a material is approximately E/π and experimental fracture strength for brittle material are typically 3 to 4 orders magnitude below this value (Anderson 1995). Fracture cannot occur unless the stress at the atomic level exceeds the cohesive strength of the material. Thus, for subcritical crack growth initiation from a flaw, the flaw must lower the global strength by magnifying the stress locally. The first quantitative evidence for the stress concentration effect of flaws was provided by Inglis (1913). His analysis for an elliptical hole ($2a$ long $2b$ wide) centrally located in infinite flat plate subjected to applied tensile stress (S) perpendicular to major axis gives the stress at the tip of crack as

$$\frac{\sigma_{yy}^{tip}}{S} = 1 + \frac{2a}{b} \tag{2.2}$$

Eq. 2.2 predicts infinite stress at the tip for limiting case of an sharp crack. Thus, a material that contains a sharp crack theoretically should fail upon the application of infinitesimal load. This paradox of a sharp crack motivated Griffith (1920) to develop energy based fracture theory rather than local stress. Later on Westerguard (1939), Irwin (1957), Sneddon (1946) and williams (1957) individually derived analytical models for crack induced stress field for isotropic linear elastic materials. Defining a polar coordinate axis with origin at crack tip, it is shown that the stress field in any linear elastic field cracked body is (Anderson 1995)

$$\sigma_{ij} = \left(\frac{k}{\sqrt{r}}\right) f_{ij}(\theta) + \sum_{m=0}^{\infty} A_m r^{m/2} g_{ij}^{m}(\theta) \tag{2.3}$$

where σ_{ij} is the stress tensor, r and θ are coordinate system, k is a constant and f_{ij} is a dimension function of θ. Both the proportionality constant k and f_{ij} depends on the mode of loading. As $r \to 0$, the leading term approaches infinity, but the other higher order terms depend on geometry and remain finite or approaches zero. Thus, the stress near a crack tip varies with $1/\sqrt{r}$ regardless of configuration of the cracked body and mode of loading. The constant k is later replaced in terms of K, known as stress intensity factor. For mode-I loading, the stress field ahead of a crack tip considering only the leading term of Eq. 2.3 is then presented as

$$\lim_{r \to 0} \sigma_{ij} = \left(\frac{K_I}{\sqrt{2\pi r}} \right) f_{ij}(\theta) \tag{2.4}$$

where $K_I = S\sqrt{\pi a}$. The stress field for mode-I loading on the crack plane, $\theta = 0$, near the crack tip where singularity dominates is thus given by

$$\sigma_{xx} = \sigma_{yy} = \frac{S\sqrt{a}}{\sqrt{2r}} \quad \text{and} \quad \sigma_{xy} = 0 \tag{2.5}$$

Note that Eq. 2.4-2.5 is only valid near the crack tip, where $1/\sqrt{r}$ singularity dominates the stress field. Stresses far from crack tip are governed by remote boundary conditions. This analysis also gives the transverse displacement for a mode-I crack as (Parker 1981)

$$v = \frac{S(\kappa + 1)}{4\mu} \sqrt{{a_f}^2 - x^2} \tag{2.6}$$

which indicates the crack opens in to an ellipse with semi major axis as a_f and semi minor axis as $S(\kappa+1)/(4\mu)$. where $\mu = E/2(1+\upsilon)$ and

$$\kappa = \begin{cases} \frac{3-\upsilon}{1+\upsilon} & \text{plane stress} \\ 3-4\upsilon & \text{plane strain} \end{cases}$$

2.3.2 Elastic Plastic Fracture Mechanics

Linear elastic stress analysis of sharp crack predicts infinite stress at the tip. In real material, however, stresses at the crack tip are finite because the crack-tip radius must be finite. Plasticity and inelastic material deformation leads to further relaxation of crack-tip stresses. The elastic stress analysis becomes increasingly inaccurate as the plastic region at the crack-tip grows. Since LEFM ceases to be valid when significant plastic deformation precedes failure, several researchers developed analysis to correct for yielding at the crack-tip based on the extension of LEFM. Two most common methods are 1) Irwin's approach (Anderson 1995, Parker 1981), where the LEFM analysis is extended to model the plasticity zone and 2) the strip yield model (Dugdale 1962, Barenblatt 1962) based on the idea of cohesive zone.

Irwin Approach

On the crack plane the LEFM stress field is given by Eq. 2.5. As a first approximation, the elastic-plastic boundary is assumed where the LEFM stress field satisfy a yield criterion. For plane stress condition, yielding occurs when $\sigma_{yy} = \sigma_Y$, the uniaxial yield strength of the material. This leads to the first order estimate of

plastic zone size as

$$r_y = \frac{1}{2\pi}\left(\frac{K_I}{\sigma_Y}\right)^2 \tag{2.7}$$

As the second approximation, neglecting any strain hardening effect, the stress distribution for $r \leq r_y$ is considered as constant and equal to σ_Y. The stress singularity is truncated by yielding at the crack tip. This simple analysis is not strictly correct because it was based on LEFM solution. When yielding occurs, stresses must redistribute in order to satisfy equilibrium. The forces present in the elastic in an elastic material inside the first estimate of the plastic zone can not be carried in the elastic plastic material because stress can not exceed σ_Y. To accommodate these forces, a simple force balance leads to second order estimate of the plastic zone, r_p.

$$r_p = \frac{1}{\pi}\left(\frac{K_I}{\sigma_Y}\right)^2 \tag{2.8}$$

which is twice as large as r_y, the first order estimate. To accommodate the stress distribution, Irwin assumed the tip of the crack in the center of the plastic zone. Thus effective half crack size is defined as, $a_{eff} = a_i + r_y$, where a_i = initial half crack size. Similarly the effective stress intensity factor is given by $K_{eff} = S\sqrt{\pi a_{eff}}$. A schematic representation of the Irwin approach is shown in figure 2.1-2.2.

Strip Yield Model

The strip yield model was proposed by Dugdale (1962) and Barenblatt (1962) independently. They consider a long, slender plastic zone at the crack tip in a non-hardening material in the plane stress in an infinite plate. They assumed a crack of length $2a_i + 2\rho$, where ρ is the plastic zone, with a closure stress equal to σ_Y applied at the crack tip. The model approximates the elastic plastic behavior by superimposing two elastic solutions: 1) a through crack under remote tension and

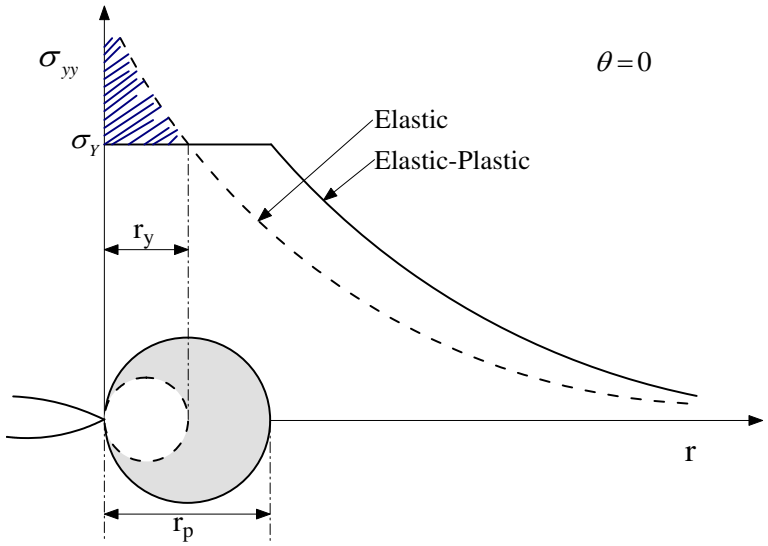

Figure 2.1: First order (r_y) and second order (r_p) estimates of plastic zone. The hatched area represents the load must be redistributed, resulting a larger plastic zone

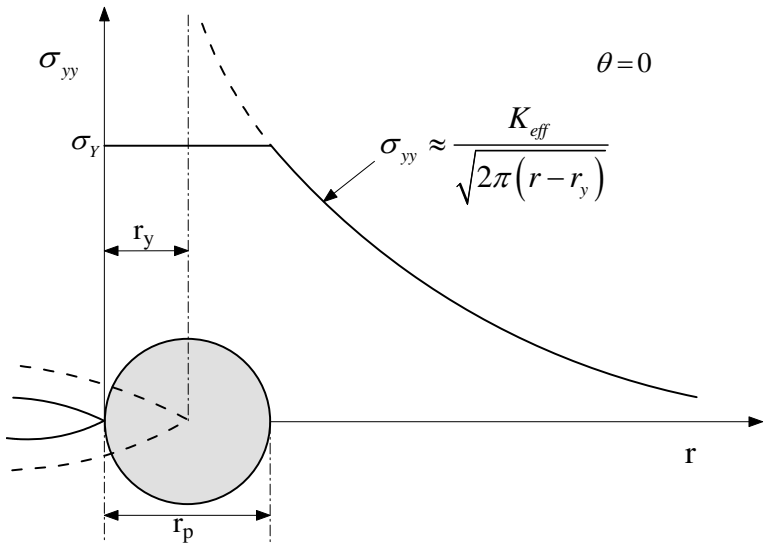

Figure 2.2: Irwin plastic zone correction. The increase in the effective stress intensity is taken into account by assuming the crack is longer by r_y

2) a through crack with closure stresses at the tip. The plastic zone length, ρ, must be chosen such that the stress intensity factors from the remote tension and closure stress cancel each other, truncating the stress singularity at the tip. This leads to

$$\frac{a_i}{a_i + \rho} = \cos\left(\frac{\pi S}{2\sigma_Y}\right) \tag{2.9}$$

For $S \ll \sigma_Y$, neglecting higher order terms except first two terms of the Taylor series expansion of Eq. 2.9 gives similar expression of plastic zone size as Irwin.

$$\rho = \frac{\pi}{8}\left(\frac{K_I}{\sigma_Y}\right)^2 \tag{2.10}$$

The effective stress intensity factor with the strip yield model is calculated by taking $a_{eff} = a_i + \rho$. However, this tends to over estimate K_{eff} (Anderson 1995). Burdekin and Stone (1966) obtained a more realistic estimate of K_{eff}. The plastic zone shape predicted by the yield strip model bears little resemblance to actual plastic zones in metals, but many polymers produce similar process zones and thus this model is better suited for polymers (Anderson 1995).

HRR Model

As long as the stresses increase monotonically, the mechanical response of elastic-plastic material is identical to non-linear elastic material. The deformation theory of plasticity, which relates total strains to stresses is equivalent to non-linear elasticity. By idealizing elastic-plastic deformation as non-linear elastic behavior, Rice (1968) provided the basis for extending fracture mechanics beyond LEFM validity limits. Hutchinson (1968) and Rice and Rosengren (1968) independently shown that the non-linear energy release rate (J) could be written as path independent line integral

and is uniquely characterizes crack tip stresses in non-linear materials. They assumed a power law hardening stress strain relationship known as Ramberg-Osgood equation.

$$\frac{\varepsilon}{\varepsilon_Y} = \frac{\sigma}{\sigma_Y} + \xi \left(\frac{\sigma}{\sigma_Y}\right)^n \tag{2.11}$$

where $\varepsilon_Y = \sigma_Y/E$, ξ is a dimensionless constant and n is the strain hardening exponent. First part of this equation is elastic contribution, while the second part is due to plastic deformation. The governing differential equation for deformation plasticity for plane problem in a Ramberg-Osgood material in terms of stress function Φ is given by

$$\Delta^4\Phi + f(\Phi, \sigma, r, n, \xi) \tag{2.12}$$

For mode-I crack Hutchinson (1968) choose Φ in a series form as

$$\Phi = C_1(\theta)r^s + C_2(\theta)r^t + ... \tag{2.13}$$

In the region close to the crack tip, elastic strains are negligible compared to plastic strains; only the second term in Eq. 2.12 is relevant and the stress function is expressed (assuming $s < t$) as

$$\Phi = \kappa\sigma_Y r^s \widetilde{\Phi}(\theta) \tag{2.14}$$

where κ is amplitude of stress function and $\widetilde{\Phi}$ is a dimensionless function of θ. Actual stress field, known as HRR singularity, are obtained by applying appropriate far field stress boundary conditions and stress free boundary conditions on the crack surface (Anderson, 1995) as

$$\sigma_{ij} = \sigma \left(\frac{E\ J}{\xi\sigma^2 I_n r}\right)^{1/(n+1)} \widetilde{\sigma}_{ij}(n, \theta) \tag{2.15}$$

For a linear material, $n = 1$, and Eq. 2.15 predicts $1/\sqrt{r}$ singularity consistent with LEFM theory. For detailed derivation of the HRR solution the reader can refer (Hutchinson 1968, Rice et al. 1968).

2.4 Concluding Remarks

It is known from literature study that CANDU reactors are complex engineering systems and presence of a flaw in a CANDU PT can endanger the safety of the nuclear plant. DHC mechanism is a known crack growth mechanism which may create vulnerable situation. Therefore, for safety and continued operation of existing NPP's, probabilistic flaw assessment models are required. Further, to reduce the error in statistical modeling of random variables, sufficient inspection data is necessary. On the other hand large scale inspection in cost intensive. Therefore a balanced between inspection sample size and possible prediction error must be maintained. In this context risk-informed inspection sample flaw size requirement is an important research issue need to explored.

Eventually, all the probabilistic flaw assessment models use some kind of mechanical stress field model. Till date these stress field models are based on classical LEFM solution and it's extension to model the plasticity behavior. LEFM model predicts singular results for a sharp crack, which is a paradox. If LEFM results are valid then any material with a sharp crack will fail immediately with the application of a vary small external load. Models based on the extension of LEFM contains the same apparent anomaly as the LEFM singularity; namely both predict infinite stresses at the crack-tip. Therefore, further research in this area is required to develop a better analytical stress field model.

Chapter 3

Probabilistic Formulation for Flaw Assessment

3.1 Introduction

It is clear from the previous chapters that the PT in a CANDU reactor is the most critical component due to severe operating conditions. Presence of a flaw in a PT may be even more hazardous, since it may grow (due to stress concentration effect) by DHC mechanism leading to rupture of the PT. DHC is a sub-critical crack growth mechanism and it is active when hydrogen concentration is sufficiently high and the stress intensity factor at the crack tip is above a threshold value (K_{IH}). The growth of flaw type defects in Zirconium alloy (Zr-2.5%Nb) PT through DHC is a serious form of degradation mechanism compared fatigue crack growth (Wong et al. 1990), which has potential to compromise the integrity of the PT. Fatigue cracks usually propagate slowly, typically 10^{-8} m/cycle, whereas hydride cracking propagate at up to 10^{-6} m/s (Moan et al. 1990). Therefore probability of detecting

a propagating subcritical DHC crack during a periodic inspection is small. Thats why assessment of any flaw type defect is given high priority in a reactor core assessment program. Technical standards have been developed in the past describing assessment procedure for protection against fracture. Canadian standard N285.8 (2005) specifies the general requirements for evaluation of the structural integrity of cold worked Zr-2.5 wt%Nb alloy PTs in operating CANDU reactors. When a flaw is detected in any PT, that does not satisfy the acceptance criteria (CSA-N285.4 1994), the licensee is required to demonstrate compliance with the technical requirements of CSA-N285.8 (2005) to justify continued operation.

A comprehensive probabilistic assessment of PT against fracture protection includes: DHC initiation assessment from a part-through-wall flaw and Leak-before-break assessment. If a part-through-wall flaw (Fig. 3.1) is present in a PT, then it may initiate and grow by DHC in presence of sufficient hydrogen and applied stress. If undetected, the growing DHC flaw at some point in time will penetrate the PT wall to become a through-wall flaw. In the event of through-wall penetration of a flaw, the primary coolant will leak into the annulus space between PT and CT. The increase in the moisture content of the re-circulating gas can be detected through the instrumentation system, which sends a warning signal (beetle alarm) to the operator. Once the leak is confirmed, the reactor is systematically shutdown. The typical variation of the pressure and temperature in a reactor shutdown transient (RSDT) is shown in figure 3.2, where the full power power operating condition is defined by pressure $p = 8.9$ MPa and temperature $t = 293\ ^{o}$C. A timely shutdown is necessary to ensure that the crack propagation is arrested before the unstable fracture (or rupture) of the PT takes place.

In present context, the assessment of flaws against fracture protection is a two step approach:

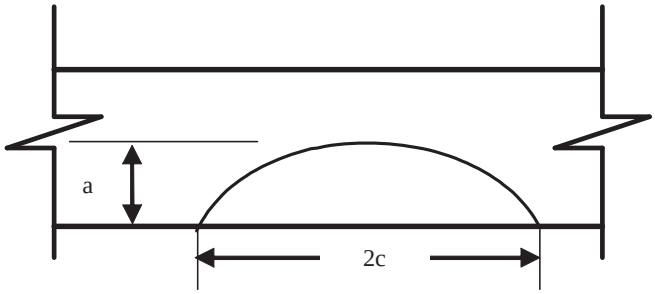

Figure 3.1: Characterization of part-through-wall flaw geometry

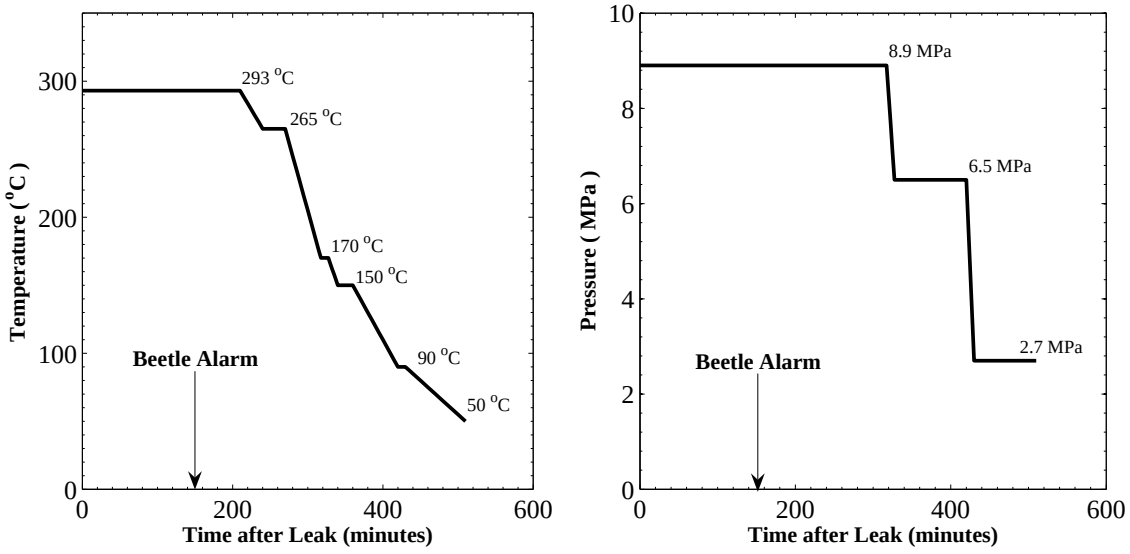

Figure 3.2: A typical reactor shutdown transient

1. **DHC initiation assessment:** In the event of a presence of a part-through-wall flaw, the tube is assessed for the likelihood of flaw initiation by DHC.

2. **LBB assessment:** In the event of DHC initiation and growth from a part-through-wall flaw, followed by PT penetration and leaking, the tube is assessed for the likelihood of PT rupture before the station specific safe shutdown of the reactor (RSDT).

CSA Standard N285.8 (2005) has specified deterministic and probabilistic methods for both planar and volumetric flaw assessment. In deterministic bounding PT analysis, CSA-N285.8 (2005) recommends the use of upper/lower bounds of the random variables. Although the deterministic bounding PT approch is simple, the associated degree of conservatism is not quantified and it does not provide any risk significance of the assessment. Recognizing that there is significant uncertainty associated with some of the variables and that the deterministic method does not provide a risk-informed basis for fitness for service, a more detailed probabilistic approach has been recommended by the CSA Standard. A full probabilistic method based on simulations actually require excessive amount of information and computation time, which makes impractical for routine assessment work. Moreover, in some cases the available performance model for flaw assessment is either implicit or complex (e.g. LBB assessment model), which leaves no option but to use simulation approach. Computer simulation programs have been developed in the past for probabilistic LBB analysis such as Marathon (Walker 1990) and Bloom (Puls et al. 1998). Simulations tend to be fairly involved due to large repetitive calculations associated with the estimation of a small probability.

In this chapter, explicit performance functions are formulated for flaw assessment. This enables the use of efficient first order reliability method (FORM)

method for probability computation. The developed explicit performance functions along with complete probabilistic information of the random variables are used and the efficient FORM method is employed for probability computation. The demerits of the deterministic approach are discussed and the proposed model results are presented. The deterministic parameters used in the following analysis are PT inner radius (r_i) = 52.73 mm and PT wall thickness (w) = 3.8 mm.

3.2 Deterministic DHC Initiation Assessment

3.2.1 Method

The goal of the deterministic DHC initiation assessment approach is to demonstrate that in the event of the presence of a part-through-wall flaw and sufficient hydride concentration, DHC initiation from the flaw is avoided. In the present analysis, a planar fretting flaw is considered. Similar analysis can also be done for volumetric flaws. The necessary steps required for the deterministic DHC initiation assessment for planar flaws based on bounding flaw dimensions are described in CSA-N285.8 (2005), and are summarized below. The deterministic condition of DHC initiation from a planar flaw is

$$K_I^{UB} > K_{IH}^{LB} \tag{3.1}$$

where, K_I is the applied stress intensity factor for an axial part-through-wall planar flaw and K_{IH} is the threshold stress intensity factor for DHC initiation also known as DHC initiation toughness. The stress intensity factor (K_I) for an axial part-through-wall planar flaw located away from the rolled joint is given in Clause

A.5.2.2.2 of CSA standard N285.8 (2005) as

$$K_I = \left[p\left(\frac{r_i}{w} + 1\right) F_P\right] \sqrt{\frac{\pi\ a}{Q}} \tag{3.2}$$

where p = pressure in MPa, r_i = internal PT radius, w = PT wall thickness, Q = flaw shape parameter given by $Q = 1 + 1.464(a/c)^{1.65}$, a = flaw depth, c = half flaw length, F_P = geometry correction factor under pressure loading. Depending on the range of a/c and a/w, different equations are given in Clause A.5.2.2.4 of CSA standard N285.8 (2005) for computing F_P. To compute an upper bound K_I, upper bound flaw depth a_{UB} and upper bound half flaw length c_{UB} at 97.5% percentile is used. The lower bound value of K_{IH} is given in CSA-N285.8 (Clause D.6.2) as

$$K_{IH}^{LB} = 4.5 \text{ MPa}\sqrt{m} \tag{3.3}$$

The method is illustrated through an example in the next section.

3.2.2 Illustration

The empirical distributions of planar flaw dimensions (a and $2c$) in a sample of debris fretting flaws are shown in figure 3.3. The flaw dimensions can be fitted reasonably well with lognormal distribution (Fig. 3.4-3.5) with probability density function

$$f(x) = \frac{1}{\sigma\sqrt{2\pi}x} \exp\left[-\frac{(\ln x - \mu)^2}{2\sigma^2}\right] \tag{3.4}$$

Note that the parameter μ and σ are not the mean and standard deviation of variable X. The logarithm of variable X is normally distributed with mean μ and

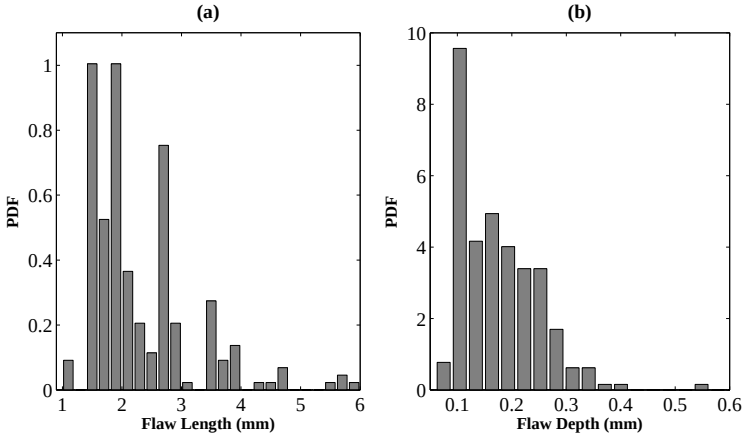

Figure 3.3: Distribution of (a) flaw length and (b) flaw depth

Table 3.1: Distributional property of variables

Variable	Distribution	Mean	Standard deviation	COV
a	Lognormal	μ_a=0.1743 mm	$\sigma_a = 0.0761$ mm	$\delta_a = 0.4364$
c	Lognormal	μ_c=1.1669 mm	$\sigma_c = 0.4067$ mm	$\delta_c = 0.3485$

standard deviation σ. The mean and standard deviation are given as

$$\mu_x = E[x] = \exp(\mu + \sigma^2/2) \tag{3.5}$$

$$\sigma_x^2 = Var[x] = \exp(2\mu + \sigma^2)[\exp(\sigma^2) - 1] \tag{3.6}$$

The estimated distribution parameters are given in Table 3.1. The 97.5% upper bound values computed from the fitted distributions are $a_{UB} = 0.3621$ mm and $c_{UB} = 1.6968$ mm. Using these 97.5% percentile upper bound values, we compute, $a_{UB}/c_{UB} = 0.2134$ and $a_{UB}/w = 0.0953$. The expression for geometry factor for this range of $[0 \leq a/c \leq 1]$ and $a/w \cong 0$ is given (CSA-N285.8 2005) as

$$F_P = \frac{2wr_o}{r_o^2 - r_i^2}\left(1.13 - 0.07\sqrt{a/c}\right) \tag{3.7}$$

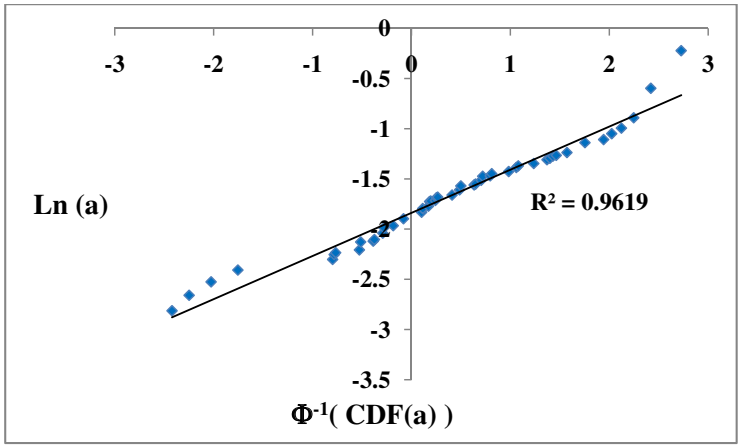

Figure 3.4: Lognormal probability paper plot of flaw depth (a)

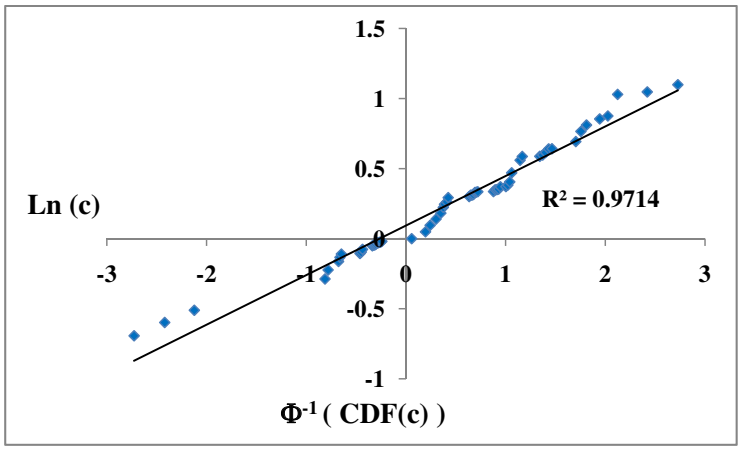

Figure 3.5: Lognormal probability paper plot of half flaw length (c)

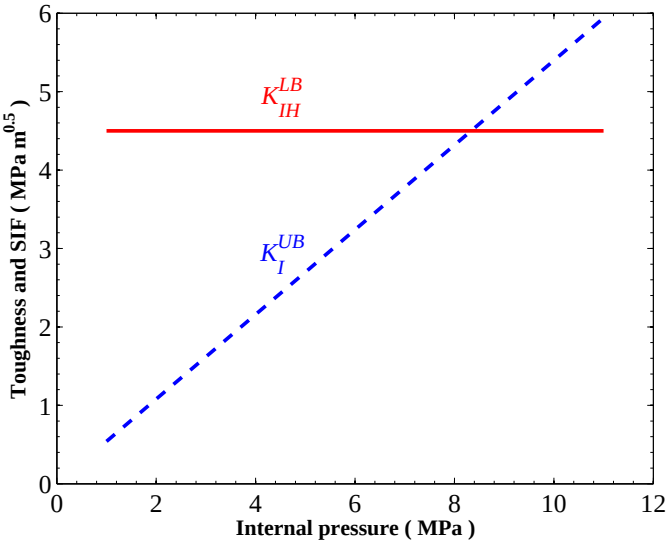

Figure 3.6: Results of deterministic DHC initiation assessment

where r_o is PT outer radius. By substituting appropriate parameters in Eq. 3.7, we compute $F_P = 1.1358$. Further substituting the values of F_P in Eq. 3.2 gives the upper bound K_I as

$$K_I^{UB} = 0.5398 \times p \tag{3.8}$$

Note that the upper bound K_I is a deterministic function of operating pressure p. The lower bound K_{IH} given by Eq. 3.3 is also an deterministic constant. Therefore the DHC initiation condition given by Eq. 3.1 is a function of two deterministic quantities. The results of such a deterministic DHC initiation analysis for a flaw far away from rolled joint where σ_h^r is absent is shown in figure 3.6.

At full power operating condition ($p = 8.9$ MPa), the upper bound K_I (4.8042 MPa$\sqrt{\text{m}}$) is slightly greater than the lower bound K_{IH} (4.5 MPa$\sqrt{\text{m}}$). Hence, the deterministic DHC initiation criterion is not satisfied at full power operating condition.

3.3 Deterministic Leak-Before-Break Assessment

3.3.1 Method

The goal of the deterministic LBB approach is to demonstrate that in the event of the DHC initiation and growth of a part-through-wall flaw followed by through-wall crack penetration in a PT, the operator has sufficient time, followed by the leak detection, to shut down and depressurized the rector in a controlled manner. Steps and necessary equations for the deterministic LBB analysis are described in section C.4.2 of CSA Standard N285.8 (2005), and are summarized below.

First the time axis is discretized as $x_1, x_2, \cdots, x_n$ and suitable pressure (p_i) and temperature (t_i ^{o}C) are assigned to each interval from the RSDT shown in figure 3.2. The deterministic condition for LBB, i.e. a growing crack does not become unstable during the RSDT, is specified in CSA-N285.8 (2005) as

$$2c_{UB}(x_i) \leq 2CCL_{LB}(x_i) \quad (\text{for all}\, i = 1, n) \tag{3.9}$$

where $2c_{UB}$ and $2CCL_{LB}$ denote upper and lower bounds of length of growing through-wall crack and the critical crack length, respectively. A typical LBB analysis consists of a sequence of events in which size of the crack ($2c$) is calculated step by step and compared with the critical crack length ($2CCL$) during the RSDT cycle. This step by step calculation is required to account for changes in the pressure and temperature in RSDT, because a sub critical flaw under hot pressurized conditions could become critical at a reduced temperature due to reduction in the fracture toughness.

The length of a growing crack at time x_i can be given as (CSA-N285.8, Cl.

4.2.2.7)

$$2c_i = 2c_{i-1} + A_c \left(\frac{V_{i-1} + V_i}{2} \right) (x_i - x_{i-1}) \tag{3.10}$$

where A_c is a correction factor and it is equal to 2 for flaws away from the rolled joint region. Note that $2c_0$ is the initial through-wall flaw penetration length and a typical value of $2c_0 = 20$ mm is recommended by CSA-N285.8 (Clause C.4.2.2.2).

The DHC growth velocity as a function of temperature is given as (Clause D.10.3)

$$V(t) = exp \left(A_a + \frac{B_a}{273 + t} + \epsilon_a \right) \tag{3.11}$$

Coefficients in this equation are obtained by regression analysis of experimental data: $A_a = -3.7722$, $B_a = -5943.2$, $\epsilon_a = 0.1442 \times U$ is the random regression error and U is a standard normal variate. Note that $t-$variate with a large degree of freedom (>20) given in CSA-N285.8 (2005) can be replaced by a normal variate without any loss of accuracy.

To compute an upper bound crack length, the 97.5% percentile of the DHC velocity is recommended as

$$V_U(x_i) = \exp \left(A_a + \frac{B_a}{273 + t(x_i)} + 0.2837 \right) \tag{3.12}$$

Note that $t(x_i)$ is the temperature at time x_i during RSDT.

The critical crack length at time x_i is a function of the fracture toughness (K_c), flow stress (σ_f) and hoop stress (σ_h), which in turn depend on the pressure and temperature. The following equations time dependent relationships are given to compute the half critical crack length (CSA-N285.8, Cl. D.13.3)

$$CCL(x_i) = \frac{K_c^2(x_i)\,\pi}{8\sigma_f(x_i)^2 \ln\left[\sec\left(\frac{\pi M \sigma_h(x_i)}{2\sigma_f(x_i)}\right)\right]} \tag{3.13}$$

The hoop stress depends on the pressure $p(x_i)$

$$\sigma_h(x_i) = p(x_i)\left(1 + \frac{r_i}{w}\right)$$

the flow stress is a function of temperature

$$\sigma_f(x_i) = 1004.5 - 1.1995\ t(x_i)$$

and the bulging factor, M, is given as

$$M = \sqrt{1 + 1.255\left(\frac{CCL(x_i)^2}{w\,r_m}\right) - 0.0135\left(\frac{CCL(x_i)^2}{w\,r_m}\right)^2} \tag{3.14}$$

Note that the calculation of CCL requires a time consuming iterative method, since M is an implicit function of CCL.

To compute the lower bound critical crack length, the lower bound fracture toughness (K_L MPa$\sqrt{\text{m}}$) is recommended as

$$K_L(x_i) = \begin{cases} 72 & \text{if } t(x_i) > 150^o\text{C}, \\ 27 + 0.30\ t(x_i) & \text{if } t(x_i) \leq 150^o\text{C}. \end{cases} \tag{3.15}$$

Using these equations, the bounds $2CCL_{LB}(x_i)$ and $2c_{UB}(x_i)$ are computed for all stages of RSDT, and Eq. 3.9 is used to assess the LBB condition. The method is illustrated through an example in the next section.

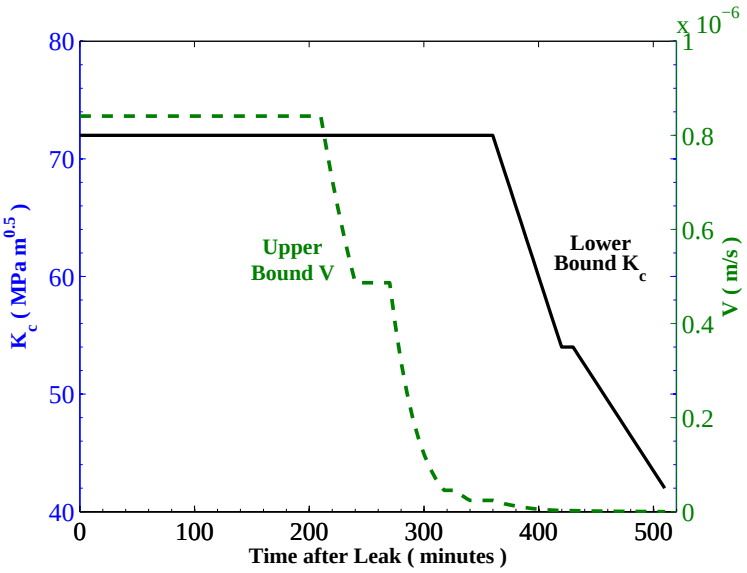

Figure 3.7: Variation of lower bound K_c and upper bound V during the RSDT

3.3.2 Illustration

An application of the deterministic LBB method to RSDT (Fig. 3.2) is presented in this section. The bounds of K_c and V are functions of temperature and their variation during the RSDT is shown in figure 3.7.

In figure 3.8, the bounds $2CCL_{LB}(x_i)$ and $2c_{UB}(x_i)$ are computed for all stages of RSDT. It was assumed that beetle alarm warns 150 minutes after the leak starts, which triggers the shutdown sequence.

Figure 3.8 shows that the DHC crack grows steadily from 20 mm to 46 mm in the first 320 minutes due to sustained high temperature ($> 150\ ^oC$) in phase I. After this, the crack growth is retarded due to a significant decrease in the temperature.

In contrast, the critical crack length fluctuates significantly during the RSDT due to the combined effects of K_c (temperature), σ_h (pressure) and σ_f (tempera-

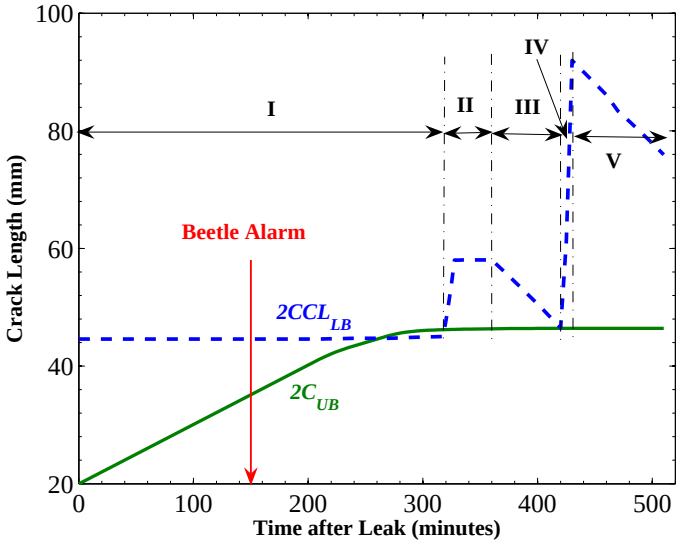

Figure 3.8: Results of deterministic LBB analysis

ture). The reason for this fluctuation is that CCL decreases as the temperature drops due to reduction in K_c and it increases with pressure drop due to reduction in hoop stress (a driving force for cracking).

The critical crack length remains constant ($\cong$ 45 mm) up to 320 minutes due to a constant pressure (8.9 MPa) and temperature being over 150 ^{o}C (Phase I). The $2CCL$ then increases to 58 mm due to the reduction in pressure to 6.5 MPa (Phase II). A further drop in temperature to 90 ^{o}C at 420 minute reduces K_c, which reduces $2CCL$ to 46 mm (Phase III). After 420 minutes, the pressure is significantly reduced to 2.7 MPa, which results in a steep rise in $2CCL$ to 90 mm (Phase IV). As the temperature continues to decrease, $2CCL$ also gradually decreases until the end of the RSDT.

Thus, there are two critical times at 320 and 420 minutes, when the actual and critical crack lengths are fairly close to each other. After 420 minutes, the critical

length remains much higher than the actual length, so that the LBB criterion is not likely to be violated. In this particular case the deterministic requirement is not satisfied for the given RSDT.

3.4 Remarks

Although the deterministic assessment is attractive due to its simplicity and limited information requirement, it's interpretation in the context of modern risk-informed regulatory framework is ambiguous. The deterministic assessment has basically binary outcomes,'*acceptable*' (Safe) or '*not acceptable*' (Fail), with no reference to associated conservatism or safety level.

In reality, the associated variables (a, c, K_c, V) are distributed quantities or random variables. The deterministic assessment criterion compares the bounds that are computed using heuristically assigned bounds to the basic random variables. Therefore, this comparison does not provide any risk insight. In simple terms, even if the deterministic condition is satisfied, what is implied reliability level? This question can not be answered.

For example, in DHC initiation analysis the estimates of K_I is function of random variables a and c and thus necessarily a distributed quantity. The deterministic assessment criterion compares the lower bound K_{IH} with upper bound K_I which is computed using heuristically assigned percentiles to a and c. Therefore, the comparison does not provide any risk insight. In other words if the deterministic condition is satisfied i.e. $K_{IH} > K_I$, what is the reliability level? This question can not be answered at present. Similarly, in LBB analysis the associated variables K_c and V are distributed quantities or random variables. Because of this, the $2CCL$ and $2c$ at any time during the RSDT also become the distributed quantities. The

deterministic assessment criterion compares the bounds on $2c$ and $2CCL$ that are computed using heuristically assigned bounds to K_c and V. Therefore, this comparison does not provide any risk insight. In other words, even if it is shown that $2CCL > 2c$, what is implied reliability level (probability of LBB)? This question can not be answered at present, without a complete probabilistic analysis.

3.5 Probabilistic DHC Initiation Analysis

A probabilistic DHC initiation approach is necessary to incorporate variability associated with the parameters: DHC initiation toughness K_{IH} and planar flaw dimensions (a, c). This section summarizes distributions of key random variables and an approach to compute the probability of DHC initiation from a part-through-wall planar flaw. This assessment is based on an assumption that there is at least one bounding PT with a planar flaw and sufficient hydrogen concentration required to create a favorable condition for DHC initiation. In principle, the probability of DHC initiation event (C_{in}) can be estimated as

$$\mathrm{P}[C_{in}] = \mathrm{P}[C_{in}|H] \times \mathrm{P}[H] \tag{3.16}$$

where H denotes the event of hydrogen concentration is sufficient high to allow DHC initiation. $\mathrm{P}[C_{in}|H]$ is the conditional probability of DHC initiation given the occurrence of H, and it can be written as

$$\mathrm{P}[C_{in}|H] = \mathrm{P}[K_{IH} - K_I \leq 0] \tag{3.17}$$

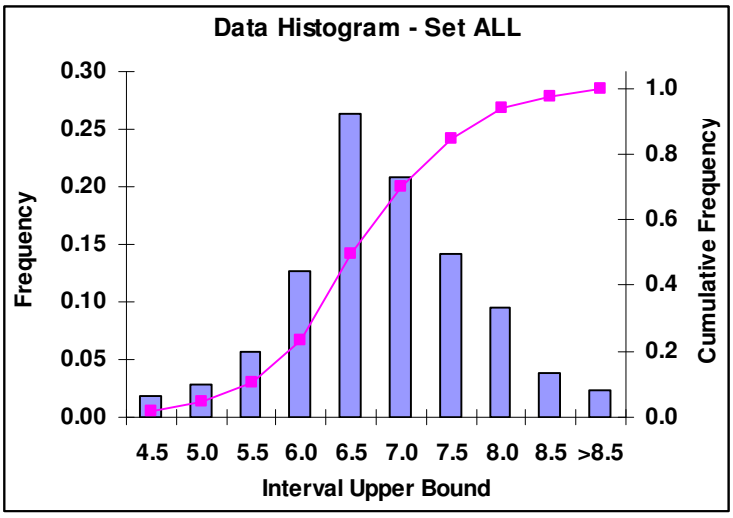

Figure 3.9: Frequency histogram of K_{IH}

3.5.1 Probability Distributions

DHC initiation toughness

The frequency histogram of DHC initiation toughness K_{IH} is as shown in figure 3.9. The DHC initiation toughness (K_{IH} MPa $\sqrt{m}$) is formulated in the form of a normal distributed variable with mean $\mu_{K_{IH}}$ and standard deviation $\sigma_{K_{IH}}$. The parameters of the model are; the mean $\mu_{K_{IH}} = 6.62$ MPa$\sqrt{m}$ and the standard deviation is $\sigma_{K_{IH}} = 0.911$ MPa$\sqrt{m}$.

Applied stress intensity factor

The applied stress intensity factor (K_I) for an axial part-through-wall planar flaw away from rolled joint is given by Eq. 3.2, where geometric factor F_P depends on the range of a/c and a/w. The distribution of a/c and a/w is plotted based on the sample fretting flaw data as shown in figure 3.10.

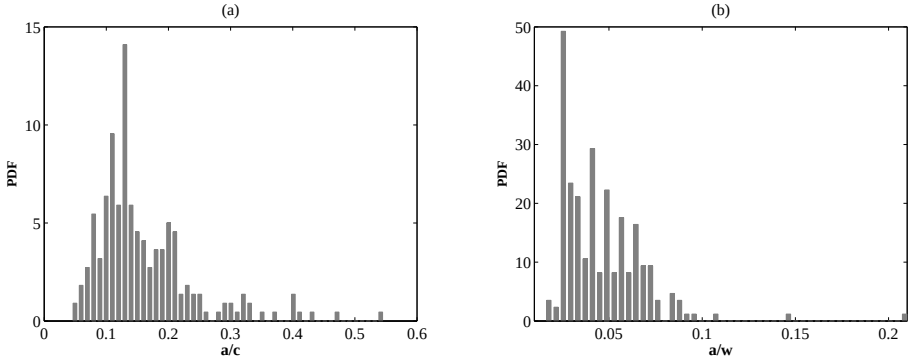

Figure 3.10: Distribution of (a) $\frac{a}{c}$ and (b) $\frac{a}{w}$

The expression for geometry factor for this range of data ($0.0444 \leq a/c \leq 0.5467$ and $0.015 \leq a/w \leq 0.21$) is given by Eq.3.7. Substituting F_P from Eq. 3.7 into Eq. 3.2 gives the following expression for applied stress intensity factor

$$K_I(a,c) = p\ \frac{2\ w\ r_o}{r_o^2 - r_i^2}\left(\frac{r_i}{w} + 1\right)\ f(a,c) \tag{3.18}$$

where $f(a,c)$ is a function of random variable a and c and is given by

$$f(a,c) = \left(1.13 - 0.07\sqrt{\frac{a}{c}}\right)\sqrt{\frac{\pi\ a}{1 + 1.464(a/c)^{1.65}}} \tag{3.19}$$

In order to apply an analytical method of probability computation, the function $f(a,c)$ is fitted with a linear functional relationship as

$$f(a,c) = 0.0135 + 0.0828 \times a - 0.0013 \times c \tag{3.20}$$

Figure 3.11 shows that the linear Eq. 3.20 is a highly accurate approximation of the analytical relation Eq. 3.19. In Eq. 3.20, the distribution of random variables a and c are formulated in the form of a lognormal distribution model. The distribution

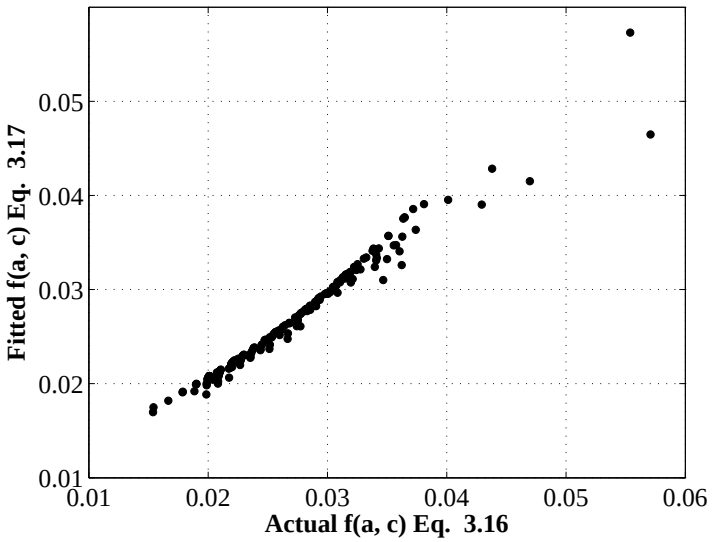

Figure 3.11: Linear Regression Fitting to function $f(a, c)$

parameters are given in Table 3.1.

3.5.2 Reliability Analysis and Results

To compute the probability of DHC initiation, a limit state function is introduced as

$$G(K_{IH}, a, c) = K_{IH} - K_I(a, c) \tag{3.21}$$

such that $G(K_{IH}, a, c) \leq 1$ defines the event of DHC initiation. Using Eq. 3.20 and Eq. 3.21, the stress intensity factor can be written as

$$K_I(a, c) = d_1 \ (0.0135 + 0.0828 \ a - 0.0013 \ c) \tag{3.22}$$

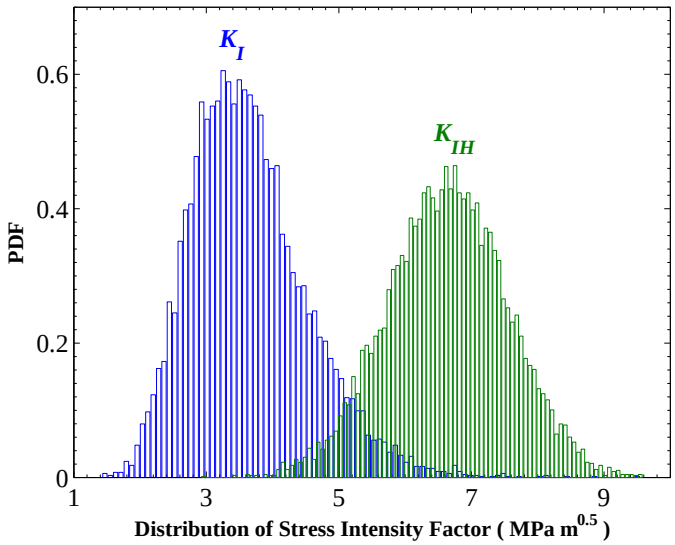

Figure 3.12: Distributions of K_{IH} and K_I (p=8.9 MPa)

where d_1 is a deterministic constant given as

$$d_1 = p\,\frac{2\,w\,r_o}{r_o^2 - r_i^2}\left(\frac{r_i}{w} + 1\right) \tag{3.23}$$

For illustration, distribution of K_{IH} and K_I at full power operating condition were simulated and their PDFs are shown in figure 3.12. An overlap between the two distributions imply that there is a finite probability of DHC initiation.

The probability of DHC initiation was computed using the FORM method (Nowak et al. 2000, Madsen et al. 1986, Melchers 1999). At full power operating condition (p = 8.9 MPa) the probability of DHC initiation is estimated as 1.494×10^{-2} and other details including the design points and sensitivity coefficients are given in Table 3.2.

It is interesting that deterministic analysis uses lower bound K_{IH} value = 4.5

Table 3.2: Results of P$[C_{in}|H]$ analysis

Probability P$[C_{in}|H]$	1.494 $\times 10^{-2}$
Design point, a^*	0.354 mm
Design point, c^*	1.075 mm
Design point, k^*_{IH}	5.677 MPa$\sqrt{}$m
a^* percentile	97.18%
c^* percentile	47.06%
${k_{IH}}^*$ percentile	15.02%
Sensitivity coefficient, α_a	0.8783
Sensitivity coefficient, α_c	-0.0340
Sensitivity coefficient, $\alpha_{K_{IH}}$	-0.4769

MPa$\sqrt{}$m, which is quite low as compared to the computed design point k^*_{IH}. Also, the deterministic approach prescribes the use of 97.5% upper bound half crack length (c), whereas the FORM analysis shows the design point c^* corresponds to 47.06% of the distribution i.e. nearly equal to the median value.

3.6 Probabilistic Formulation of LBB Analysis

A probabilistic LBB approach is necessary to incorporate variability associated with two key parameters: fracture toughness and DHC crack growth velocity (CSA-N285.8 2005). This section summarizes distributions of key random variables and an approach to compute the probability of PT rupture (or BBL) during the shutdown transient. This assessment is based on an assumption that there is at least one bounding PT with a flaw where the stress and hydride concentration are sufficiently high to allow the crack growth by DHC mechanism, and ultimately leading to a through wall crack of a postulated length. In principle, the probability of BBL

event can be estimated as

$$\mathrm{P}[BBL|C_{in}] = \mathrm{P}[BBL|C_{in}] \times \mathrm{P}[C_{in}] \tag{3.24}$$

where the event C_{in} is the DHC initiation from a part-through-wall flaw. $\mathrm{P}[BBL|C_{in}]$ is the conditional probability of BBL or rupture of PT and it can be written as

$$\mathrm{P}[BBL|C_{in}] = \mathrm{P}[2CCl - 2c \leq 0] \tag{3.25}$$

3.6.1 Probability Distributions

DHC Velocity

The DHC velocity (V m/s), described as a function of temperature (t ^{o}C) in Eq. 3.11, can be recast in the form of a logarithmic regression model

$$\ln[V(t)] = \ln[m_V(t)] + \sigma_{lnV}(t)\ U \tag{3.26}$$

This equation implies that $V(t)$ is lognormally distributed with median m_V and logarithmic standard deviation σ_{lnV}. The median is a temperature dependent quantity given as

$$m_V(t) = \exp\left[-3.7722 - \frac{5943.2}{273 + t}\right] \tag{3.27}$$

and $\sigma_{lnV} = 0.1442$ is temperature independent. This model was developed based on regression analysis of crack growth velocity data collected from the testing of PTs removed from various reactors.

At the full power operating condition ($t = 293\ ^o$C), the DHC velocity is denoted as V, which has parameters $m_V = 6.3315 \times 10^{-7}$ m/s and $\sigma_{lnV} = 0.1442$. A

compact expression is developed to describe randomness of DHC velocity at other temperatures, which will be useful in reliability index computation.

The DHC velocity is treated as a random variable to model the variability in the reactor core. It means that for a postulated flaw in a randomly selected PT, the velocity is a realization, v_1, of the random variable V from its parent lognormal distribution. As the temperature changes over the shutdown cycle, $v_1(t)$ also varies along a fixed path. This can be explained further as follows. Suppose at the outset of RSDT ($t_1 = 293\ ^o$C), the DHC velocity for a PT is given as

$$\ln[v(t_1)] = \ln[m_V(t_1)] + \sigma_{lnV}(t_1)\ u \tag{3.28}$$

where u is a realization of U for the specific PT. As the temperature decreases to t_2, the DHC velocity becomes

$$\ln[v(t_2)] = \ln[m_V(t_2)] + \sigma_{lnV}(t_2)\ u \tag{3.29}$$

Because the percentile of the velocity is not changing by a temperature change, u remains unchanged as well. It leads to the following relation

$$u = \frac{\ln\left[\frac{v(t_2)}{m_V(t_2)}\right]}{\sigma_{lnV}(t_2)} = \frac{\ln\left[\frac{v(t_1)}{m_V(t_1)}\right]}{\sigma_{lnV}(t_1)} \tag{3.30}$$

Substituting for $t_1 = 293$, $m_V = 6.3315 \times 10^{-7}$ and $\sigma_{lnV}(t_1) = \sigma_{lnV}(t_2) = 0.1442$, the velocity for any other temperature during the RSDT can be obtained in general as

$$V(t) = V\ \exp\left[10.5 - \frac{5943.2}{273 + t}\right] \tag{3.31}$$

where V is DHC velocity at full power operating condition.

Crack Length

The crack growth in a small time interval $\triangle x_i = x_i - x_{i-1}$ is a product of the time interval with the DHC velocity corresponding to the temperature in this interval. The crack length, $2c(x_n)$ at time x_n after leak is given as

$$2c(x_n) = c_0 + 2\sum_{i=1}^{n} V[t(\overline{x_i})]\triangle x_i \tag{3.32}$$

where c_0 is initial crack penetration length and $\overline{x_i} = (x_{i-1} + x_i)/2$. Substituting from Eq. 3.31 for $V(t)$, we obtain the crack length as

$$2c(x_n) = c_0 + 2\ V\ d(x_n) \tag{3.33}$$

where $d(x_n)$ is a deterministic function of x_n encompassing the effect of temperature as follows:

$$d(x_n) = \sum_{i=1}^{n} \exp\left[10.5 - \frac{5943.2}{273 + t(\overline{x_i})}\right] \triangle x_i \tag{3.34}$$

It is clear that crack length is only dependent on the temperature variation during the shutdown, and it is not affected by the pressure variation.

Fracture Toughness

Fracture toughness is also modeled as a lognormal random variable similar to Eq. 3.26 as

$$\ln[K(t)] = \ln[m_K(t)] + \sigma_{lnK}(t)\ U \tag{3.35}$$

The median m_K and logarithmic standard deviation σ_{lnK} specific to this perticular reactor are given by

$$m_K(t) = \begin{cases} \exp\left[3.762 + 5.8849 \times 10^{-3}\ t\right] & \text{if} \quad t \leq 150\ ^o\text{C}, \\ \exp[4.6495] & \text{if} \quad t > 150\ ^o\text{C} \end{cases} \tag{3.36}$$

$$\sigma_{lnK}(t) = \begin{cases} 0.174\sqrt{1.03226 + \frac{(t-87.742)^2}{103653.9}} & \text{if} \quad t \leq 150\ ^o\text{C}, \\ 0.18346 & \text{if} \quad t > 150\ ^o\text{C} \end{cases} \tag{3.37}$$

For $t > 150\ ^o$C, the fracture toughness, denoted as K, is a temperature independent lognormal variable with median $m_K = 104.5327$ MPa $\sqrt{\text{m}}$ and $\sigma_{lnK} = 0.1834$. As discussed in the previous section and shown by Eq. 3.30, the fracture toughness at any other temperature can also be written as

$$K(t) = m_K(t) \left[\frac{K}{104.5327}\right]^{a(t)} \qquad t \leq 150^0 C \tag{3.38}$$

where $a(t) = \sigma_{lnK}(t)/\sigma_{lnK}$.

Critical Crack Length

The critical crack length, denoted as $2CCL(x_i)$, at time x_i is a function of $K(t)$ and pressure $p(x_i)$. Although Eq. 3.13 is applicable for computing the critical crack length, it is a highly nonlinear equation that requires iterative solution. This is particularly time consuming in probabilistic analysis where repeated evaluations of this function are required. To minimize the computation time, Eq. 3.13 is approximated

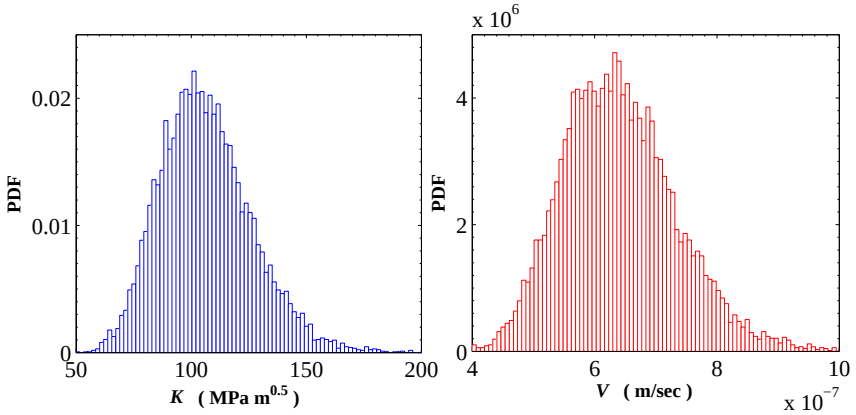

Figure 3.13: Probability distribution of fracture toughness and DHC velocity at full power

by a highly accurate power function as

$$2CCL(x_i) = 2[a_1(x_i) + a_2(x_i)\, K(t, x_i)]^{m(x_i)} \tag{3.39}$$

where coefficients $a_1(x_i)$, $a_2(x_i)$ and $m(x_i)$ are evaluated for each set of temperature $t(x_i)$ and pressure, $p(x_i)$ during the RSDT. In the first 320 minutes after leak, pressure is constant ($p = 8.9$ MPa) and temperature $t \geq 150$ ^{o}C, which makes the critical length a time independent quantity (R_0) given as

$$2CCL_0 = 2[-66.88 + 3.65\, K]^{0.588} \quad (mm) \tag{3.40}$$

3.6.2 Reliability Analysis and Results

The probability density functions (PDFs) of fracture toughness and DHC velocity at full power condition are shown in figure 3.13.

To compute the probability of rupture (BBL), a limit state function is defined

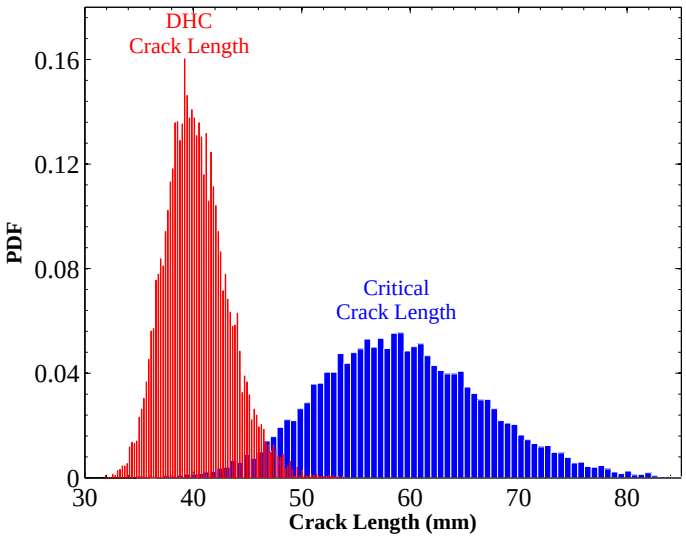

Figure 3.14: Distributions of actual and critical crack lengths

as

$$G(CCL, c, x_i) = 2CCL(x_i) - 2c(x_i) \tag{3.41}$$

Note that $P[G(CCL, c, x_i) \leq 0]$ signifies the cumulative probability of rupture in the time interval $(0 - x_i]$. Distribution of actual and critical crack lengths at $x_i =$ 420 minutes were simulated and their PDFs are shown in figure 3.14. The mean and COV of critical length is 59.2 mm and 0.131, respectively. The actual crack length has mean and COV of 40.3 mm and 0.073, respectively. An overlap between the two distributions imply that there is a finite probability that the DHC crack length could exceed the critical length that could lead to PT rupture.

In figure 3.15, lower (2.5%) and upper (97.5%) percentiles and mean values of $2CCL(x)$ and $2c(x)$ are plotted as a function of time during the RSDT. As discussed before, after 420 minutes the bounds of critical and actual crack lengths are so far apart that the probability of BBL in the RSDT beyond this point is almost zero.

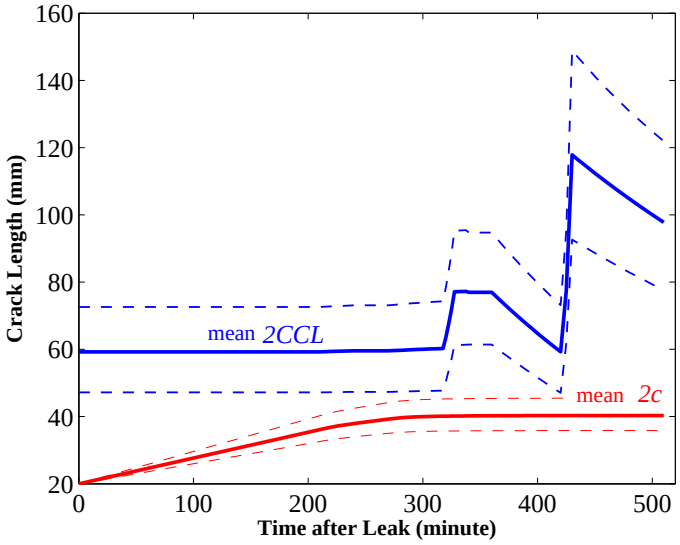

Figure 3.15: Mean and 95% bounds for actual and critical crack length during the RSDT cycle

The critical length at the full power condition has the smallest mean value, and later in RSDT it increases as the pressure is deceased. The increases in $2CCL(x_i)$ are followed by decreasing trend, but it does not fall below the baseline value at full power condition. Thus, the critical crack length can be conservatively taken as a constant $2CCL_0$ given in Eq. 3.40 in the entire RSDT. This simplifies the limit state equation for computing the probability of failure as

$$G(CCL, c, x_i) = 2[-66.88 + 3.65\,K]^{0.588} - c_0 - 120,000\ V\ d(x_n) \qquad (3.42)$$

The unit of V is m/s and x_i is in minutes. For the RSDT shown in figure 3.2, $d(x_n)$=264.064, calculated by taking x_i in minutes and temperature t in ^{o}C. The initial penetration length is $c_0 = 20$ mm. The conditional probability of BBL was computed using the FORM method involving an iterative algorithm for finding the

Table 3.3: Results of P$[BBL|C_{in}]$ analysis

Probability P$[BBL\|C_{in}]$	7×10^{-3}
Design point, K^*	70.263 MPa$\sqrt{}$m
Design point, V^*	7.486×10^{-7} m/s
k^* percentile	1.5%
v^* percentile	88.3%

design points.

The probability of rupture in the RSDT is estimated as 7×10^{-3} and other details are given in Table 3.3. The design point coordinates, $k^* = 70.26$ MPa$\sqrt{}$m and $v^* = 7.486 \times 10^{-7}$ m/s, are 1.5% and 88% percentiles of their respective distributions. It is interesting that deterministic analysis uses 97.5% percentile of V, which is quite high as compared to that associated with the design point v^*.

In summary, in the event of presence of sufficient hydrogen concentration (H), the probability of DHC initiation at full power operating condition is P$[C_{in}|H]$ = 1.494×10^{-2}. In the event of DHC initiation (C_{in}) from a part-through-wall flaw, the probability of BBL for the typical RSDT (Fig. 3.2) is P$[BBL|C_{in}] = 7 \times 10^{-3}$. Hence, the approximate conservative probability of PT rupture or BBL is P$[BBL|H]$ = P$[BBL|C_{in}] \times$ P$[C_{in}|H] = 1.046 \times 10^{-4}$. In the present context, this probability can be accepted as conservative upper bounds. The reason is that the conditional probability ($P[C_{in}|H]$) ignores the probability of presence of sufficient hydrogen concentration. Thus, P$[BBL] < 1.046 \times 10^{-4}$, if $P[H] < 1$.

3.7 Conclusions

This chapter formulates explicit limit state equations for probabilistic flaw assessment of CANDU PTs. The probabilistic formulation covers DHC initiation assess-

ment and LBB assessment.

Although the deterministic method is simple, the associated degree of conservatism is not quantified and it does not provide a risk informed basis for the fitness for service assessment. On the other hand, probabilistic methods based on simulations require excessive amount of information and computation time, making them impractical for routine assessment work. The proposed formulation of explicit limit state equation is helpful in employing First Order reliability method for probability computation, which is highly efficient over the Monte Carlo Simulation method. The approximate conservative probability of PT rupture or BBL for the presented random variables is computed using the proposed formulation and efficient FORM method and is estimated as $\mathrm{P}[BBL] = \mathrm{P}[BBL|C_{in}] \times \mathrm{P}[C_{in}|H] = 1.046 \times 10^{-4}$. This probability can be accepted as conservative upper bounds. The reason is that the conditional probability ($P[C_{in}|H]$) ignores the probability of presence of sufficient hydrogen concentration.

In addition to probability information, design point values of the variables is obtained using FORM method. The CSA standard specifies upper and lower bounds of the variables for deterministic bounding assessment. In the proposed probabilistic DHC initiation assessment, the design point coordinate are found to be $a^* =$ 0.354 mm, $c^* = 1.075$ mm, $k^*_{IH} = 5.677$ MPa$\sqrt{\text{m}}$ which are 97.18 %, 47.06% and 15.02 % of their distributions respectively. It is interesting that deterministic analysis uses lower bound K_{IH} value = 4.5 MPa$\sqrt{\text{m}}$, which is quite low as compared to the computed design point k^*_{IH}. Also, the deterministic approach prescribes the use of 97.5% upper bound half crack length c value, whereas the FORM analysis shows the design point c^* corresponds to 47.06% of the distribution i.e. almost equal to the median value. Similarly, in LBB assessment the design point coordinate, v^* $= 7.486 \times 10^{-7}$ m/s, is 88% percentiles of the distribution. It is interesting that

deterministic analysis uses 97.5% percentile of V, which is quite high as compared to that associated with the design point v^*.

Chapter 4

Reliability Based Flaw Assessment Models

4.1 Introduction

CSA Standard N285.8 (2005) has specified deterministic and probabilistic methods for flaw assessment. As discussed in chapter 3, though the deterministic assessment is attractive due to its simplicity and limited information requirement, its interpretation in the context of modern risk-informed regulatory framework is ambiguous. The deterministic assessment has basically binary outcomes,'*acceptable*' (Safe) or '*not acceptable*' (Fail), with no reference to associated conservatism or safety level.

In reality, the associated variables are distributed or random quantities. But the deterministic assessment criterion considers the heuristically assigned bounds to random variables. For example in DHC initiation analysis the variables a, c and K_{IH} are distributed quantities. Because of this, estimates of K_I is necessarily a distributed quantity. However, the deterministic assessment approach compares

the lower bound K_{IH} with upper bound K_I which is computed using heuristically assigned bounds to a and c. Similarly, in LBB analysis the variables K_c and V are distributed quantities. Because of this, estimates of the $2CCL$ and $2c$ at any time during the RSDT are necessarily distributed quantities. But, the deterministic assessment criterion compares the bounds on $2c$ and $2CCL$ that are computed using heuristically assigned bounds to K_c and V. Therefore, these comparisons do not provide any risk insight. In simple terms, even if it is shown that $K_{IH}^{LB} > K_I^{UB}$ or $2CCL_{LB} > 2c_{UB}$, the implied reliability level is unknown, because the current deterministic criterion is not formally calibrated to a specific reliability level.

This chapter presents an innovative, semi-probabilistic method that bridges the gap between a simple deterministic analysis and complex simulations. In the proposed method, a deterministic criterion of CSA standard N285.8 is calibrated to specified target probabilities based on the concept of partial factors. In other words, the proposed method is a probabilistic version of the deterministic flaw assessment by incorporating partial factors that are calibrated for an allowable probability level. The approach is similar to the load and resistance factor design (LRFD) used for civil engineering structures (Nowak et al. 2000, Madsen et al. 1986). This paper also highlights the conservatism associated with the current CSA standard. The main advantage of the proposed approach is that it retains the simplicity of deterministic method, yet it provides a practical, risk-informed basis for flaw assessment.

In the proposed method, semi-probabilistic assessment equations, corresponding to target reliability are formulated by using the corresponding calibrated partial factors. Satisfying the semi-probabilistic criterion ensures that the actual probability is less than the target probability for which the particular assessment equation is defined. This method is simple to use in practice and it avoid complexities

associated with full probabilistic analysis.

4.2 Concept of Reliability-Based Calibration

4.2.1 Approach

As an alternative to a fully probabilistic approach for quantifying reliability, a deterministic equation can be developed for the design or assessment of structural components. In this equation, all random variables are replaced by their specific percentile values that are determined as a set for a specified reliability level. This can be explained further by considering a simple stress (S) strength (R) reliability problem, in which the failure condition is defined by a limit state function:

$$G(R, S) = R - S \tag{4.1}$$

The failure event is $G(R, S) \leq 0$. Consider a standard case in which R and S are independent, normally distributed random variables with means μ_R and μ_S, standard deviations σ_R and σ_S, and coefficient of variations (COVs), δ_R and δ_S, respectively. The probability of failure can be computed as (Nowak et al. 2000, Madsen et al. 1986):

$$P_f = P[G(R, S) \leq 0] = P[(R - S) \leq 0] = \Phi(-\beta) \tag{4.2}$$

where $\Phi(x)$ is the standard normal cumulative distribution function and β is the reliability index given as

$$\beta = \frac{\mu_R - \mu_S}{\sqrt{\sigma_R^2 + \sigma_S^2}} \tag{4.3}$$

The basic idea behind the reliability-based design is to replace random variables in the limit state function by their factored nominal values. Suppose nominal values of strength and stress variables are r_N and s_N, which could be averages or particular fractiles of these random variables. The limit state is then converted to a design equation as

$$g(R, S) = \gamma_R \, r_N - \gamma_S \, s_N = 0 \tag{4.4}$$

where γ_R and γ_S are partial factors associated with R and S, respectively. The partial factors are pre-calibrated such that a structure satisfying Eq. 4.4 would achieve a target reliability index of β_T. Here, $\gamma_R r_N$ $\gamma_S s_N$ can be referred to as probabilistic bounds of R and S random variables.

Eq. 4.4 provides a basis for design, i.e., the calculation of r_N for a specified s_N, or vice versa. This approach is referred to as load and resistance factor design (LRFD) in structural engineering (Madsen et al.1986). It is more preferable over a full probabilistic analysis, since it retains the simplicity of the deterministic design and at the same time satisfies a quantitative safety target. The LRFD format also provides probabilistic consistency across designs involving different structural materials and configurations. This approach has been applied to nuclear piping (Gupta et al. 2003), containment structures (Han et al. 1998), concrete columns (Mirza 1996), ship structures (Ayyub et al. 1995), bridge structures (Nowak 1995, Nowak et al. 2005), and welded offshore structures (Jiao et al. 1992).

4.2.2 Illustration

This section illustrates the process of calibrating partial factors through an example of designing the piping for pressure using the following limit state equation (Gupta et al. 2003)

$$G(R,S) = R - S(0.5\theta - 0.4) = 0 \quad \text{for} \quad \theta = (d_0/w) \geq 6 \tag{4.5}$$

Here the yield strength of pipe material, R, and the internal pressure, S, are normally distributed random variables. The pipe's outer diameter, d_0, and wall thickness, w, are deterministic constants. Thus, $h = 0.5\theta - 0.4$ is a design constant. Given all the distribution parameters, the reliability index for a pipe with design constant, h, can be calculated as

$$\beta = \frac{\mu_R - \mu_S\ h}{\sqrt{\sigma_R^2 + \sigma_S^2 h^2}} \tag{4.6}$$

It can be rewritten in terms of non-dimensional variables as

$$\beta = \frac{(\lambda - h)}{\sqrt{\lambda^2\ \delta_R^2 + \delta_S^2\ h^2}} \tag{4.7}$$

where $\lambda = (\mu_R/\mu_S)$ is known as the central safety factor. A point on the limit state function that is the nearest to the origin is referred to as the design point, and its coordinates represent the most likely combination of R and S that would cause the failure. For a specified target reliability index, β_T, the design point coordinates, (r^*, s^*) are given as

$$\begin{aligned} r^* &= \mu_R + \sigma_R\ \alpha_R\ \beta_T \\ s^* &= \mu_S + \sigma_S\ \alpha_S\ \beta_T \end{aligned} \tag{4.8}$$

where α_R and α_S are directions cosines of the design points given as

$$\alpha_R = \frac{-\sigma_R}{\sqrt{\sigma_R^2 + \sigma_S^2 h^2}} \quad \text{and} \quad \alpha_S = \frac{\sigma_S\ h}{\sqrt{\sigma_R^2 + \sigma_S^2 h^2}} \tag{4.9}$$

If a component is designed such that all variables are set equal to their design point coordinates, its reliability index would then be β_T.

Partial factors are scaling factors that scale the nominal values of random variables to the design point coordinates. For simplicity of illustration, the nominal values of (R, S) are taken as their mean values, i.e., $r_N = \mu_R$ and $s_N = \mu_S$. The partial factors are then derived as

$$\begin{aligned} \gamma_R &= \frac{r^*}{r_N} = \frac{r^*}{\mu_R} = 1 - \frac{\delta_R^2 \ \beta_T}{\sqrt{\delta_R^2 + (\delta_S h/\lambda)^2}} \\ \gamma_S &= \frac{s^*}{s_N} = \frac{s^*}{\mu_S} = 1 + \frac{\delta_S^2 \ h \ \beta_T}{\sqrt{(\lambda \delta_R)^2 + (\delta_S h)^2}} \end{aligned} \tag{4.10}$$

A partial factor is a function of COVs, δ_R and δ_S, and the central safety factor λ. For given COVs and a target reliability index, first Eq. 4.7 needs to be solved for λ, and then substituting the value of λ in Eq. 4.10 allows the computation of partial factors.

The pipe design equation using the partial factors is written as

$$g(r, s) = \gamma_R \, \mu_R - \gamma_S \, \mu_S \ h = 0 \tag{4.11}$$

For given mean values of stress and strength variables, the pipe design parameters $h = 0.5(d_0/w) - 0.4$ can be calculated using the partial factors calibrated with respect to a target reliability index. The design equation will ensure a uniform reliability level for all pipe designs.

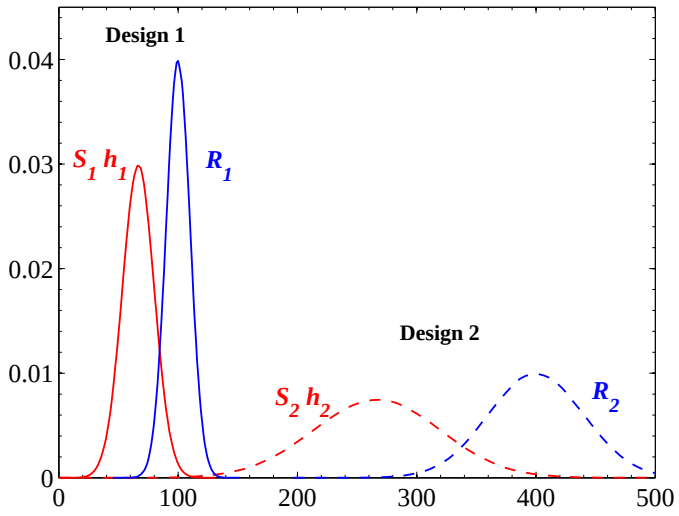

Figure 4.1: Two different design situations for $\beta_T = 2$

4.2.3 Results

In reality, different designs can be obtained for a specified reliability level of the pipe. For example, consider a set of COVs specified as $\delta_R = 0.1$ and $\delta_S = 0.2$ and the target reliability index as $\beta_T = 2$. Suppose for a design situation, the mean design pressure and mean yield strength of the pipe wall material are given as $\mu_S = 2.75$ MPa and $\mu_R = 100$ MPa, respectively, and an alternative design situation is specified as, the mean design pressure and mean yield strength of the pipe wall material are $\mu_S = 6$ MPa and $\mu_R = 400$ MPa, respectively. For the first design situation, the design constant corresponding to $\beta_T = 2$, is obtained using Eq. 4.7 as $h = 24.25$. The same reliability level for the alternative design case can also be demonstrated by choosing the design constant $h = 44.44$. Both the design situations demonstrating same reliability are illustrated graphically in figure 4.1.

The design equation (Eq. 4.11) in terms of partial factors provide an alternative

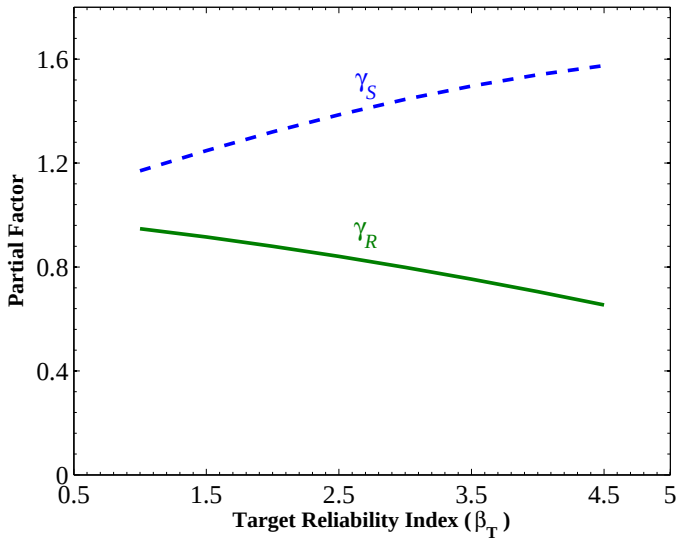

Figure 4.2: Partial safety factors for different reliability indices

efficient method to facilitate the process of new pipe design as well as the assessment of an existing pipe for specified safety levels. The method is illustrated as follows.

Figure 4.2 plots partial factors versus β_T, which were computed for a set of COVs specified as $\delta_R = 0.1$ and $\delta_S = 0.2$. These can be used in designing a new pipe or assessing the reliability of an existing pipe.

Consider designing the wall thickness of a pipe of diameter $d_0 = 203.2$ mm for a reliability index $\beta_T = 4$. The mean design pressure and mean yield strength of the pipe wall material are given as $\mu_S = 5.5$ MPa and $\mu_R = 200$ MPa, respectively. For $\beta_T = 4$, partial factors are calibrated as $\gamma_R = 0.705$ and $\gamma_S = 1.54$. Substituting these parameters in Eq. 4.11, the wall thickness is computed as $w = 5.96$ mm.

The partial factors can also be used to asses the adequacy of an existing pipeline in the following way. Suppose some inspection data show that the pipe thickness $w = 5$ mm, actual $\mu_R = 190$ MPa and mean applied pressure is $\mu_S = 4.9$ MPa.

Using partial factors for $\beta_T = 4$ in Eq. 4.11, we find that $g(r, s) = -16.36 < 0$, which means the that reliability index is less than 4. By using $\gamma_R = 0.798$ and $\gamma_S = 1.445$ for $\beta_T = 3$, it can be shown that $g(r, s) = 10.72 > 0$. It means that actual $\beta > 3$.

The reliability-based calibration of partial factors is exact for limit state functions involving linear combinations of normally distributed random variables. In case of nonlinear limit states and non-normal random variable, approximate and iterative methods have been developed for computing β and associated partial factors (Nowak 1983, Nowak et al. 1979, Madsen et al. 1986). Surprisingly, approximate algorithms are highly accurate and they have served well in the development of load and resistance factor design of structures under a wide variety of limit state functions (Allen et al. 2005, Nowak 1995, Nowak et al. 2001).

4.3 Partial Factors for DHC Initiation Analysis

In chapter 3, explicit limit state equation is formulated for probabilistic DHC initiation analysis. To compute the conditional DHC initiation probability ($\mathrm{P}[C_{in}|H]$), a limit state function is defined as

$$G(R, S) = K_{IH} - d_1 \ (0.0135 + 0.0828 \times a - 0.0013 \times c) \tag{4.12}$$

such that $\mathrm{P}[G(R, S) \leq 0]$ signifies the conditional probability of DHC initiation given H, where d_1 is a design constant as given in Eq. 3.23.

In the defined limit state Eq. 4.12, the random variable K_{IH} (MPa$\sqrt{\mathrm{m}}$) is formulated as normally distributed quantity with parameters $\mu_{K_{IH}} = 6.62$ MPa$\sqrt{m}$ and $\sigma_{K_{IH}} = 0.911$ MPa$\sqrt{m}$ and random variables a and c are modeled as lognormally

Table 4.1: Calibration of partial factors for different probabilities of DHC initiation

P_f	β	a^*	c^*	k^*_{IH}	$a^*\%$	$c^*\%$	$k^*_{IH}\%$	γ_a	γ_c	$\gamma_{K_{IH}}$
10^{-2}	2.326	0.375	1.074	5.613	97.96%	47.03%	13.46%	2.153	0.921	0.848
10^{-3}	3.090	0.499	1.074	5.297	99.68%	47.02%	7.32%	2.861	0.921	0.800
10^{-4}	3.719	0.628	1.076	5.020	99.95%	47.15%	3.95%	3.601	0.922	0.758

distributed variables. The parameters are provided in Table 3.1.

4.3.1 DHC Initiation Assessment Equation

The following equation is proposed for the semi-probabilistic assessment of DHC initiation from a planar flaw at full power operating condition:

$$G_{DHC}(\mu_{K_{IH}}, \mu_{K_I}) = \gamma_{K_{IH}}\ \mu_{K_{IH}} - d_1\ (0.0135 + 0.0828\ \gamma_a\ \mu_a - 0.0013\ \gamma_c\ \mu_c) \quad (4.13)$$

Partial factors associated with random variable a, c and K_{IH} are denoted as γ_a, γ_c, and $\gamma_{K_{IH}}$ respectively. The mean values are taken as nominal values of a, c, and K_{IH}, though can be changed to any other suitable percentile values.

4.3.2 Results and Discussion

For calibration coefficient of variation ($\delta = \mu/\sigma$) for the variables are taken as $\delta_a = 0.4364$, $\delta_c = 0.3485$, and $\delta_{K_{IH}} = 0.1376$. Corresponding to these specified coefficient of variation, calibrated partial factors for various orders of the probability of DHC initiation are presented in figure 4.3. Additional information on design points are presented in Table 4.1.

Some interesting observations can be made from the results given in Table 2.

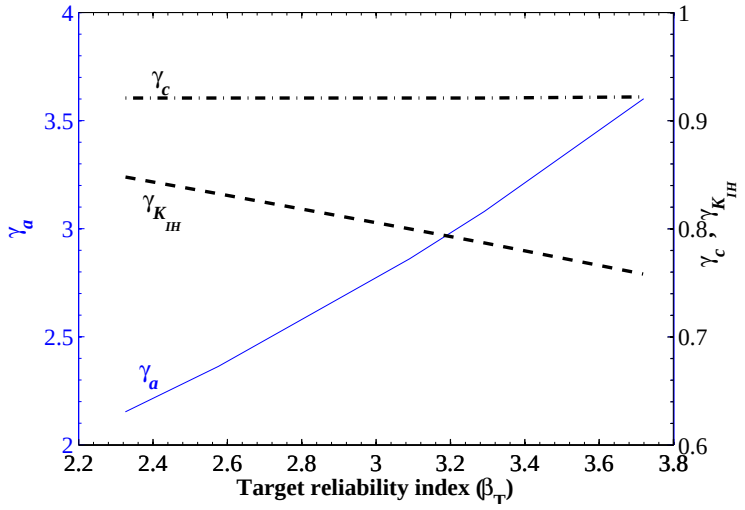

Figure 4.3: Partial safety factors vs target reliability indices for DHC initiation

The design point a^* varies approximately from 98% to 99.95% and design point c^* almost remains constant at 47% percentile of their distributions, respectively. The design point k^*_{IH} varies from 5.02 MPa$\sqrt{}$m to 5.613 MPa$\sqrt{}$m. However, CSA lower bound DHC initiation toughness (4.5 MPa$\sqrt{}$m) is much lower than these associate design point. Moreover, design point of the flaw depth a^* varies approximately from 98% to 99.95%, suggesting that the heuristic assumption of upper bound flaw depth (a) at constant 97.5% upper quantile is not appropriate. The most important observation is about the design point associated with half crack length (c). CSA prescribes the use of 97.5% upper bound value of c for deterministic assessment. However, the current analysis reveals that the probabilistic bound for c is almost remains constant at about 47% quantile.

4.3.3 Application

Consider now an illustrative case of DHC initiation assessment of a PT with target reliability 10^{-2}. Suppose surveillance data shows that μ_a= 0.1 mm and μ_c= 1 mm. Assume the mean of DHC initiation toughness remains same i.e. $\mu_{K_{IH}}$= 6.62 MPa. Under the assumption that the co-efficient of variation of all the variables has not changed significantly from the corresponding values taken in calibrating the partial factors, the same set of partial factors can be used for assessment. Partial factors for this case are taken from Table 4.1 as γ_a= 2.153, γ_c= 0.921 and $\gamma_{K_{IH}}$= 0.848. For the full power condition(p = 8.9 MPa) and assumed PT dimensions (r_i and w), the design constant d_1 is computed as 137. Substituting the values of partial factors, design constant d_1 and mean values in Eq. 4.13, gives G_{DHC}(=1.486)<0. It implies that $P[C_{in}|H] > 10^{-2}$. Thus the probability requirement for DHC initiation is satisfied for the specified target reliability level.

4.4 Partial Factors for LBB Analysis

In chapter 3, explicit limit state equation is formulated for probabilistic LBB analysis. First the time axis is discretized as $x_1, x_2, \cdots, x_n$ and suitable pressure (p_i) and temperature (t_i ^{o}C) are assigned to each interval from the RSDT shown in figure 3.2. The condition for LBB, i.e. a growing crack does not become unstable during the RSDT, is specified in CSA N285.8 (2005) as

$$2c(x_i) \leq 2CCL(x_i) \quad (\text{for all}\, i = 1, n) \tag{4.14}$$

where $2c$ and $2CCL$ denote the length of growing DHC through-wall crack and the critical crack length, respectively. A typical LBB analysis consists of a sequence

of events in which size of the crack ($2c$) is calculated step by step and compared with the critical crack length ($2CCL$) during the RSDT cycle. This step by step calculation is required to account for changes in the pressure and temperature in RSDT, because a sub critical flaw under hot pressurized conditions could become critical at a reduced temperature due to reduction in the fracture toughness. For partial factor calibration for target BBL probability, a limit state function in the form of stress and strength variable is defined as follows

$$G(R, S, x_i) = R(x_i) - S(x_i) \tag{4.15}$$

Note $P[G(R, S, x_i) \leq 0]$ signifies the cumulative probability of PT rupture in the time interval from 0 to x_i, where R is critical crack length (resistance) and S is the actual growing DHC crack length (stress). The overlap of the two distributions (R and S) implies that there is a finite probability that the actual crack length could exceed the critical length and cause the PT to rupture.

As shown in figure 3.15, the critical length at the full power condition has the smallest mean value; later in RSDT it increases as the pressure deceases. The increases in $R(x_i)$ are followed by decreasing trend, but it does not fall below the baseline value at full power condition. Thus, the critical crack length can be conservatively taken as a constant R_0 given in Eq. 3.40 for the entire RSDT. This simplifies the limit state equation for computing the probability of BBL as

$$G(R, S) = 2[-66.88 + 3.65\,K]^{0.588} - s_0 - 120,000\ V\ d(x_n) \tag{4.16}$$

The unit of V is m/s and x_i is in minutes. For the RSDT shown in figure 3.2, $d(x_n)$=264.064, calculated by taking x_i in minutes and temperature t in ^{o}C. The initial penetration length is $s_0 = 20$ mm.

In the above limit state equation, the random variable V stands for DHC velocity at full power operating condition ($t = 293\ ^{o}$C). V (m/s) is formulated in the form of a logarithmic regression model (Eq. 4.17) with parameters $m_V = 6.3315 \times 10^{-7}$ m/s and $\sigma_{lnV} = 0.14428$.

$$\ln[V] = \ln[m_V] + \sigma_{lnV}\ U \tag{4.17}$$

Similarly, random variable K is fracture toughness at full power operating condition. K is also modeled as a lognormal random variable (Eq. 4.18) with parameter $m_K = 104.5327$ MPa $\sqrt{\text{m}}$ and $\sigma_{lnK} = 0.1834$.

$$\ln[K] = \ln[m_K] + \sigma_{lnK}\ U \tag{4.18}$$

4.4.1 LBB Assessment Equation

The following equation is proposed for the semi-probabilistic assessment of LBB :

$$G_{LBB}(\mu_K, \mu_V) = 2[-66.88 + 3.65 \times \gamma_K\, \mu_K]^{0.588} - 20 - 120,000\ \gamma_V\, \mu_V\ d(x_{end}) \tag{4.19}$$

Partial factors associated with K and V are denoted as γ_K and γ_V, respectively. The mean values are taken as nominal values of K and V.

4.4.2 Results and Discussion

Calibrated partial factors for various orders of the probability of PT rupture are plotted in figure 4.4 and additional information is presented in Table 4.2. Since $d(x_n)$ is a non-random quantity, the proposed assessment Eq. 4.19 is applicable to other shutdown transient cycles.

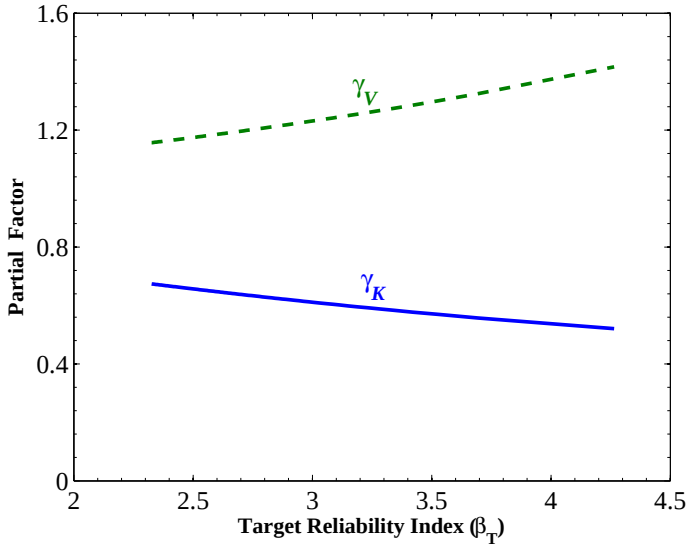

Figure 4.4: Calibrated partial factors for different target reliability indies

Allowable pressure tube failure frequencies per year for a reactor core, are presented in Table 2.2 as specified in Table C.1 of CSA N285.8 (2005), vary from 10^{-2} to 10^{-3} depending on the core type and the number of active degradation mechanisms. Partial factors corresponding to these target probabilities are given in Table 4.3. In the present context, these specified probabilities can serve as conservative upper bounds. The reason is that the target probability in the current analysis is a conditional probability (P$[BBL|C_{in}]$), which assumes the presence of a through wall crack and ignores the probability of crack initiation. Thus P$[BBL|C_{in}] <$ P$[BBL]$, if P$[C_{in}] < 1$.

Some interesting observations can be made from the results given in Table 4.3. In case of Type 1 core with no degradation mechanism, the design point of fracture toughness ($k^* = 71.8$ MPa$\sqrt{\text{m}}$) and the CSA lower bound (72 MPa$\sqrt{\text{m}}$) are almost the same. However, the associated design point of DHC velocity (v^*) is

Table 4.2: Calibration of partial factors for different probabilities of PT rupture

P_f	β	k^* (MPa$\sqrt{\text{m}}$)	v^* (m/s)	k^*(%)	v^* (%)	γ_K	γ_V
10^{-2}	2.326	71.641	9.06E-07	1.975%	86.054%	0.674	1.157
10^{-3}	3.09	64.174	8.50E-07	0.392%	94.234%	0.603	1.242
10^{-4}	3.719	59.069	7.95E-07	0.093%	97.925%	0.555	1.328
10^{-5}	4.265	55.342	7.40E-07	0.026%	99.353%	0.520	1.416

Table 4.3: Partial factors for LBB corresponding to safety levels specified in CSA N285.8 (2005)

TYPE I CORE								
j	P_f	β	k^*(MPa$\sqrt{\text{m}}$)	v^* (m/s)	k^* (%)	v^* (%)	γ_K	γ_V
0	0.01	2.326	71.896	7.44×10^{-7}	0.021%	0.868%	0.676	1.163
1	0.005	2.576	68.776	7.52×10^{-7}	0.011%	0.884%	0.647	1.176
2	0.0025	2.807	65.948	7.59×10^{-7}	0.006%	0.895%	0.620	1.186
3	0.00167	2.934	64.415	7.62×10^{-7}	0.004%	0.901%	0.606	1.191
TYPE II CORE								
j	P_f	β	k^*(MPa$\sqrt{\text{m}}$)	v^*(m/s)	k^* (%)	v^* (%)	γ_K	γ_V
0	0.033	1.838	78.203	7.25×10^{-7}	0.057%	0.826%	0.736	1.133
1	0.0165	2.132	74.374	7.37×10^{-7}	0.032%	0.853%	0.699	1.152
2	0.00825	2.397	70.997	7.46×10^{-7}	0.017%	0.873%	0.668	1.167
3	0.0055	2.543	69.186	7.51×10^{-7}	0.012%	0.882%	0.651	1.174

Type I core → *Design basis core*
Type II core → *Updated assessment that demonstrates acceptability of an initiating event failure frequency that is equal to the total allowable value of 0.033 events per reactor year*
$\boldsymbol{j}$ → *Number of known in-service pressure tube degradation mechanism*

87% percentile, which is less conservative than the CSA upper bound of 97.5%. In case of two active degradation mechanisms, the design point of fracture toughness decreases to $k^* = 66$ MPa$\sqrt{}$m and v^* slightly increases to 89.5% percentile.

In case of Type 2 core with less than two active degradation mechanisms, current results clearly reveal conservatism associated with the deterministic methodology. Here, k^* is higher than the CSA lower bound, whereas v^* is lower than the CSA upper bound. Even in case of two active degradation mechanisms, $k^* = 71$ MPa$\sqrt{}$m and the CSA lower bound are fairly close, yet v^* is 87%.

In all the cases given in Table 4.3, design point of the DHC velocity v^* does not exceed 90% percentile of its distribution, suggesting that the CSA upper bound is in general fairly conservative than the probabilistic upper bound.

4.4.3 Application

Consider the LBB assessment of a Type II core with 3 active degradation mechanisms. Suppose surveillance data show that mean fracture toughness $\mu_K = 100$ MPa$\sqrt{}$m, and mean DHC velocity as $\mu_V = 6 \times 10^{-7}$ m/s. Partial factors for this case are taken from Table 4.3 as $\gamma_K = 0.65$ and $\gamma_V = 1.17$. Substituting these in Eq. 4.19, lead to $G_{LBB}(= 18.8) > 0$. It implies that $P_f < 5.5 \times 10^{-3}$. Thus the LBB requirement is satisfied at the specified reliability level.

4.5 Conclusions

This chapter presents an innovative semi-probabilistic method for flaw assessment in which the deterministic criterion of CSA Standard N285.8 (2005) is calibrated to a target probability of failure using the concept of partial factors. The main

advantage of the proposed approach is that it retains the simplicity of deterministic method, yet it provides a practical risk-informed basis for flaw assessment.

This chapter clearly presents concepts underlying the process of calibrating a deterministic criterion to a specified probability level. The conversion is based on replacing the random variables by probabilistic bounds determined from a formal reliability analysis. A probabilistic bound (or design point) is obtained as a product of nominal value of the random variable (such as mean) with a calibrated partial factor. Since the calibration process accounts for interaction among random variables and their sensitivity to the assessment criterion, probabilistic bounds are consistent with a specified reliability level, whereas bounds chosen heuristically or based on experience will lack this consistency.

This chapter defines the limit state function for DHC initiation analysis and LBB analysis formulated in chapter 3 and computes partial factors using the First-Order Reliability Method, which is highly efficient over the simulation method. Partial factors are computed for a range of target probabilities of DHC initiation and BBL as specified in Table C.1 of CSA Standard N285.8 (2005). In DHC initiation analysis the method defines probabilistic bounds on DHC initiation toughness K_{IH} and flaw dimensions a and c. Similarly, in LBB analysis it defines bounds on fracture toughness (K_c) and DHC velocity (V).

In DHC initiation analysis, the CSA Standard N285.8 (2005) specifies a 97.5% percentile upper bound on a and c to compute upper bound K_I, whereas probabilistic analysis shows a^* fluctuates from 98% to 99.95% and c^* remains almost constant at 47%. The probabilistic lower bound K_{IH} is higher than 5 MPa$\sqrt{}$m for almost all the cases whereas the CSA lower bound is 4.5 MPa$\sqrt{}$m. In this sense, the CSA lower bound K_{IH} and heuristic assumption of upper bound c at 97.5% are not appropriate. In LBB analysis, The CSA Standard N285.8 (2005) specifies a

97.5 % percentile upper bound on V, whereas probabilistic upper bound does not exceed 90% percentile. In this sense, the CSA upper bound V is more conservative. The lower bound K_c varies from 78 to 64 MPa$\sqrt{}$m depending on the type of core and the number active degradation mechanisms.

This proposed approach is generic and it can be adopted to any other probabilistic assessment. The proposed semi-probabilistic approach avoids complex and involved simulations, and offers an alternative practical tool for risk-informed assessment of reactor components.

Chapter 5

Probabilistic Sample Size Analysis

5.1 Introduction

In any probabilistic assessment, parametric probability distribution models for each random variables is required. Further, the parameters of the assumed parametric probability distributions are computed from the available inspection data through estimation technique, e.g. maximum likelihood method (Lawless 2003).

In practical situations, where the model fitting and parameter estimation are based on finite sample sizes, there will remain uncertainty in the estimated parameter values as well as in the validity of the distribution model itself. The uncertainty in probabilistic assessment can be divided in two types: (1) statistical or sampling uncertainty and (2) model uncertainty. Statistical uncertainty is associated with failure to estimate the model parameters with precision and can be virtually eliminated at the expense of a very large sample size. The model uncertainty is the failure to assume the best distribution model with precision and can also be eliminated with sufficient large sample size. Thus it is clear that the assumption of

specific probability distribution models and the computation of parameters from the limited inspection data could affect the results of probabilistic analysis. With a reasonably accurate parametric probability distribution model, the uncertainty in the estimated parameters depends on the number of inspection data. With adequate number of sampling data points, the uncertainty in distribution modeling and hence uncertainty in probability estimation can be reduced to an acceptable level.

The nuclear power plant systems are not readily accessible to inspection and data collection due to high radiation and large inspection costs. For pressure tubes, in-service inspection of a small sample of PT is performed at periodic intervals (Table 2.1). The probabilistic assessment of flaws in PTs of CANDU reactors is therefore confounded by large sampling uncertainties. Hence, the determination of size of flaw samples required during a periodic inspection is an important issue.

In this chapter, the sampling error associated with a finite small sample data is investigated and a risk informed approach is proposed to define the required sample size for inspection. The approach is illustrated with an example DHC initiation assessment from a flaw.

5.2 Sampling Uncertainty

In applying statistical inference theory, a sufficiently large number of samples are highly desirable for accurate estimation of the parameters of the probability distributions. If the sample size is not large enough, a significant uncertainty is associated with the estimated parameters. The basic assumption in a parameter estimation technique is, the sample points are random and they are statistically independent. The most common requirement for selecting the best estimator (Ochi 1989) is: the

expected value of the estimator ($\hat{\theta}$) should be equal to the true θ i.e. $E(\hat{\theta}) = \theta$. The estimated parameter which satisfies this condition is called unbiased estimator.

Obviously, the larger the sample size, the more accurate is the estimation of the unknown model parameters. The uncertainty in the estimated parameter is actually a function of number of sample size (n). This is illustrated through an example in the following section.

5.2.1 Illustration

Consider a two parameter normal distribution described by its PDF

$$f_X(x|\mu,\sigma) = \frac{1}{\sigma\sqrt{2\pi}} \exp\left[-\frac{1}{2}\left(\frac{x-\mu}{\sigma}\right)^2\right] \tag{5.1}$$

Suppose the inspection sample points $x_i, i = 1, \ldots, n$ are independent and identical samples of X of size n. The likelihood function for parameter inference for this case is

$$L = \left(\frac{1}{2\pi\sigma}\right)^{n/2} \exp\left[-\frac{1}{2\sigma^2}\sum_{i=1}^{n}(x-\mu)^2\right] \tag{5.2}$$

and the maximum log-likelihood estimations are

$$\frac{\partial}{\partial\mu}\ln(L) = 0, \quad \Rightarrow \hat{\mu} = \frac{1}{n}\sum_{i=1}^{n} x_i \tag{5.3}$$

$$\frac{\partial}{\partial\sigma^2}\ln(L) = 0, \quad \Rightarrow \hat{\sigma}^2 = \frac{1}{n}\sum_{i=1}^{n}(x_i-\hat{\mu})^2 \tag{5.4}$$

To be unbiased, it should demonstrate $E(\hat{\mu}) = \mu$ and $E(\hat{\sigma}^2) = \sigma^2$. The estimated maximum log-likelihood parameters gives

$$\begin{aligned} E(\hat{\mu}) &= \mu \quad \text{and} \\ E(\hat{\sigma}^2) &= \frac{n-1}{n}\sigma^2 \end{aligned} \tag{5.5}$$

Thus the estimator $\hat{\sigma}^2$ does not satisfy the unbiased requirement. To be unbiased, the estimator $\hat{\sigma}^2$ is reformulated as

$$\hat{\sigma}^2 = \frac{1}{n-1}\sum_{i=1}^{n}(x_i - \hat{\mu})^2 \tag{5.6}$$

Further, analysis shows that the estimated parameters are also random variables and follow their own distributional property. The estimator $\hat{\mu}$ follows normal distribution with mean μ and variance σ^2/n and the variance estimator is given by $\hat{\sigma}^2 = \frac{\sigma^2}{n-1}\chi^2(n-1)$, where $\chi^2(n-1)$ is chi-square distribution with $n-1$ degrees of freedom (Desu et al. 1990). It is apparent that the distributional property of the estimated parameters depends on the sample size n. Therefore, it is highly desirable that some measure of assurance in the estimation should be reflected in the estimator. In this context, confidence intervals (CI) on the estimated parameters as a function of sample size n is suggested (Benjamin et al. 1970). If the parent distribution follows normal distribution with known variance σ, the $(1-\alpha)\%$ CI about the true or population mean can be stated as

$$\hat{\mu} - u_{\alpha/2}\frac{\sigma}{\sqrt{n}} \leq \mu \leq \hat{\mu} + u_{\alpha/2}\frac{\sigma}{\sqrt{n}} \tag{5.7}$$

where $u_{\alpha/2}$ is defined to be that value such that $1 - \Phi(u_{\alpha/2}) = \alpha/2$, Φ is the CDF of standard normal variable.

For example consider a normally distributed random variable, X, described by its PDF $f(x|\mu_X, \sigma_X)$. The true parameters of the parent distribution is given as mean $\mu_X = 100$ and standard deviation $\sigma_X = 10$. To illustrate the sampling uncertainty associated with finite small sample data, let us simulate n number of observations from the parent distribution $f(x)$. The resulting set of n realizations $(x_1, x_2, ..., x_n)$ will yield a set of parameters of the distribution. Further, if we repeat the test m number of times, we will get m different sets of observations. Each set of observation of n realizations will yield a different pair of estimated parameters. Finally, we will get m different pairs of estimated mean and variance $(\hat{\mu}_{X_1}, \hat{\sigma}_{X_1})$, $(\hat{\mu}_{X_2}, \hat{\sigma}_{X_2})$, ..., $(\hat{\mu}_{X_m}, \hat{\sigma}_{X_m})$. In reality, $\hat{\mu}_X$ and $\hat{\sigma}_X$ are distributed quantities as shown in figure 5.1 and 5.2, respectively. However, a reasonably high sample size will give an accurate estimation of the parameters (Fig. 5.1-5.2).

Consider now the statement concerning the CI of the mean when the true standard deviation σ (=10) is known. Suppose, we have a set of 25 observed values of the variable X and the estimated mean is computed as $\hat{\mu}_X = 102.1816$. We can still make a probability statement regarding the likelihood that the true mean will be within certain limits about the estimated mean. For example, the 95% predicted confidence interval on the actual mean μ_X computed using Eq. 5.7 is: $98.2616 \leq \mu_X \leq 106.1015$.

5.3 Probabilistic DHC Initiation Model

Complete formulation of the probabilistic DHC initiation assessment model form a planar flaw is presented in chapter 3. To estimate the conditional probability of

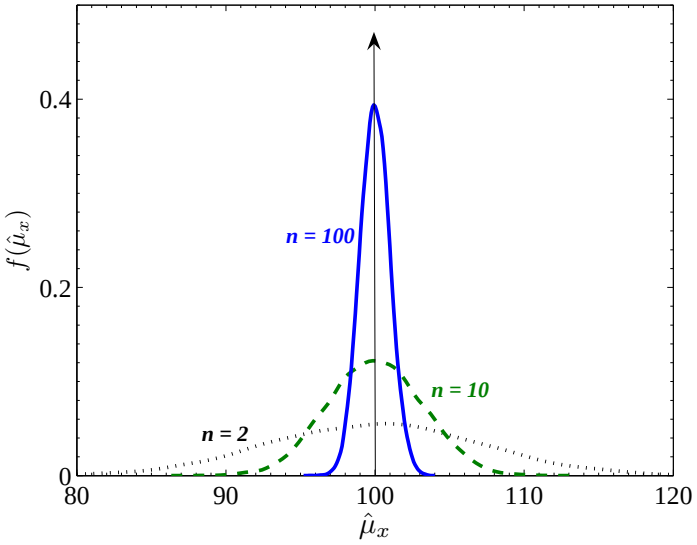

Figure 5.1: Distribution of $\hat{\mu}_X$ for $n = 2$, 10, 100

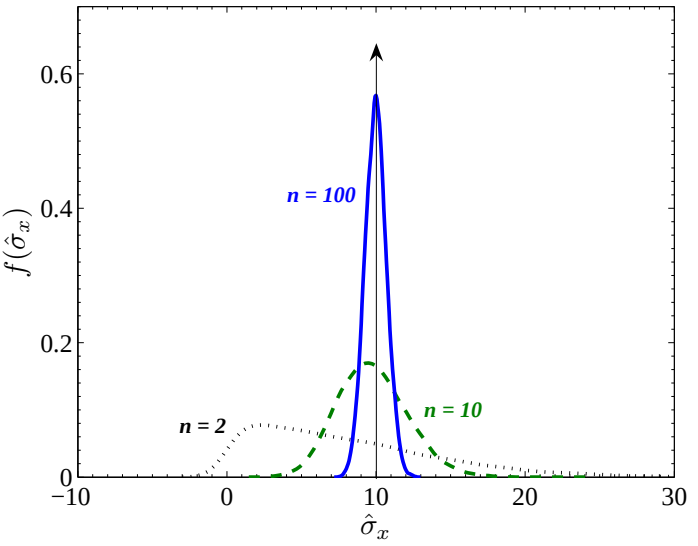

Figure 5.2: Distribution of $\hat{\sigma}_X$ for $n = 2$, 10, 100

DHC initiation ($P[C_{in}|H]$) given H, a limit state function is defined as

$$G(K_{IH}, a, c) = K_{IH} - d_1\ (0.0135 + 0.0828 \times a - 0.0013 \times c)$$

where d_1 is a deterministic constant given by Eq. 3.23, the distributional property along with parameters of the random variables K_{IH}, a, c is presented in Table 3.1. At full power operating condition ($p = 8.9$ MPa) the probability is estimated as $P[C_{in}] = 1.494 \times 10^{-2}$.

5.4 Sample Size Analysis

The main purpose of probabilistic reactor core assessment is to assess the uninspected reactor based on the test data gathered from the inspected reactor. Whenever a new reactor is inspected, the new flaw data sets are obtained and the probabilistic assessment is performed using the new data sets.

The uncertainty in probability estimation can be reduced with large inspection data. However, the inspection costs associated with PTs is significant. Therefore, a balance has to be maintained between inspection sample size and statistical uncertainty or prediction error in the estimation of probability. What is the optimal inspection samples required so that a reasonably accurate prediction of probability can be estimated is an important issue? In this section a two step risk informed approach is presented to decide on the required inspection sample size based on allowable prediction error. The solution to this problem is considered in two parts (1) confirmatory and (2) exploratory, as defined below:

(1) Confirmatory:

Confirm that the mean values of the newly inspected flaw dimension data has not

changed significantly from the mean value of the referenced parent distributions. Determine approximate sample size required to test with confidence that the mean of the new inspection samples do not vary from the mean of the referenced parent distributions.

If the mean value of the newly inspected flaw samples is the same as the referenced parent distributions, then probability information inferred with the referenced distribution do apply for the new inspection region.

(2) Exploratory:

If there is a significant change in the mean of newly inspected flaw data from the mean of the population or referenced parent distributions, then new model parameters are need to be estimated with the new sample data. In this case, explore the possible risk impact of using the small sample data in probability estimations. Determine the sample size required to evaluate probability of DHC initiation using the newly fitted distributional parameters with an acceptable amount of prediction error.

5.4.1 Confirmatory Analysis

To confirm whether the mean of the new inspection sample data is same as the referenced mean value, hypothesis tests about the location parameters are prescribed in literatures (Benjamin et al. 1970, Daniel, 1990). In the following, without loss of generality, we consider the mean value of the variables follow normal distribution and the steps for the test of hypothesis is presented below.

Test for Mean

Suppose that a population with unknown mean μ is thought to have some specific mean value, say μ_0. Let us define the null hypothesis and the corresponding alternative as follows:

$$H_0 : \quad \hat{\mu_0} = \mu, \quad H_1 : \quad \hat{\mu} \neq \mu_0 \tag{5.8}$$

Let n sample observations are designated as $x_1,\ x_2,\ \ldots,\ x_n$ and the sample mean value is estimated as $\hat{\mu} = (1/n)\sum_{i=1}^{n} x_i$. The statistic $\hat{\mu}$ is assumed to follow normal distribution with mean μ and standard deviation $\sigma/\sqrt{n}$, where σ is the known population standard deviation. The test statistic for the test is defined as

$$U = \frac{\hat{\mu} - \mu_0}{\sigma/\sqrt{n}} \tag{5.9}$$

The test statistics U follows normal distribution with zero mean and unit standard deviation.

When conducting a statistical test, two types of error must be considered: type-I error(false positive) and type-II (false negative), with probabilities (α and β, respectively. Type-I error (α) is defined as the probability of rejecting the null hypothesis when it is true and type-II error (β) is the probability of accepting the null hypothesis when it is not true. The term $1-\alpha$ is called the confidence interval and $1-\beta$ is known as the power of the test. The significance level α actually defines the unlikely values of sample statistics when the null hypothesis is true. In other words it defines the critical/rejected region of the test when the null hypothesis is true. For a two tail test and assumed significance level, say α, the critical value of

the test statistic is computed as

$$U_{\alpha/2} = \Phi^{-1}\left(\frac{\alpha}{2}\right) \tag{5.10}$$

where Φ is the cumulative distribution function of a standard normal variable with mean zero and unit standard deviation.

If the sample test statistic U falls in the rejected region, then the null hypothesis is rejected. In other words, if $U > U\alpha/2$, then the assumption of null hypothesis that $\hat{\mu} = \mu$ is rejected and thus the mean of the sample is considered to be different than the hypothesized mean value at α significance level.

As discussed earlier, in making a decision about the hypothesis two types of error can be made type-I and type-II. Though at α significance level we can accept accept a certain null hypothesis, there is still certain probability (β) that a wrong decision is taken. For example if the actual mean is $\mu_1 (\neq \mu_0)$, with a probability of error β, the decision $\hat{\mu} = \mu$ can still be accepted at α probability of type-I error (Fig. 5.3). Type-I and type-II errors exhibit inverse relationship. If we reduce probability of one, other goes up. Thus, it is always better to keep a balance between the two errors.

Usually, when a statistical test is conducted, the probability of type-I error is specified by the investigator. However, the probability that a significant result will be obtained if a real difference (μ_1) exists (i.e., the power of the test, $(1-\beta)$ depends largely on the total sample size n. As one increases n the spread of the distributions decreases thus the type-II error decreases (or power of the test increases). This information is valuable in defining the total sample size required for the test. In other words, the total sample size (n) required for the statistical test can be defined by deciding on the significance level and power of the test. The steps of sample size

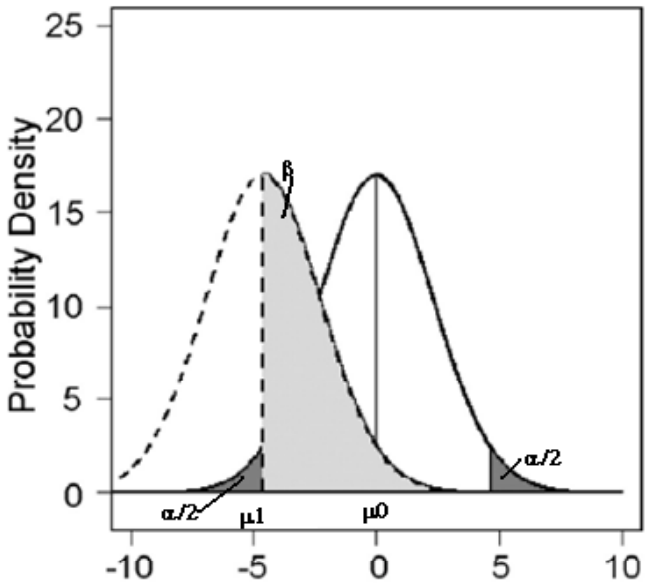

Figure 5.3: Illustration of type I and type II error in statistical hypothesis testing

estimation procedure is as follows:

The parameters involved in the problem are α, β, μ, μ_1, σ and σ_1. Define the null and alternative hypothesis

$$H_0 : \quad \hat{\mu} = \mu, \quad H_1 : \quad \hat{\mu} = \mu_1 \tag{5.11}$$

The test statistics is

$$U = \frac{\hat{\mu} - \mu}{\sigma/\sqrt{n}} \tag{5.12}$$

Decide the type-I and type-II error at desired level i.e. α and β, respectively. Satisfy

the condition

$$\begin{aligned} \mathrm{P}[U > U_{\alpha/2}|H_0] &= \alpha/2 \quad \text{and} \\ \mathrm{P}[U > U_{\alpha/2}|H_1] &= 1-\beta \end{aligned}$$

This leads to

$$\begin{aligned} \frac{\hat{\mu}-\mu}{\sigma/\sqrt{n}} &= U_{\alpha/2} \quad \text{and} \\ \frac{\hat{\mu}-\mu_1}{\sigma_1/\sqrt{n}} &= U_{\beta} \end{aligned}$$

Further assuming, $\sigma_1 = \sigma$, and solving we get

$$|\mu_1 - \mu| = \frac{(U_{\alpha/2} - U_{\beta})\sigma}{\sqrt{n}} \quad \text{or} \tag{5.13}$$

$$n = \left[(U_{\alpha/2} - U_{\beta}) \left(\frac{\sigma}{|\mu_1 - \mu|} \right) \right]^2 \tag{5.14}$$

Let us define a single parameter which reflects the difference in the null and alternate hypothesis (i.e. $\mu_1 - \mu$) and the population standard deviation (σ) as

$$\triangle_{\delta} = \frac{\sigma}{|\mu_1 - \mu|} \tag{5.15}$$

The sample size can now be formulated in terms of $\triangle_{\delta}$ as

$$n = \left[(U_{\alpha/2} - U_{\beta}) \triangle_{\delta} \right]^2 \tag{5.16}$$

Typical result of the above sample size formulation at 10% significance level (i.e. $\alpha = 0.1$) is as shown in figure 5.4. It is apparent from figure 5.4 that the number

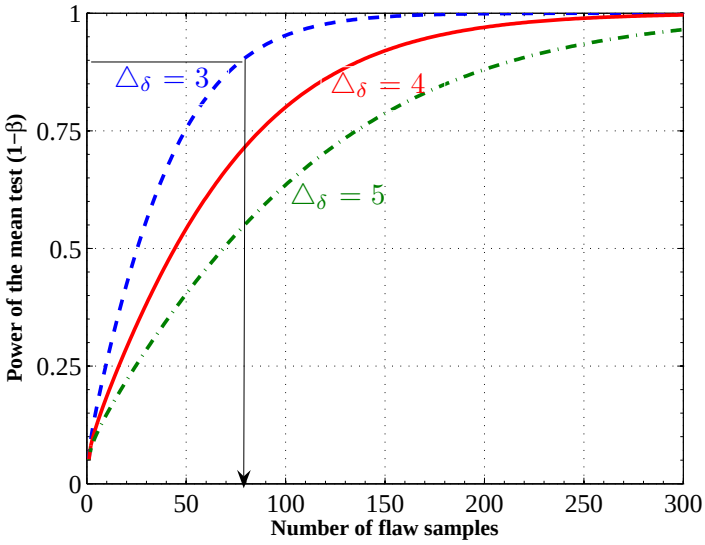

Figure 5.4: Sample size n vs power of the mean test

of sample observation increases with the increase in coefficient of variation of the variable. For illustration, suppose we are interested to test the mean of a variable which has coefficient of variation 0.3 against the alternative mean with 10% variation from the hypothesized mean, then the parameter $\triangle_\delta$ is 3. At power of the test 90%, as shown in figure 5.4, we need at least 80 observations to perform the mean hypothesis test at 10% significance level. Further, assuming a typical value of 10 flaws per pressure tube, 8 PTs are required to be inspected for flaws.

5.4.2 Exploratory analysis

If the confirmatory analysis fails to satisfy the null hypothesis i.e. if there is a significant change in the mean parameter of newly inspected flaw data from the referenced mean parameter of the population or parent distributions, then new model parameters are need to be estimated with the new sample data. Since, the

number of inspected components are small, the estimated parameters are actually confounded by the sampling uncertainty. It is known that, the parameters of fitted distributions follow their own distributional property. With a very few sample data points, the uncertainty associated with the estimated parameters may be reasonably high. In this case, it is necessary to explore the possible risk impact of using the small sample data in probability estimations.

To investigate the possible uncertainty associated with the estimated parameters of the flaw dimensions, random flaw dimensions are simulated from the known parent distributions. The parent distribution and true parameters are taken as given in Table 3.1. These simulated sample flaw data are then used to calculate the parameters of the model statistical distributions. The mean upper and lower quantile values of the estimated parameters along with the true distributional parameters are plotted in figure 5.5-5.6.

Though the mean estimated parameters with finite small samples are nearly same as the true parameter of the parent distribution, there is a considerable amount of variance is associated (Fig. 5.5- 5.6).

Consequently, the computed probability will also be affected by sampling uncertainty. Since, we use the estimated parameters fitted with a small number of simulated flaw data, the uncertainty associated with the estimated parameters will lead to uncertainty in the computed probability of DHC initiation ($\hat{\mathrm{P}}[C_{in}]$). The computed parameters from the simulated small sample flaw data, is the used to calculate the uncertainty in probability of DHC initiation as shown in figure 5.7.

It is apparent from figure 5.7 that though the mean value of the calculated probability of DHC initiation with small number of sample flaws is almost same as that of the true probability of DHC initiation, there is significant uncertainty

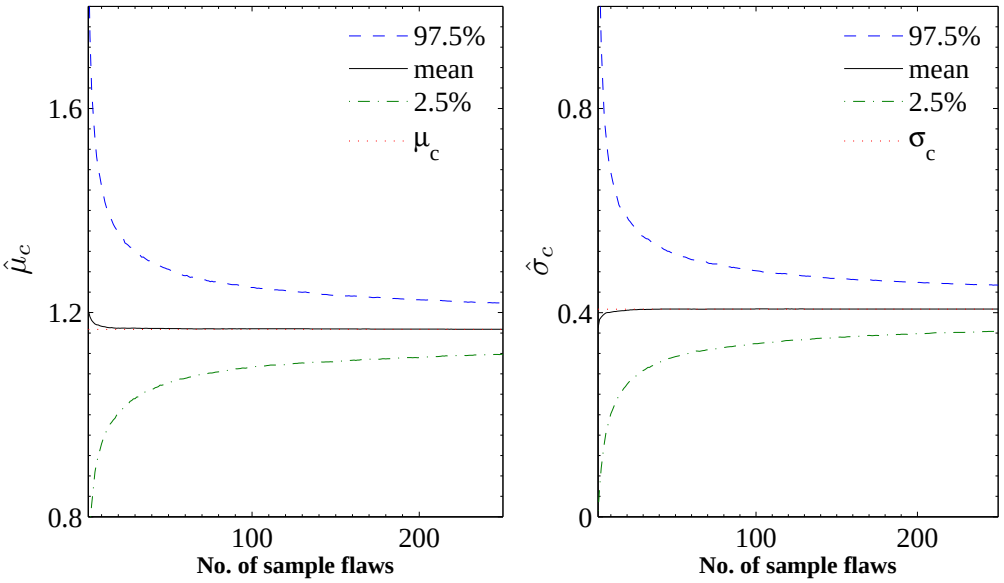

Figure 5.5: Sampling uncertainty in the estimated parameters of c

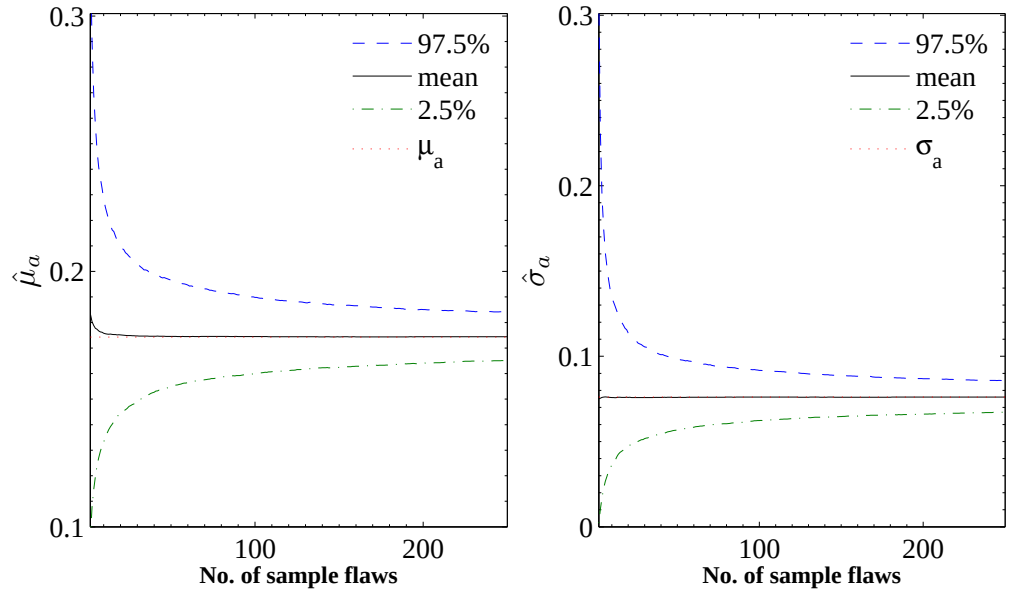

Figure 5.6: Sampling uncertainty in the estimated parameters of a

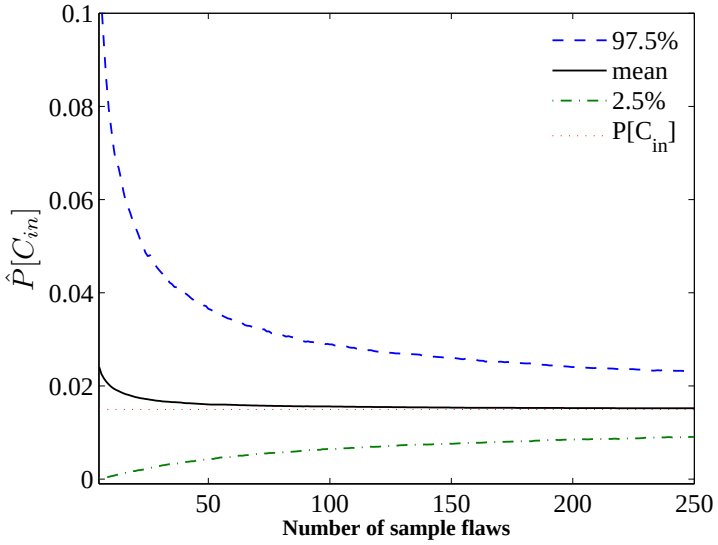

Figure 5.7: Statistical uncertainty in the estimated $\hat{\mathrm{P}}[C_{in}]$

associated with very small data. To quantify the relative uncertainty, the standard error associated with the simulated probability with small sample data is computed and plotted in figure 5.8. The standard error is defined as the standard deviation of the estimated probability of DHC initiation

$$\sigma_{\mathrm{P}[C_{in}]} = \frac{1}{k-1}\sum_{i=1}^{k}\left(\hat{\mathrm{P}}[C_{in}]_k - \mathrm{P}[C_{in}]\right)^2 \tag{5.17}$$

It can be inferred from figure 5.7 and 5.8 that with small number of sample flaws there is significant uncertainty associated with the computed probability of DHC initiation. The uncertainty or the standard error decreases rapidly up to around 60 number of sample flaws. At 60 sample flaws the standard error is approximately 10^{-2}. After that the standard error decreases comparatively slowly. This trend can be observed in both the plots figure 5.7 and figure 5.8. At around 180 number of

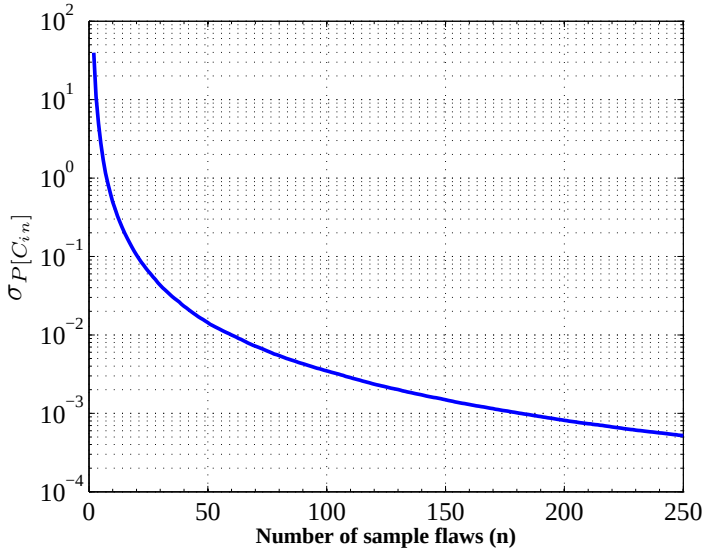

Figure 5.8: Standard error in the estimated $\hat{\mathrm{P}}[C_{in}]$

sample flaws, the standard error is very small ($< 10^{-3}$). If we assume a typical value of 10 flaws per pressure tube, then approximately 6 and 18 PTs are required to inspect for flaws, corresponding to standard errors 10^{-2} and 10^{-3}, respectively.

Moreover, the standard error as estimated above provides us the scope of defining the confidence interval on the true probability. Assuming the estimated $\hat{\mathrm{P}}[C_{in}]$ follows normal distribution with standard deviation $\sigma_{\mathrm{P}[C_{in}]}$, the $(1-\alpha)\%$ CI about the true probability $\mathrm{P}[C_{in}]$ can be stated as

$$\hat{\mathrm{P}}[C_{in}] - u_{\alpha/2}\,\frac{\sigma_{\mathrm{P}[C_{in}]}}{\sqrt{n}} \;\leq\; \mathrm{P}[C_{in}] \;\leq\; \hat{\mathrm{P}}[C_{in}] + u_{\alpha/2}\,\frac{\sigma_{\mathrm{P}[C_{in}]}}{\sqrt{n}} \tag{5.18}$$

For example, if we choose the acceptable standard error in the estimation of probability of DHC initiation as $\sigma_{\mathrm{P}[C_{in}]} = 10^{-2}$, then we need at least 60 observations. Suppose, the 60 sample flaw observation data yield the probability of DHC

initiation as $\hat{\mathrm{P}}[C_{in}] = 2.0189 \times 10^{-2}$. The 95% confidence interval on the true probability is then established as

$$0 \leq \mathrm{P}[C_{in}] \leq 4.5492 \times 10^{-2} \tag{5.19}$$

5.5 Conclusions

This chapter presents a risk informed strategy to determine the required flaw sample size during a scheduled in-service inspections. The sampling uncertainty associated with the probability computation is discussed and a two step confirmatory and explanatory approach is proposed to decide on the sample size requirement. The proposed approach is illustrated through an example of DHC initiation assessment. However this approach can be applied to any other probabilistic assessment.

The main purpose of probabilistic reactor core assessment, is to assess the uninspected reactor based on the test data gathered from the inspected reactor. In the confirmatory phase, the new inspected flaw samples are tested for the deviation of its mean parameters from the referenced mean parameters of the inspected core. The number of sample sizes are determined such that the statistical hypothesis test can be performed with a specified confidence level. Considering the hypothesized mean and the alternative mean differ by 10%, and assuming the significance level at 10% and power of the test at 90%, the approximate number of flaws required to perform the mean hypothesis test are 80, 140 and 210 corresponding to the coefficient variation of the variable 0.3, 0.4 and 0.5, respectively.

If there is not much deviation, the probability value computed using the statistical models derived from the inspected core remains valid for the newly inspected core. Otherwise we follow the second stage of the approach i.e. explanatory data

analysis. In the explanatory phase, the relative uncertainty associated with the probability computation is investigated by simulating the flaws from the reference population. Assuming a certain amount of acceptable standard error in the estimation of probability the required sample size can be defined. The uncertainty or the standard error decreases rapidly up to around 50 number of sample flaws. At 50 sample flaws the standard error is approximately 10^{-2}. After that the standard error decreases comparatively slowly. At 200 number of sample flaws, the standard error is very small ($< 10^{-3}$). The computed relative standard error also provides the scope to define probabilistic bounds on the true probability at specified significance levels.

The number of PTs required to be inspected can be decided using the proposed approach and the reactor specific information about the intensity of number of flaws in a PT.

Chapter 6

Notch and Crack Analysis for Linear Elastic Material

6.1 Introduction

It is well known that any engineering components, e.g. PTs in a nuclear reactor, may contain flaws or crack like defects, introduced during manufacturing process or during the service life. Presence of a flaw in the PT of a CANDU reactor may be critical, since it creates favorable condition for crack growth under DHC mechanism leading to rupture or BBL situation. The condition of rupture of PT normally depends on two parameters, applied stress and maximum allowable stress that the PT can withstand. In order to predict failure of such engineering components with crack like defects, it is necessary to study about the notch/crack induced stress field inside a body. Historically, stress and strain field inside a body have been predicted for two dimensional linear elastic problems, by the use of stress functions. Later, complex stress functions have been employed with the use of conformal mapping

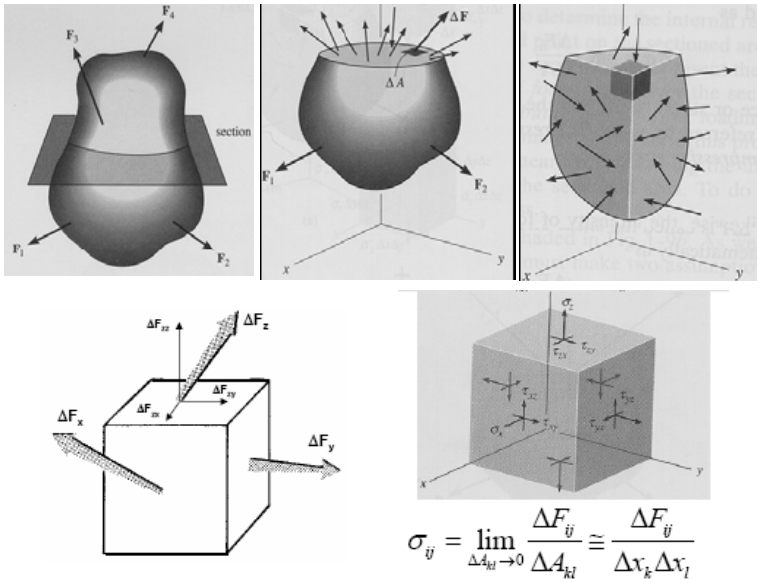

Figure 6.1: Illustration of stress field inside a body

techniques for solving problems involving complicated boundary shapes and crack like defects. In the following sections, fundamental concepts of stress and strain is discussed followed by formulation of notch induced stress field for an centralized crack in a linear elastic infinite body in plane stress condition is described.

6.2 Classical Approach

An external system of forces applied to a three dimensional body in equilibrium results in a non-uniform internal stress field as shown in figure 6.1.

In general, a rectangular three dimensional element will have direct and shear stresses acting on each of it's six surfaces. The nine stress components defining the

state of stress are

$$\begin{pmatrix} \sigma_{xx} & \sigma_{xy} & \sigma_{xz} \\ \sigma_{yx} & \sigma_{yy} & \sigma_{yz} \\ \sigma_{zx} & \sigma_{zy} & \sigma_{zz} \end{pmatrix}$$

The internal stress components must be in equilibrium. This condition leads to a system of six equilibrium equations completely specifying the state of equilibrium. For e.g. equilibrium in x-direction is satisfied by,

$$\frac{\partial \sigma_{xx}}{\partial x} + \frac{\partial \sigma_{xy}}{\partial y} + \frac{\partial \sigma_{xz}}{\partial z} + F_x = 0 \tag{6.1}$$

Where F_x is the body force in $x-$direction. Similar equilibrium equations for $y-$ and $z-$direction can be easily derived.

In addition to stresses the body experience deformation, which is characterized by six strain components. The strains components are of two kinds: direct strain and shear strain. The complete set of equations for direct strain are:

$$\epsilon_{xx} = \frac{\partial u_x}{\partial x}, \quad \epsilon_{yy} = \frac{\partial u_y}{\partial y}, \quad \text{and} \quad \epsilon_{zz} = \frac{\partial u_z}{\partial z} \tag{6.2}$$

where, u_x, u_y, u_z are displacement in $x-$, $y-$ and $z-$directions respectively. The complete set of equations for shear strain are:

$$\epsilon_{xy} = \frac{1}{2}\left(\frac{\partial u_x}{\partial y} + \frac{\partial u_y}{\partial x}\right), \quad \epsilon_{xz} = \frac{1}{2}\left(\frac{\partial u_z}{\partial x} + \frac{\partial u_x}{\partial z}\right) \quad \& \quad \epsilon_{yz} = \frac{1}{2}\left(\frac{\partial u_z}{\partial y} + \frac{\partial u_y}{\partial x}\right) \tag{6.3}$$

6.2.1 Linear Theory of Elasticity

Generalized Hooke's law based on small deformation theory is the foundation for the linear elastic theory.

Small deformation theory

The stress and strain components are defined at a given point. When it is said that a stress component σ is a function of x, y, z, it actually refers to the position of the point in the final (i.e. stressed or deformed) state of the body (Muskhelishvili 1975). However, in small deformation theory, the value of σ at (x, y, z) and (X, Y, Z) is assumed to differ by an amount which is small compared to σ at (X, Y, Z), where (X, Y, Z) is the initial undeformed position of the point and (x, y, z) is the final deformed position. Thus in small deformation theory, the value of σ at a given point (x, y, z) in a deformed body is replaced by the σ value at it's undeformed position (X, Y, Z).

Hooke's law

The deformation of an elastic body is proportional to the forces acting on it i.e. the components of stress at a given point of a body are linear and homogeneous functions of the components of strain at the same point. For a three dimensional isotropic, homogeneous body, the stress and strain components in a linear elastic material is related by Hooke's law as follows

$$\begin{aligned} \epsilon_{xx} &= \frac{1}{E}[\sigma_{xx} - \nu(\sigma_{yy} + \sigma_{zz})] \qquad & \epsilon_{yz} &= \frac{1+\nu}{E}\sigma_{yz} \\ \epsilon_{yy} &= \frac{1}{E}[\sigma_{yy} - \nu(\sigma_{xx} + \sigma_{zz})] \qquad & \epsilon_{zx} &= \frac{1+\nu}{E}\sigma_{zx} \\ \epsilon_{zz} &= \frac{1}{E}[\sigma_{zz} - \nu(\sigma_{xx} + \sigma_{yy})] \qquad & \epsilon_{xy} &= \frac{1+\nu}{E}\sigma_{xy} \end{aligned} \tag{6.4}$$

where E is the modulus of elasticity and ν is poisson's ratio.

The six components of strain are derived from three components of displacement. For continuity the compatibility equations must be satisfied. For example

the compatibility condition for $x-y$ plane in terms of strain components is

$$\frac{\partial^2 \epsilon_{xx}}{\partial y^2} + \frac{\partial^2 \epsilon_{yy}}{\partial x^2} - 2\frac{\partial \epsilon_{xy}}{\partial x \partial y} = 0 \tag{6.5}$$

6.2.2 Plane Theory of Elasticity

The problem of finding stresses and displacements at points within a loaded body is considerably simplified if it can be assumed that there is no change in the distribution of either stress or strain over the $x-y$ plane i.e. in the $z-$direction. The plane theory in which the stress components in the $z-$direction is zero is called plane stress (Love 1927). This state of stress may be assumed to exist in a thin sheet, which is considered incapable of supporting stresses through the thickness. For a plane stress case, all stress components having a $z-$suffix must be zero, yielding: $\sigma_{zz} = \sigma_{zx} = \sigma_{zy} = 0$. This simplifies the stress strain relationship (Eq. 6.4) to

$$\begin{aligned} \epsilon_{xx} &= \frac{1}{E}(\sigma_{xx} - \nu\sigma_{yy}) \\ \epsilon_{yy} &= \frac{1}{E}(\sigma_{yy} - \nu\sigma_{xx}) \\ \epsilon_{xy} &= \frac{1+\nu}{E}\sigma_{xy} \end{aligned} \tag{6.6}$$

Also, the equations of equilibrium simplifies to

$$\frac{\partial \sigma_{xx}}{\partial x} + \frac{\partial \sigma_{xy}}{\partial y} + F_x = 0 \quad \text{and} \quad \frac{\partial \sigma_{yy}}{\partial y} + \frac{\partial \sigma_{xy}}{\partial x} + F_y = 0 \tag{6.7}$$

The strain compatibility relation (Eq. 6.5) can be rewritten in terms of stresses by substituting from the stress-strain relations (Eq. 6.6) as

$$\frac{\partial^2}{\partial y^2}(\sigma_{xx} - \nu\sigma_{yy}) + \frac{\partial^2}{\partial x^2}(\sigma_{yy} - \nu\sigma_{xx}) - 2(1+\nu)\frac{\partial}{\partial x \partial y}(\sigma_{xy}) = 0 \tag{6.8}$$

6.2.3 Stress Function Approach

In plane theory of elasticity there always exist a single auxiliary stress function $\Phi(x, y)$ by the help of which the stress components can be expressed in the following order

$$\sigma_{xx} = \frac{\partial^2 \Phi}{\partial y^2}, \quad \sigma_{yy} = \frac{\partial^2 \Phi}{\partial x^2} \quad \text{and} \quad \sigma_{xy} = -\frac{\partial^2 \Phi}{\partial x \partial y} \tag{6.9}$$

This fact was first noticed by G.B. Airy and the stress function 'Φ' is called Airy function. Since, the stresses are known to be single valued and continuous together with their second order derivatives, a stress function Φ which have continues derivatives up to and including the fourth order and derivatives from the second order onwards having single valued functions throughout the region, will satisfy the equilibrium relations (Eq. 6.7). However, this does not yet mean that these functions corresponds to actual deformation. To ensure this, the stress functions must also satisfy the compatibility condition (Eq. 6.8), which leads to

$$\nabla^2(\sigma_{xx} + \sigma_{yy}) = -(1 + \nu)\left(\frac{\partial}{\partial x}F_x + \frac{\partial}{\partial y}F_y\right) \tag{6.10}$$

and in the absence of body force, this can be written as

$$\left(\frac{\partial^4}{\partial x^4} + 2\frac{\partial^4}{\partial x^2 \partial y^2} + \frac{\partial^4}{\partial y^4}\right)\Phi = \nabla^4 \Phi = 0 \tag{6.11}$$

where ∇^2 is the harmonic operator. Equation 6.11 is bi-harmonic and it's solution is a bi-harmonic function[1]. Therefore, for the complete solution of a plane stress boundary value problem, the stress function must be bi-harmonic and must satisfy all the imposed boundary conditions. This problem is generally solved by assum-

[1]Bi-harmonic functions are functions which satisfy the bi-harmonic equation, the derivatives of which are continuous up to and including the fourth order and the derivatives of which, starting from the second order, are single valued throughout the region under consideration

ing a bi-harmonic stress function and determining the constants of the functions such that it satisfies all the boundary conditions. Numerous Airy stress functions are available in the literature (Timoshenko 1970) with their associated boundary conditions.

Further, using stress function the sum of direct stresses can be expressed as

$$\sigma_{xx} + \sigma_{yy} = \left(\frac{\partial^2}{\partial y^2} + \frac{\partial^2}{\partial x^2} \right) \Phi = \nabla^2 \Phi \tag{6.12}$$

Note that: since Φ must be bi-harmonic, sum of direct stresses given by $\nabla^2\Phi$ must be harmonic. Hence the sum of direct stresses are harmonic functions.

6.2.4 Complex Stress Function

Muskhelishvili (1975) has shown that every bi-harmonic function Φ of the two variables x, y may be represented in a very simple manner by the help of two analytic functions of complex variable $z = x + i\ y$. Complete analysis of complex representation of plane theory of elasticity can be found in the book by Muskhelishvili (1975). Relevant results are presented below.

By denoting these analytic functions by $\phi(z)$ and $\psi(z)$ the following relationship can be established

$$\sigma_{xx} + \sigma_{yy} = 4\ \Re \left[\frac{\partial \Phi(z)}{\partial z} \right] = 2\ \left[\left(\frac{\partial \phi(z)}{\partial z} \right) + \overline{\left(\frac{\partial \phi(z)}{\partial z} \right)} \right] \tag{6.13}$$

$$\sigma_{yy} - \sigma_{xx} + 2\ i\ \sigma_{xy} = 2\ \left[\overline{z}\ \left(\frac{\partial^2 \phi(z)}{\partial z^2} \right) + \overline{\left(\frac{\partial \psi(z)}{\partial z} \right)} \right] \tag{6.14}$$

$$\frac{E}{1+\nu}(u_x + i\ u_y) = \frac{3-\nu}{1+\nu}\phi(z) - z\ \overline{\left(\frac{\partial \phi(z)}{\partial z} \right)} - \overline{\left(\frac{\partial \psi(z)}{\partial z} \right)} \tag{6.15}$$

where, $\overline{(.)}$ = complex conjugate of (.) and $\Re[.]$= Real part of [.].

6.2.5 Elliptical Notch Analysis

The complex representation of plane theory of elasticity in terms of analytic functions lends itself to the application of conformal mapping and provides the analysts with a powerful tool for the solution of cutout and cracks. For e.g. the analytic mapping function

$$z = \omega(\xi) = \frac{a+b}{2}\left[\xi + \left(\frac{a-b}{a+b}\right)\frac{1}{\xi}\right] \tag{6.16}$$

maps the region external to ellipse in the $z-$plane to the region outside a unit circle in the ξ plane, where a and b is the size of elliptical notch along semi-major and semi-minor axis. The choice of circular region for ξ plane is particularly convenient for handling boundary conditions with a power series representation of stress functions. Using conformal mapping, the stress and displacement field can be found through the transformation of variables. Since the crack surface is traction free, a solution in terms of single analytic function defined in ξ plane is required to be chosen. The other analytic function can be directly obtained to satisfy the traction free condition on the crack surface. Following the above argument and suitably choosing the the analytic function $\phi(z)$ in terms of series expansion and satisfying the uniaxial boundary conditions at large $|z| \to \infty$, the tangential stress around the elliptical notch surface is given as

$$\sigma_t = S\ \left(\frac{1-2m-m^2+2\ \cos\theta}{1+m^2-2m\ \cos(2\theta)}\right) \tag{6.17}$$

where S is the uniaxial far field stress perpendicular to the x-axis, θ varies from 0 to 2π. This result leads to infinite stress concentration when the elliptical notch

reduces to a limiting case of sharp crack ($b \rightarrow 0$).

Later, Stevenson (1945) provided the complex potentials for uniaxial loading case using elliptical co-ordinates. However, his complex potential were not suitable for displacement field (Maugis 1992), since the condition of no rotation at infinity is not satisfied. Concerning the displacement field only the exact shape of a crack was studied thoroughly by Theocaris (1986) and Theocaris et al. (1986, 1989).

6.3 Proposed Model

The classical solution to crack problems (section 2.3.1) does not provide any data regarding deformed crack-tip geometry and stress state in the vicinity of the crack-tip due to its singular nature. The classical analysis is based on small deformation theory and lagrangian strain tensor, in which the traction free boundary conditions are satisfied on the un-deformed crack geometry. However, experimental observation indicates blunting of the crack-tip in both elastic and elastic-plastic materials (Theocaris et al. 1989, and Luo et al. 1988). The final shape of the deformed crack geometry given by the exact theoretical solution in an elastic plate (Theocaris 1986 and Theocaris et al. 1989) is an ellipse, whose dimensions depend on the loading and the elastic properties of the plate. Thus an elliptical cavity (Fig. 6.2a) characterized by its initial dimensions a_i and b_i deforms into an ellipse (Fig. 6.2b) with final semi major and semi minor length a_f and b_f respectively.

A complete nonlinear formulation of such a boundary value problem should include large deformations, material nonlinearity, and geometrical nonlinearity. A close form solution to such a problem is, in general, not attainable. However, some researchers have tried to obtain solutions by using only either material nonlinearity (Hutchinson 1968) or only geometrical nonlinearity (Dubey et al. 1992). It has

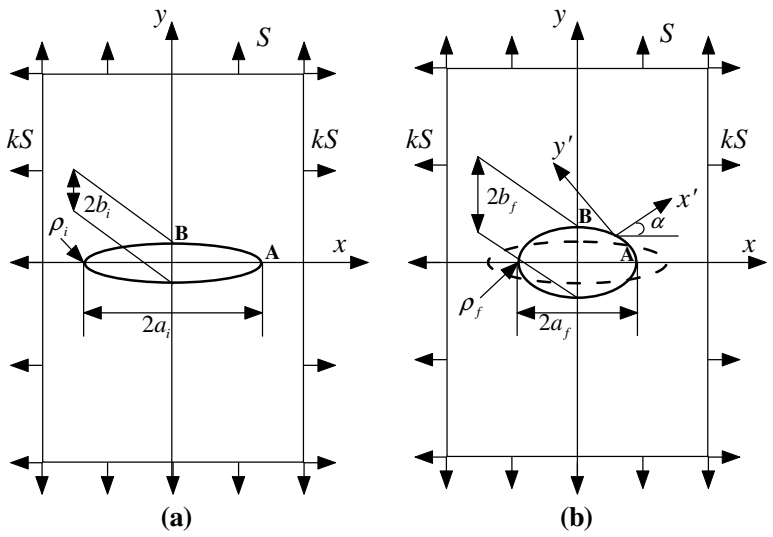

Figure 6.2: Elliptical cavity in an infinite plate: (a) Initial configuration, (b) Final deformed configuration

also been proved (Hutchinson 1968, Rice 1968) that nonlinear material behavior alone does not eliminate the singularity in the stress and strain fields. Therefore, it seems that the singular solution is the result of neglecting the strain-displacement nonlinearity occurring at crack tip due to blunting. The use of large deformation theory needs an appropriate formulation of the boundary value problem associated with the deformed geometry of the body. Unfortunately, the introduction of nonlinear strain-displacement relations significantly complicates the solution procedure. But, it is possible to obtain a nonsingular solution (Singh et al. 1994) even applying the small deformation theory when the boundary conditions are satisfied, not on the initial undeformed boundary, but on the final deformed boundary. The only difference of such a solution, in comparison to classical solution based small deformation theory, is the use of the Cauchy's stress definition and boundary conditions which are coupled with the deformed geometry. This formulation also incorporates

the rotation near the crack-tip leading to blunting and displacement of the crack-tip. However, the choice of complex potential in the problem formulation must be flexible enough to model this rotation near the crack-tip.

In the following sections, proposed solutions to notch and crack problems for linear elastic material subjected to generalized biaxial loading condition are presented. The problem is solved taking into account the changes in geometry due to the applied load. The proposed model allows crack tip blunting and satisfies boundary conditions on the final deformed crack geometry. It is believed that the crack tip stress and strain fields are 3-dimensional in reality. But for mathematical simplicity, the crack tip fields are assumed to be in plane stress condition. The proposed model is expected to provide further insight into the condition assessment of cracked components.

6.3.1 General

Suppose a system of external stresses applied to a plate results in a non-uniform stress field, which is represented by Cauchy or true stress components, σ_{ij}. As a result of the external stress, a particle initially occupying position X_i in the plate is deformed and displaced to a point x_i. Further, if the surface area deforms such that the direction cosines N_i of its initial normal changes to direction cosines n_i in the deformed configuration, the equation of traction on the boundary are

$$t_j = n_i \ \sigma_{ij} \tag{6.18}$$

Note that in Eq. 6.18 the true stress components are associated with the deformed normal, i.e. they are associated with the deformed geometry. It should be noted that, as in classical theory of elasticity, the same linear form of the Eulerian strain

tensor is used in the following analysis. However, the infinitesimal strain assumption is not made here and equilibrium relations, stress-strain relations and strain-displacement relations are strictly considered with respect to deformed coordinates. That is the Lagrangian and Eulerian small-strain tensors are not assumed to be identical. Moreover, the same Muskhelishvili relationship (Eq. 6.13-6.15) in terms of analytic functions are employed. However, in order to get a complete solution, these relations must also satisfy all the applied boundary conditions. To incorporate the boundary conditions in a closed form, let us introduce elliptical coordinates.

6.3.2 Elliptical Co-ordinate System

A transformation from the cartesian to elliptical co-ordinates in terms of a complex variable, $z\ (= x + i\ y)$, is given by, $z = c\ \cosh\zeta$, where $c = \sqrt{a^2 - b^2}$, a is the semi-major length and b is the semi-minor length of the ellipse and $\zeta\ (= \xi + i\ \eta)$ is another complex variable defined in elliptical co-ordinates ξ and η. The cartesian co-ordinates of the crack surface are related to elliptical co-ordinates as follows:

$$x = c\ \cosh\xi\cos\eta \quad \text{and} \quad y = c\ \sinh\xi\sin\eta \tag{6.19}$$

Note that the $x-$axis is defined by $\xi = 0$ for $|x| < c$ and by $\eta = 0$ for $|x| > c$. Eliminating η and ξ from Eq. 6.19 gives, respectively

$$\frac{x^2}{c^2\cosh\xi^2} + \frac{y^2}{c^2\sinh\xi^2} = 1 \tag{6.20}$$

$$\frac{x^2}{c^2\cos\eta^2} - \frac{y^2}{c^2\sin\eta^2} = 1 \tag{6.21}$$

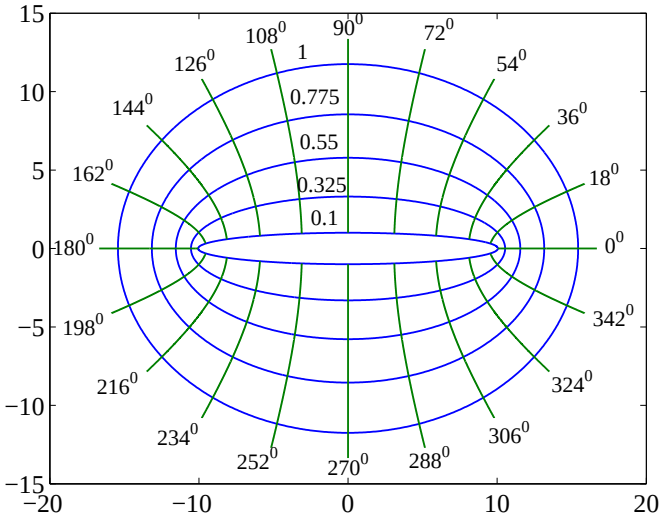

Figure 6.3: Elliptical Co-ordinate system

Constant values ξ and η describe, respectively, homofocal ellipse or hyperbolas as shown in figure 6.3. An elliptical cavity is defined by a constant crack opening parameter $\xi = \xi_o$ such that $a = c \cosh \xi_o$ and $b = c \sinh \xi_o$, and η varies from 0 to 2π.

The Muskhelishvili stress field relations can be expressed in elliptical coordinates using transformation principle as follows

$$\sigma_{\xi\xi} + \sigma_{\eta\eta} = 4 \Re \left[\frac{\partial \Phi(z)}{\partial z} \right] \tag{6.22}$$

$$\sigma_{\eta\eta} - \sigma_{\xi\xi} + 2\, i\, \sigma_{\xi\eta} = 2\, e^{2i\alpha} \left[\overline{z} \left(\frac{\partial^2 \phi(z)}{\partial z^2} \right) + \overline{\left(\frac{\partial \psi(z)}{\partial z} \right)} \right] \tag{6.23}$$

where $e^{2i\alpha} = \sinh \zeta / \sinh \overline{\zeta}$. The $\sigma_{\xi\xi}$ and $\sigma_{\eta\eta}$ are stresses perpendicular to the ellipse and hyperbolas, respectively.

6.3.3 Analysis for an Elliptical Cavity

The analysis presented below is for an elliptical cavity in an infinite plate subjected to remote biaxial loading kS and S (Fig. 6.2a). The plate is assumed to be linear elastic, isotropic, and infinite in the X and Y dimensions. The undeformed elliptical cavity is characterized by its initial dimension a_i and b_i which corresponds to the length of semimajor and semiminor axis, respectively. The initial elliptical cavity deforms to its new shape (Fig. 6.2b) due to the external applied stress. In accordance to the findings of Theocaries et al. (1986), the new shape of the deformed elliptical cavity is assumed to be an ellipse. The new shape is characterized by the final dimension a_f and b_f which corresponds to the length of semimajor and semiminor axis, respectively. The plate is assumed to be in a plane stress state.

General Formulation

Consider an infinite plate with an centralized elliptical cavity denoted by it's semimajor and semiminor length a and b, respectively. The plate is subjected to far field biaxial stresses denoted by kS and S along X and Y directions, respectively. Let us denote the elliptical cavity be represented in elliptical co-ordinate system as ξ_o such that $\tanh \xi_o = b/a$. To get a solution that satisfies all the stress boundary conditions and the condition of no rotation at infinity, let us choose the complex potentials in terms of elliptical co-ordinates (Maugis 1992) as

$$4\phi(z) = c\ S\left[(m + ne^{2\xi_o})\sinh\zeta - ne^{2\xi_o}\cosh\zeta\right] \tag{6.24}$$

$$4\psi(z) = -\frac{c\ S}{\sinh\zeta}\left[m\cosh 2\xi_o + n + ne^{2\xi_o}\sinh\left(2\zeta - 2\xi_o - i\pi\right)\right] \tag{6.25}$$

where $m = 1 + k$ and $n = 1 - k$.

The chosen complex potential and Muskhelishvili relationship gives

$$\frac{2\sigma_{\eta\eta}}{S} = [1 + \lambda(\cosh 2\xi_o - \cos 2\eta)](\lambda C\sinh 2\xi + D) - \lambda[\cosh(2\xi - 2\xi_o) - 1]D\cos 2\eta \tag{6.26}$$

$$\frac{2\sigma_{\xi\xi}}{S} = [1 - \lambda(\cosh 2\xi_o - \cos 2\eta)](\lambda C\sinh 2\xi + D) + \lambda[\cosh(2\xi - 2\xi_o) - 1]D\cos 2\eta \tag{6.27}$$

$$\frac{2\sigma_{\xi\eta}}{S} = \lambda^2(\cosh 2\xi - \cosh 2\xi_o)C\sin 2\eta - \lambda D\sin 2\eta\sinh(2\xi - 2\xi_o) \tag{6.28}$$

$$u_x = \frac{c\ S}{E}[C\sinh\xi\cos\eta + D\cosh\xi\cos\eta - (1+\nu)\sinh(\xi - \xi_o)\sinh\xi_o D\cos\eta - \frac{1+\nu}{2}(\cosh 2\xi - \cosh 2\xi_o)C\sinh\xi\cos\eta] \tag{6.29}$$

$$u_y = \frac{c\ S}{E}[C\cosh\xi\sin\eta + D\sinh\xi\sin\eta - (1+\nu)\sinh(\xi - \xi_o)\cosh\xi_o D\sin\eta - \frac{1+\nu}{2}(\cosh 2\xi - \cosh 2\xi_o)C\cosh\xi\sin\eta] \tag{6.30}$$

where,

$$\lambda = \frac{1}{\cosh 2\xi - \cos 2\eta} \tag{6.31}$$

$$C = m + ne^{2\xi_o} \tag{6.32}$$

$$D = -ne^{2\xi_o} \tag{6.33}$$

One can easily verify the traction free boundary conditions on the cavity. On the cavity ($\xi = \xi_o$). Substituting $\xi = \xi_o$ in to Eq. 6.27 and 6.28 gives $\sigma_{\xi\xi}$ =0 and $\sigma_{\xi\eta}$ = 0. Thus, the traction free condition on the cavity is satisfied.

Stresses and Displacements Around an Elliptical Cavity

Suppose an elliptical cavity characterized by its initial dimension a_i and b_i, deforms to a new elliptical shape due to the external applied stress. The new elliptical shape of the cavity is characterized by the final dimension a_f and b_f which corresponds to the length of semimajor and semiminor axis, respectively. In elliptical coordinates, the undeformed elliptical cavity is denoted as ξ_i and the final deformed elliptical cavity is denoted as ξ_f such that $\tanh \xi_i = b_i/a_i$ and $\tanh \xi_f = b_f/a_f$.

Eqs. 6.26-6.30 make it possible to to calculate stresses and displacements at any point on the plate as a function of final dimensions of the elliptical cavity (ξ_f) and the far field applied stress S. The final dimension of the elliptical cavity (ξ_f) can be established (Sahoo et al. 2007b, Singh et al. 1994) by first computing the displacements of its semimajor (u_x) and semiminor (u_y). The displacement u_x of a_i on the major axis can be computed by setting parameters $c = c_f$, $\xi = \xi_o = \xi_f$ and $\eta = 0$ in Eq. 6.29. Note that $a_f = c_f \cosh \xi_f$ and $b_f = c_f \sinh \xi_f$. Which gives

$$u_x = \frac{S}{E}[2\ k\ b_f - (1-k)a_f] \tag{6.34}$$

Similarly, the displacement u_y of b_i on the minor axis can be computed by setting parameters $c = c_f$, $\xi = \xi_o = \xi_f$ and $\eta = \pi/2$ in Eq. 6.30. Which gives

$$u_y = \frac{S}{E}[2\ a_f + (1-k)b_f] \tag{6.35}$$

The final shape of the elliptical cavity is then given by

$$a_f = a_i + u_x = \frac{a_i\ E(E - S + S\ k) + b_i(2\ E\ S\ k)}{E^2 - S^2(1 + k^2 + 2k)} \tag{6.36}$$

$$b_f = b_i + u_y = \frac{a_i\ (2\ E\ S) + b_i\ E(E + S - S\ k)}{E^2 - S^2(1 + k^2 + 2k)} \tag{6.37}$$

In elliptical coordinate system, the final shape of the elliptical cavity is represented by $\xi_f = \tanh^{-1}(b_f/a_f)$ and the root radius at the tip of the final shape of the cavity on the major axis is

$$\rho_f = \frac{b_f^2}{a_f} \tag{6.38}$$

whereas the root radius of the initial undeformed cavity is given by $\rho_i = b_i^2/a_i$.

The stress field at any point on the plate in terms of final dimensions can be obtained by substituting $\xi_o = \xi_f$ into Eq. 6.26-6.28. Most interesting results are produced below.

Biaxial loading

The final shape of the elliptical cavity under biaxial loading condition is given by Eq. 6.36 and 6.37.

On the x-axis ($\eta = 0$) where $\sigma_{yy} = \sigma_{\eta\eta}$, $\sigma_{xx} = \sigma_{\xi\xi}$ and $\sigma_{xy} = 0$, gives

$$\frac{2\sigma_{yy}}{S} = \left[1 + \frac{\cosh 2\xi_f - 1}{\cosh 2\xi - 1}\right]\left(C\frac{\sinh 2\xi}{\cosh 2\xi - 1} + D\right) - D\frac{[\cosh(2\xi - 2\xi_f) - 1]}{\cosh 2\xi - 1} \tag{6.39}$$

$$\frac{2\sigma_{xx}}{S} = \left[1 - \frac{\cosh 2\xi_f - 1}{\cosh 2\xi - 1}\right]\left(C\frac{\sinh 2\xi}{\cosh 2\xi - 1} + D\right) + D\frac{[\cosh(2\xi - 2\xi_f) - 1]}{\cosh 2\xi - 1} \tag{6.40}$$

On the y-axis ($\eta = \pi/2$) where $\sigma_{yy} = \sigma_{\xi\xi}$, $\sigma_{xx} = \sigma_{\eta\eta}$ and $\sigma_{xy} = 0$, gives

$$\frac{2\sigma_{yy}}{S} = \left[1 - \frac{\cosh 2\xi_f + 1}{\cosh 2\xi + 1}\right]\left(C\frac{\sinh 2\xi}{\cosh 2\xi + 1} + D\right) - D\frac{[\cosh(2\xi - 2\xi_f) - 1]}{\cosh 2\xi + 1} \quad (6.41)$$

$$\frac{2\sigma_{xx}}{S} = \left[1 + \frac{\cosh 2\xi_f + 1}{\cosh 2\xi + 1}\right]\left(C\frac{\sinh 2\xi}{\cosh 2\xi + 1} + D\right) + D\frac{[\cosh(2\xi - 2\xi_f) - 1]}{\cosh 2\xi + 1} \quad (6.42)$$

On the cavity itself ($\xi = \xi_f$), we have $\sigma_{\xi\xi} = \sigma_{\xi\eta} = 0$ and

$$\frac{\sigma_{\eta\eta}}{S} = \frac{\left(m + ne^{2\xi_f}\right)\sinh 2\xi_f}{\cosh 2\xi_f - \cos 2\eta} - ne^{2\xi_f} \quad (6.43)$$

At the tip of the cavity on the major axis ($\eta = 0$), we have

$$\frac{\sigma^A_{\eta\eta}}{S} = \frac{\sigma^A_{yy}}{S} = \left(m + ne^{2\xi_f}\right)\coth \xi_f - ne^{2\xi_f} \quad (6.44)$$

At the tip of the cavity on the minor axis ($\eta = \pi/2$), we have

$$\frac{\sigma^B_{\eta\eta}}{S} = \frac{\sigma^B_{xx}}{S} = \left(m + ne^{2\xi_f}\right)\tanh \xi_f - ne^{2\xi_f} \quad (6.45)$$

Substituting $e^{2\xi_f} = (a_f + b_f)/(a_f - b_f)$ and $\coth \xi_f = a_f/b_f$ into above two equations, gives

$$K^A_t = \frac{\sigma^A_{yy}}{S} = 1 + \frac{2\ a_f}{b_f} - k \quad (6.46)$$

$$K^B_t = \frac{\sigma^B_{xx}}{k\ S} = 1 + \frac{2\ b_f}{a_f} - \frac{1}{k} \quad (6.47)$$

Note that the stress concentration factors, K^A_t, derived using proposed model has the same form as suggested by Maugis (1992). However, in this case, it depends on the final deformed dimension a_f and b_f.

Uniform loading

For uniform loading case $k = 1$, $D = n = 0$ and $C = m = 2$. The final shape of the elliptical cavity under this condition is

$$a_f = a_i \left(\frac{E^2}{E^2 - 4\ S^2} \right) + b_i \left(\frac{2\ S\ E}{E^2 - 4\ S^2} \right) \tag{6.48}$$

$$b_f = a_i \left(\frac{2\ S\ E}{E^2 - 4\ S^2} \right) + b_i \left(\frac{E^2}{E^2 - 4\ S^2} \right) \tag{6.49}$$

In elliptical co-ordinate system the final shape is given by $\xi_f = \tanh^{-1}(b_f/a_f)$, where b_f and a_f is as defined in Eq. 6.48 and 6.49 respectively. The stress field relations (Eq. 6.39-6.47) are simplified under uniform loading condition as follows:

On the x-axis ($\eta = 0$) where $\sigma_{yy} = \sigma_{\eta\eta}$, $\sigma_{xx} = \sigma_{\xi\xi}$ and $\sigma_{xy} = 0$

$$\frac{2\sigma_{yy}}{S} = \left[1 + \frac{\cosh 2\xi_f - 1}{\cosh 2\xi - 1} \right] \left(\frac{2\ \sinh 2\xi}{\cosh 2\xi - 1} \right) \tag{6.50}$$

$$\frac{2\sigma_{xx}}{S} = \left[1 - \frac{\cosh 2\xi_f - 1}{\cosh 2\xi - 1} \right] \left(\frac{2\ \sinh 2\xi}{\cosh 2\xi - 1} \right) \tag{6.51}$$

On the y-axis ($\eta = \pi/2$) where $\sigma_{yy} = \sigma_{\xi\xi}$, $\sigma_{xx} = \sigma_{\eta\eta}$ and $\sigma_{xy} = 0$

$$\frac{2\sigma_{yy}}{S} = \left[1 - \frac{\cosh 2\xi_f + 1}{\cosh 2\xi + 1} \right] \left(\frac{2\ \sinh 2\xi}{\cosh 2\xi + 1} \right) \tag{6.52}$$

$$\frac{2\sigma_{xx}}{S} = \left[1 + \frac{\cosh 2\xi_f + 1}{\cosh 2\xi + 1} \right] \left(\frac{2\ \sinh 2\xi}{\cosh 2\xi + 1} \right) \tag{6.53}$$

On the cavity itself ($\xi = \xi_f$), we have $\sigma_{\xi\xi} = \sigma_{\xi\eta} = 0$ and

$$\frac{\sigma_{\eta\eta}}{S} = \frac{2\ \sinh 2\xi_f}{\cosh 2\xi_f - \cos 2\eta} \tag{6.54}$$

At the tip of the cavity on the major axis ($\eta = 0$), we have

$$\frac{\sigma_{\eta\eta}}{S} = \frac{\sigma^A_{yy}}{S} = 2\ \coth\xi_f \tag{6.55}$$

At the tip of the cavity on the minor axis ($\eta = \pi/2$), we have

$$\frac{\sigma_{\eta\eta}}{S} = \frac{\sigma^B_{xx}}{S} = 2\ \tanh\xi_f \tag{6.56}$$

Substituting $\coth\xi_f = \frac{a_f}{b_f}$ into above two equation, gives

$$K^A_t = \frac{\sigma^A_{yy}}{S} = \frac{2\ a_f}{b_f} \tag{6.57}$$

$$K^B_t = \frac{\sigma^B_{xx}}{S} = \frac{2\ b_f}{a_f} \tag{6.58}$$

Uniaxial loading

For uniaxial loading case $k = 0$ and $m = n = 1$. The final shape of the elliptical cavity under this condition is

$$a_f = a_i \left(\frac{E}{E+S}\right) \tag{6.59}$$

$$b_f = a_i \left(\frac{2\ S\ E}{E^2 - S^2}\right) + b_i \left(\frac{E}{E-S}\right) \tag{6.60}$$

In elliptical co-ordinate system the final shape is given by $\xi_f = \tanh^{-1}(b_f/a_f)$, where b_f and a_f is as defined in Eq. 6.59 and 6.60 respectively. The stress field solutions can be obtained by substituting $m = n = 1$ and the ξ_f for uniaxial loading condition in to Eq. 6.39-6.47.

On the cavity itself ($\xi = \xi_f$), we have $\sigma_{\xi\xi} = \sigma_{\xi\eta} = 0$ and

$$\frac{\sigma_{\eta\eta}}{S} = \frac{\left(1 + e^{2\xi_f}\right) \sinh 2\xi_f}{\cosh 2\xi_f - \cos 2\eta} - e^{2\xi_f} \tag{6.61}$$

At the tip of the cavity on the major axis ($\eta = 0$), we have

$$\frac{\sigma_{\eta\eta}}{S} = \frac{\sigma^A_{yy}}{S} = \left(1 + e^{2\xi_f}\right) \coth \xi_f - e^{2\xi_f} \tag{6.62}$$

Substituting $e^{2\xi_f} = \frac{a_f + b_f}{a_f - b_f}$ and $\coth \xi_f = \frac{a_f}{b_f}$ into Eq. 6.62, gives

$$K^A_t = \frac{\sigma^A_{yy}}{S} = 1 + \frac{2\ a_f}{b_f} \tag{6.63}$$

Similarly, at the tip of the cavity on the minor axis ($\eta = \pi/2$), we have

$$\frac{\sigma^B_{xx}}{S} = \left(1 + e^{2\xi_f}\right) \tanh \xi_f - e^{2\xi_f} = 1 + \frac{2\ b_f}{a_f} \tag{6.64}$$

Note that the concentration factor, K^A_t, derived above using proposed model has the similar form as the well known expression for the stress concentration factor of an elliptical hole under uniaxial loading (Inglis, 1913). However, in this case, it depends on the final deformed dimension a_f and b_f.

It is also interesting to analyze the radius of curvature of the tip of the final elliptical cavity (ρ_f). For biaxial loading condition an explicit relation for ρ_f is hard to obtain. For an uniaxial case, using the Eqs. 6.59 and 6.60, we get

$$\rho_f = \frac{E + S}{E} \left\{ \frac{E}{E - S} \left(\sqrt{\rho_i} + \frac{2S\sqrt{a_i}}{E + S} \right) \right\}^2 \tag{6.65}$$

In general, the range of applied stresses, S, encountered in practice is relatively

very small compared to E, i.e. $S \ll E$. Therefore, Eq. 6.65 can be approximated as

$$\rho_f \cong \left(\sqrt{\rho_i} + \frac{2S\sqrt{a_i}}{E} \right)^2 \tag{6.66}$$

Eq. 6.66 can also be written in terms of Mode-I stress intensity factor given by $K_I = S\sqrt{\pi a}$, as follows

$$\sqrt{\rho_f} - \sqrt{\rho_i} \cong \frac{2K_I}{\pi E} \tag{6.67}$$

It is known that in the case of crack like sharp cavities $\rho_i/a_i \ll 1$. In this case the critical crack tip radius, ρ_c, at the onset of unstable crack propagation can also be estimated in terms of critical stress intensity factor, K_c, as follows

$$\sqrt{\rho_c} - \sqrt{\rho_i} \cong \frac{2K_c}{\pi E} \tag{6.68}$$

It is interesting to note that the final dimension of the cavity given by Eq. 6.36 and 6.37, depends on the far field stresses (S and k) and the elastic property of the material (E). This is in agreement with the findings of Theocaris (1986) and Theocaris et al. (1989).

Many researchers have shown that (Schijve, 1980, Santhanam et al., 1979, Glinka, 1985, Creager et al., 1967), for infinite bodies, the near tip stress fields are function of notch-tip root radius. For example: Glinka (1985) showed for $Y = 0$

$$\sigma_{yy} = \frac{K_t\ S}{2\sqrt{2}} \left[\left(\frac{x}{\rho_i} + \frac{1}{2} \right)^{-1/2} + \frac{1}{2} \left(\frac{x}{\rho_i} + \frac{1}{2} \right)^{-3/2} \right] \tag{6.69}$$

Creager and Paris (1967) showed

$$\sigma_{yy} = \frac{K_I}{\sqrt{2\pi r}} \cos\frac{\theta}{2} \left[1 + \sin\frac{\theta}{2} \sin\frac{3\theta}{2} \right] + \frac{K_I}{\sqrt{2\pi r}} \frac{\rho_i}{2r} \cos\frac{3\theta}{2} \tag{6.70}$$

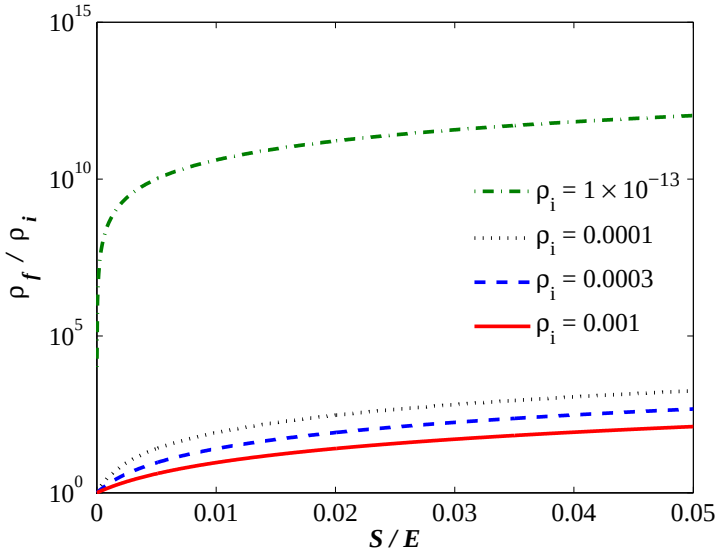

Figure 6.4: Change in notch-tip root radius for uniaxial loading condition ($k = 0$) as a function of applied far field stress S

However, these relations are in terms of initial undeformed notch-tip root radius (ρ_i). Eq. 6.38 makes it possible to analyze the change in the notch-tip root radius, during loading process, as a function of applied load ($S,\ k$) and E, by substituting the corresponding values of final dimensions a_f and b_f. For example Eq. 6.65 defines the final notch-tip root radius for an uniaxial loading condition as a function of S and E. For uniaxial loading condition ($k = 0$), the change of notch-tip root radius with the applied far field stress S for various initial notch geometries is shown in Fig. 6.4. It is apparent (Fig. 6.4) that for sharp notches ($\rho_i \cong 0$), the change in notch-tip curvature, during loading, is significant ($\rho_f \gg \rho_i$). This indicates that the small deformation assumption is violated as the curvature of an elliptical cavity approaches to a sharp crack. Thus, for sharp notches and cracks, the stress field relations formulated in terms of final notch-tip geometry considering the blunting during loading is recommended. For blunt cavities, the change in notch-tip root

radius is comparatively small. Therefore, for blunt notches, the classical solution based on the fixed initial boundaries seems to be sufficient for engineering practices.

6.3.4 Limit Solution for a Sharp Crack ($b_i = 0$)

The relations derived above for an elliptical cavity can also be used to calculate stresses and displacements for the limiting case of a sharp crack with semi-major dimension a_i and semi-minor dimension $b_i = 0$.

Biaxial loading

The final elliptical shape of a sharp crack can be obtained using the Eq. 6.36 and 6.37 by substituting $b_i = 0$, which gives

$$a_f = a_i \frac{E(E - S + S\ k)}{E^2 - S^2(1 + k^2 + 2k)} \tag{6.71}$$

$$b_f = \frac{a_i(2\ E\ S)}{E^2 - S^2(1 + k^2 + 2k)} \tag{6.72}$$

In elliptical co-ordinates the final shape is

$$\xi_f = \tanh^{-1}\left(\frac{b_f}{a_f}\right) = \tanh^{-1}\left(\frac{2\ S}{E - S + S\ k}\right) \tag{6.73}$$

The stress field can be obtained by substituting ξ_f from Eq. 6.73 in to Eq. 6.39-6.45. The stress concentration factor at the tip A of the crack can be obtained by substituting final dimensions in to Eq. 6.46, which gives

$$K_t^A = \frac{\sigma_{yy}^A}{S} = 1 + \frac{E - S + S\ k}{S} - k \tag{6.74}$$

Similarly,

$$K_t^B = \frac{\sigma_{xx}^B}{k\ S} = 1 + \frac{S}{E - S + S\ k} - \frac{1}{k} \tag{6.75}$$

Using Eq. 6.71 and 6.72 the radius of curvature of the tip is

$$\rho_f = a_i \frac{4ES^2}{(E - S + S\ k)[E^2 - S^2(1 + k^2 + 2k)]} \tag{6.76}$$

Uniform loading

The final elliptical shape of a sharp crack under uniform loading ($k = 1$) can be obtained using the Eqs. 6.48 and 6.49 by substituting $b_i = 0$, which gives

$$a_f = a_i \left(\frac{E^2}{E^2 - 4\ S^2} \right) \tag{6.77}$$

$$b_f = a_i \left(\frac{2\ S\ E}{E^2 - 4\ S^2} \right) \tag{6.78}$$

In elliptical co-ordinates the final shape is

$$\xi_f = \tanh^{-1} \left(\frac{b_f}{a_f} \right) = \tanh^{-1} \left(\frac{2\ S}{E} \right) \tag{6.79}$$

The stress field can be obtained by substituting ξ_f from Eq. 6.79 in to Eq. 6.39-6.45. The stress concentration factor at the tip A of the crack can be obtained by substituting the final dimensions in to Eq. 6.57, which gives

$$K_t^A = \frac{\sigma_{yy}^A}{S} = \frac{E}{S} \tag{6.80}$$

Similarly,

$$K_t^B = \frac{\sigma_{xx}^B}{S} = \frac{S}{E} \tag{6.81}$$

Using Eq. 6.77 and Eq. 6.78 the radius of curvature of the tip is

$$\rho_f = 4\ S^2\ a_i \tag{6.82}$$

Uniaxial loading

The final elliptical shape of a sharp crack under uniaxial loading ($k = 0$) can be obtained using the Eq. 6.59 and 6.60 by substituting $b_i = 0$, which gives

$$a_f = a_i \left(\frac{E}{E+S} \right) \tag{6.83}$$

$$b_f = a_i \left(\frac{2\ S\ E}{E^2 - S^2} \right) \tag{6.84}$$

In elliptical co-ordinates the final shape is

$$\xi_f = \tanh^{-1} \left(\frac{b_f}{a_f} \right) = \tanh^{-1} \left(\frac{2\ S}{E-S} \right) \tag{6.85}$$

The stress field can be obtained by substituting ξ_f from Eq. 6.85 in to Eq. 6.39-6.45. The stress concentration factor at the tip A of the crack can be obtained by substituting the final dimensions in to Eq. 6.63, which gives

$$K_t^A = \frac{\sigma_{yy}^A}{S} = \frac{E}{S} \tag{6.86}$$

It is interesting to analyze the radius of curvature of the tip for uniaxial loading condition. Using the Eqs. 6.83 and Eq. 6.84, we get

$$\rho_f = \frac{4ES^2 a_i}{(E+S)(E-S)^2} \tag{6.87}$$

In the case of very low applied stresses such that $S \ll E$, the final crack-tip radius can be approximated in terms of stress intensity factor, K_I as follows

$$\rho_f \cong \frac{4\ K_I^2}{\pi E^2} \tag{6.88}$$

Subsequently, the critical crack tip radius, ρ_c, at the onset of unstable crack propagation can be estimated in terms of material constant,E, and the critical stress intensity factor, K_c, as follows

$$\rho_c \cong \frac{4\ K_c^2}{\pi E^2} \tag{6.89}$$

From the above relationship, it can be observed that the final deformed shape of a sharp crack is function of initial dimensions, applied stress and modulus of elasticity, similar to the case of elliptical cavity.

6.4 Results and Discussion

6.4.1 Stresses Near Elliptical Notches

The stress concentration factor K_t at the tip of the cavity is not constant, but depends on the applied load. K_t^A depends mostly on the far field load S and weekly on the biaxial load factor k. K_t^B depends on far field load S and the biaxial load factor k. For illustration, the variation of K_t^A under uniaxial loading condition ($k = 0$) and applied stress S, determined for several initial notch geometries, is shown in figure 6.5. It is apparent that K_t^A decreases rapidly with increase of applied load S. The rapid decrease of K_t^A occurs immediately after the load is applied when the most significant changes in the notch-tip geometry takes place. The decrease of K_t^A is more significant for sharp notches. For blunt cavities with

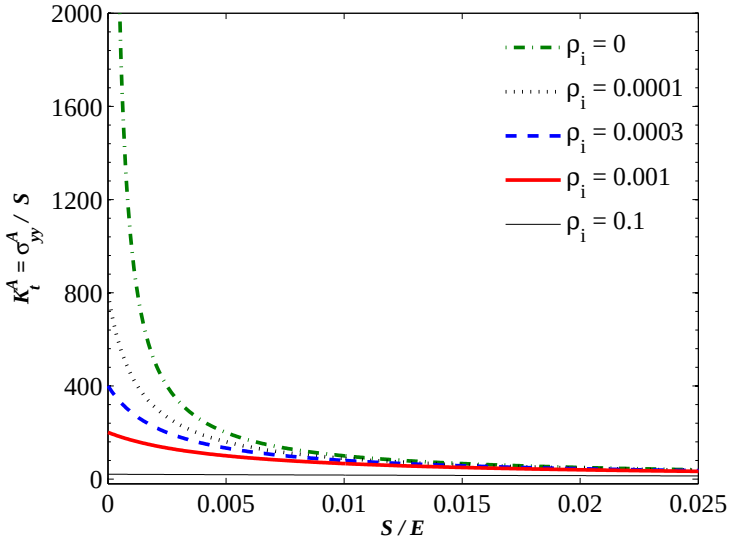

Figure 6.5: Stress concentration factor K_t^A as a function of far field load S and initial geometry under uniaxial loading condition ($k = 0$)

notch-tip radius $\rho_i \geq 0.1$, the change of K_t^A is found to be negligible within the analyzed load range $S \leq 0.025E$. Therefore, for blunt notches with $\rho_i \geq 0.1$, the classical solution based on fixed geometries seems to be sufficient for engineering practices.

Also for illustration, the variation of K_t^B under uniform loading condition ($k = 1$) with applied stresses S, determined for several initial notch geometries, is shown in figure 6.6. It is apparent that K_t^B increases linearly with increase of applied load S. The rapid increase of K_t^B occurs immediately after the load is applied when the most significant changes in the notch geometry takes place.

The stress σ_{yy}^A at the tip of the cavity on major axis can also be computed as

$$\frac{\sigma_{yy}^A}{E} = \frac{SK_t^A}{E} \tag{6.90}$$

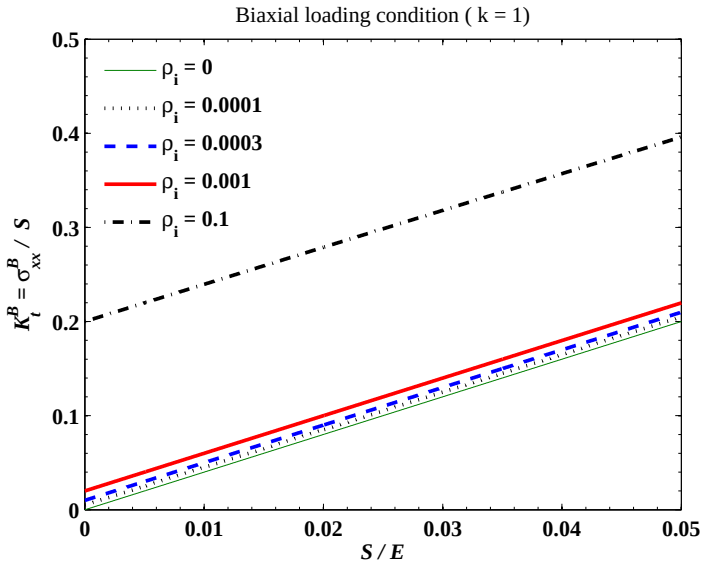

Figure 6.6: K_t^B as a function of far field load S and initial geometry under uniform loading condition ($k = 1$)

The variation of σ_{yy}^A under uniaxial loading condition with applied stress S are shown for several initial notch geometries in figure 6.7. As shown in figure 6.7, in the case of crack or sharp notch, with $\rho_i = 0$, the stress σ_{yy}^A remains constant and equal to the modulus of elasticity E, as soon as the far field load is applied. For notches with $\rho_i > 0$, the notch-tip stress σ_{yy}^A increases almost linearly for small values of applied load S and then gradually departs from linearity as the applied load increases further. The departure occurs early for sharp notches and remains almost linear for a blunt cavity with $\rho_i \geq 0.1$ for the load range $S \leq 0.05\ E$. Therefore, for blunt cavities the classical solution is sufficient. For sharp cavities, the point of departure from linearity (Fig. 6.7) indicates the load range within which the classical solution can be used.

The variation of σ_{xx}^B under uniform loading condition ($k = 1$) with applied stress S are shown for several initial notch geometries in figure 6.8. As shown in figure 6.8,

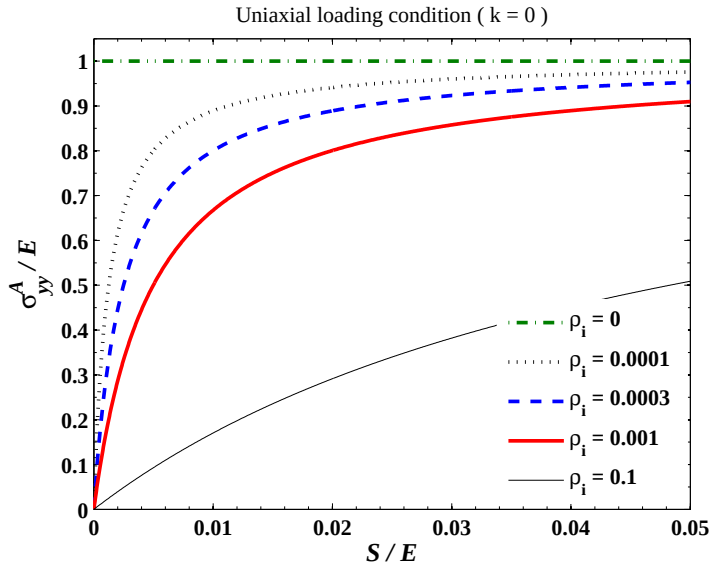

Figure 6.7: Stress σ^A_{yy} at the notch-tip A as a function of far field load S and initial geometry under uniaxial loading condition ($k = 0$)

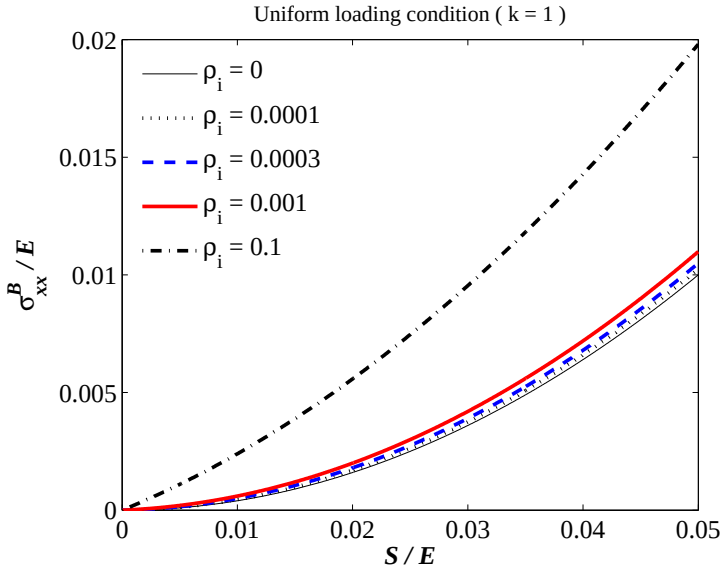

Figure 6.8: Stress σ^B_{xx} at the notch-tip B as a function of far field load S and initial geometry under uniaxial loading condition ($k = 1$)

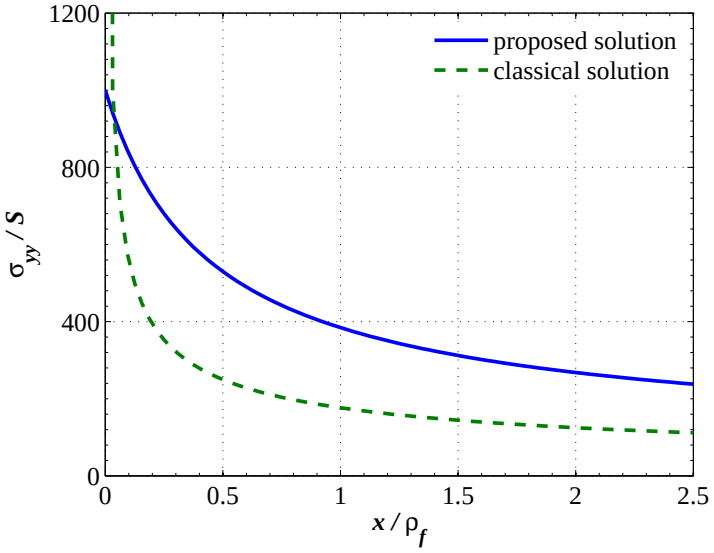

Figure 6.9: Stress component σ_{yy} ahead of the notch-tip along x-axis ($y = 0$) under uniaxial loading condition ($k = 0$)

for all notch configuration, the notch-tip stress σ^B_{xx} increases with applied load S.

6.4.2 Stresses Near Sharp Cracks

The crack-tip blunting takes place during the loading process, affects the stress field distribution in the vicinity of the crack-tip. Typical stress distribution near the deformed crack surface in the plane $y = 0$ under uniaxial loading ($k = 0$), computed from Eq. 6.39 and 6.40, by substituting ξ_f from Eq. 6.85, are shown in figure 6.9 and figure 6.10, respectively. For comparison, the classical singular solution based on fixed geometry is also shown. It is apparent from the figure that the distribution of both the stress components σ_{yy} and σ_{xx} are completely different from the classical solution. The stress component σ_{xx} tends to zero at the blunted crack-tip A, while classical solution tends to infinity. In the case of stress

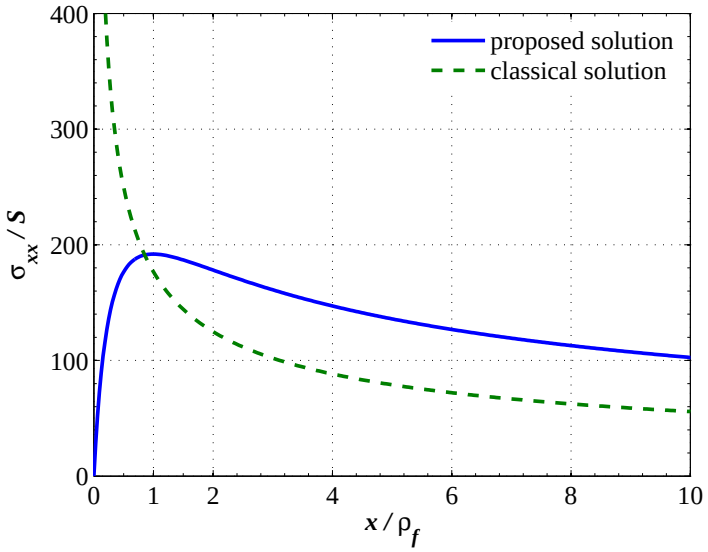

Figure 6.10: Stress component σ_{xx} ahead of the notch-tip along x-axis ($y = 0$) under uniaxial loading condition ($k = 0$)

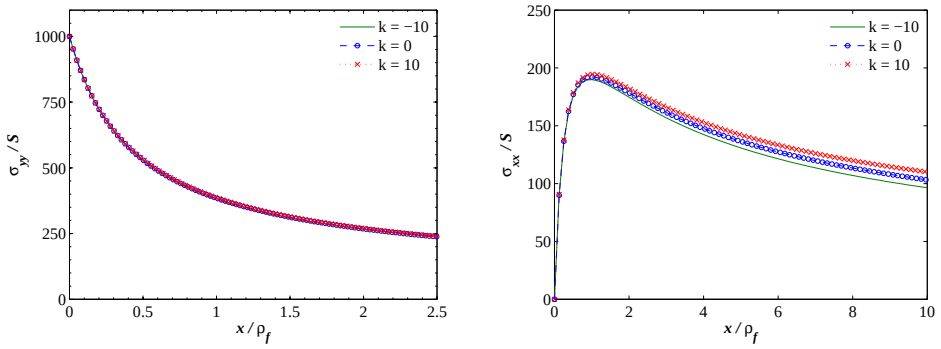

Figure 6.11: σ_{yy} and σ_{xx} ahead of the notch-tip along x-axis ($y = 0$) under biaxial loading condition

component σ_{yy}, the most significant differences between the proposed and classical solution occurs near the crack-tip A. At the tip, the classical solution tends to infinity, while proposed solution yields finite stress $\sigma_{yy} = E$. For distances greater than ρ_f from the crack-tip, both the solution gives qualitatively similar results. The strain at the tip A also reaches finite ($\epsilon_y = 1$) but high value. This indicates that the small deformation assumption is violated. The high strain at the tip results from the 90^0 rotation of crack lips, which takes place during crack-tip blunting process immediately after the far field load is applied.

Also for illustration, the stress field along x-axis is computed under biaxial loading condition with different k values and is shown in figure 6.11. It is apparent from the figure 6.11, that the stress component σ_{yy} is not influenced by the k parameter for the chosen range of k. The stress component σ_{xx} is slightly varies with the analyzed range of k. However, near the notch-tip the difference is negligible.

6.5 Conclusions

In this chapter the stress field induced by a central notch in an infinite linear elastic plate subjected to generalized biaxial loading condition is studied by using a solution associated with the final deformed shape of the notch. The only difference of such a solution, in comparison to classical solution based small deformation theory, is the use of the Cauchy's stress definition and boundary conditions which are coupled with the deformed geometry. This formulation also allows the rotation near the notch-tip leading to blunting and displacement of the tip. The analysis is carried out using linear constitutive law, linear strain-displacement relations and plane stress condition.

The analysis based on the final deformed shape yields non-singular stress field

near the tip of a sharp notch/crack and a non-linear variation of stress concentration factor. Also the notch-tip stresses are found to be dependent on the modulus of elasticity of the material and far field applied stresses.

The analysis revealed that for sharp notches, the change in notch-tip curvature, during loading, is significant. This indicates that the small deformation assumption is violated as the curvature of an elliptical cavity approaches to a sharp crack. Thus, for sharp notches and cracks, the stress field relations formulated in terms of final notch-tip geometry considering the blunting during loading is recommended. For blunt cavities, the change in notch-tip root radius is comparatively small. Therefore, for blunt notches, the classical solution based on the fixed initial boundaries seems to be sufficient for engineering practices.

For the limiting case of a sharp crack subjected to uniaxial loading, the crack tip stresses are found to be finite and constant i.e. $\sigma_{yy}^{A} = E$ and $\sigma_{xx}^{A} = 0$ irrespective of the initial dimension. This suggest that, upon application of small far field load, the notch surface near the tip undergoes a rotation of 90^0 and causing blunting of the tip. This rotation produces finite but high strains at the tip of value equal to one. Increasing the far field load enlarges the the notch-tip root radius, which changes the stress concentration factor in such a way that the stress at the notch-tip remains constant i.e. $\sigma_{yy}^{A} = E$. Also, the critical value of notch-tip curvature is analyzed for instability of the a crack. It is found that, the critical value of notch-tip root radius is a function of critical value of stress intensity factor. Closed form expressions are presented to calculate the stresses and notch-tip curvature.

Chapter 7

Crack Analysis for Elastic-Perfectly-Plastic Material

7.1 Introduction

In real life, most materials experience plastic deformation in the near tip region of a sharp crack, due to high stress concentration exceeding material yield limits. In this plastic region the stress and deformation field is actually controlled by yield property of the material and therefore elastic stress solutions are of limited practical use. The material yield criterion limits the stresses in plastic zone to finite values avoiding the singularity.

Well known analytical crack-tip analysis for strain hardening material are due to Hutchinson (1968) and, Rice and Rosengren (1968), using path independent J integral and deformation plasticity also known as non-linear elasticity. HRR solution (section 2.3.2) describes the structure of singularity near crack-tip region excluding the tip itself. In other words, HRR solution yields singular stress/strain

at the crack-tip for any value of strain hardening exponent of a power law hardening material. Though the HRR model is not applicable when the stress strain relation has a discontinuity (Hutchinson 1968), approximate solutions for an elastic-perfectly-plastic material can still be obtained by using a high strain hardening exponent.

In the derivation of HRR solution, only the second term in the asymptotic expression is considered as relevant. Since the singularity is merely the leading term in the asymptotic expansion, the elastic strains were assumed to be negligible, this solution dominates only valid near the crack tip similar to LEFM solution (Anderson 2005). When the higher order terms are significant, both the HRR model and the classical LEFM model are invalid. Also for very small r values, both the HRR and the classical LEFM solution are invalid because they neglect finite geometry changes at the crack tip (Anderson 2005). The large strains at the crack-tip cause the crack to blunt, which reduces the stress triaxiality locally. The blunted crack-tip is a free surface; thus σ_{xx} must vanish at the blunted crack-tip. The analysis that leads to HRR singularity does not consider the effect of the blunted crack-tip on the stress field.

Wells (1961) is the first person to suggest on the opening of crack surface, when significant plasticity precedes failure. While examining fractured test specimens, Wells noticed that the crack faces has moved apart; plastic deformation has blunted an initially sharp crack. Later on, Wells (1963) proposed the crack tip displacement (CTOD) as a measure of fracture toughness.

McMeeking and Parks (1979) performed crack tip analysis that incorporated large strain theory and finite geometry changes. Figure 7.1 shows some of the analysis results (σ_0 denotes yield stress). Also HRR singularity solution is presented in this plot for comparison. The solid curve in figure 7.1 reaches a peak when the

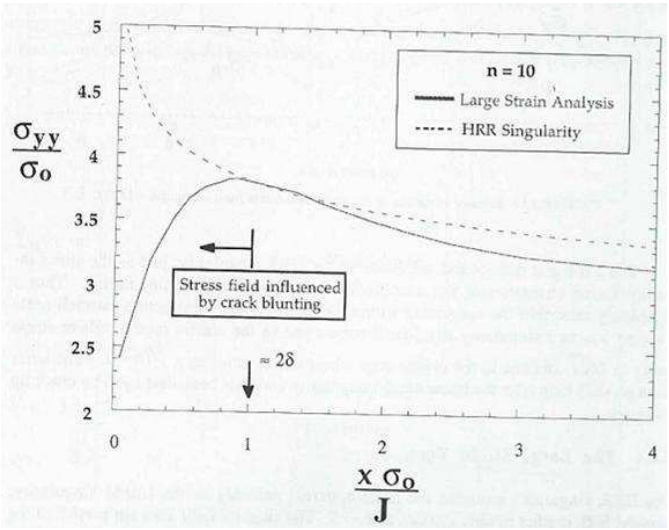

Figure 7.1: Large-strain crack tip finite element results of McMeeking and Parks (McMeeking et al. 1979). Blunting cause the stresses to deviate from the HRR solution at the crack tip

ratio $x\sigma_0/J$ is unity or distance from crack tip reaches twice CTOD, and decreases as $x \to 0$. The HRR singularity is invalid in this region, where the stresses are influenced by large strains and crack blunting.

Other classical models for plastic zone analysis of elastic-perfectly-plastic material, attending the crack-tip were based upon extension of LEFM. These approximate solutions (Anderson, 2005) reconcile singular elastic solution and plastic behavior in a heuristic manner. To obtain the size of plasticity zone on the basis of singular elastic solution, Irwin (Anderson, 2005) assumed constant stress field in the plastic zone (section 2.3.2). The proposal by Dugdale (1968) and Barenblatt (1962) were based on canceling two singularities, one from elastic analysis other associated with the wedge force due to constant yield stress in the plastic zone (section 2.3.2). Both the models postulated that the effect of yielding increases the crack length and leads to blunting at the crack-tip. In Irwin model the postulated crack extends

to the center of the plastic zone and in the Dugdale or Barenblatt model, the crack is assumed to extend right through the plastic zone.

In this chapter better solutions for elastic-perfectly-plastic material is formulated in a fashion similar to Irwin. However, instead of assuming LEFM solution as a reference elastic solution, elastic solution considering the final deformed crack geometry is used. In the proposed analysis the postulation of the increased crack length due to the effect of yielding is avoided. Also the assumption of constant stress value ($\sigma_{xx} = \sigma_{yy} = \sigma_Y$), as suggested in the classical models, in the plasticity zone along crack line is avoided. Instead, the model is constructed flexible enough to compute the actual stress field in the plastic zone using the Von Mises yield criterion. All the results presented here are for a plane stress condition.

7.2 Proposed Model

7.2.1 General

Classical models of plastic zone analysis for elastic-perfectly-plastic material, attending the crack-tip were based upon extension of LEFM solution. The LEFM solution is based on the concept of small deformation theory and assumes the sharp crack remains fixed and sharp during loading, which leads to stress singularity at the crack-tip. The solutions for plastic zone length are derived by reconciling the singular LEFM stress field and plastic zone stress field. The plastic zone stress field along the crack line is assumed to remain constant and equal to the yield stress.

However, as discussed in chapter 6, detail notch and crack analysis for elastic material yields significant deformation and blunting of the tip of a sharp crack. The solution in terms of the final geometry yields finite stress field different in nature

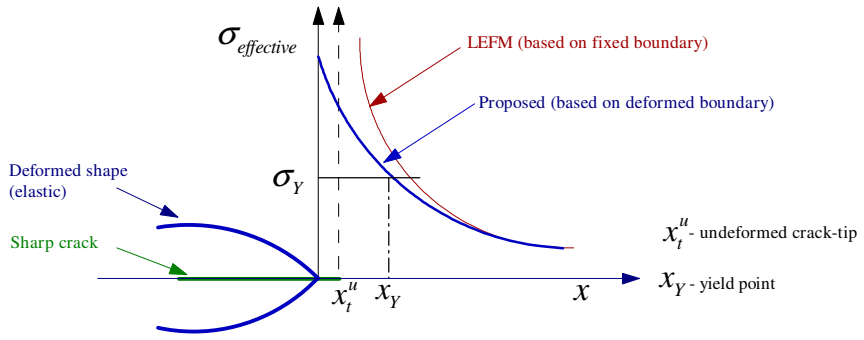

Figure 7.2: Comparison of sigular LEFM solution and solution based on final deformed configuration

and magnitude compared to LEFM results as shown if figure 7.2. Due to blunting effect, the stress σ_{xx} at the tip vanish and the stress σ_{yy} remains finite, where as the LEFM yields $\sigma_{xx} = \sigma_{yy}$ along the crack line. Moreover, the classical models of plastic zone analysis assumes constant stress in the plastic zone equal to yield stress i.e. $\sigma_{xx} = \sigma_{yy} = \sigma_Y$. Since, crack tip is expected to blunt, the assumption of non-zero σ_{xx} at the tip is not valid.

In the following, a better stress field model for elastic-perfectly-plastic material is proposed. The solution is based on reconciling the elastic stress field based on final deformed geometry and the plastic stress field (Sahoo et al. 2006, Sahoo. et al. 2007a), similar to Irwin's model. The crack-tip is assumed to be blunted during the loading process and thus the assumption of constant stress field along the crack line is avoided. In other words, the assumption non-zero σ_{xx} at the tip is not made here. Instead, at the blunted crack-tip the stress σ_{xx} is taken zero and a flexible analytic function is used to define the stress field inside the plastic zone along the crack line. The constants of the analytic function are then estimated to satisfy the stress boundary conditions as well as the stress free condition on the deformed crack surface.

7.2.2 Elastic Stress Field

In chapter 6 complete formulation for elastic stress field based on the final geometry is presented. However, the necessary results for a sharp crack under uniaxial loading condition are reproduced here.

The final elliptical shape of a sharp crack under uniaxial loading is given by

$$a_f = a_i \left(\frac{E}{E+S} \right) \quad \text{and} \quad b_f = a_i \left(\frac{2\ S\ E}{E^2 - S^2} \right) \tag{7.1}$$

In elliptical co-ordinates the final shape is

$$\xi_f = \tanh^{-1} \left(\frac{b_f}{a_f} \right) = \tanh^{-1} \left(\frac{2\ S}{E-S} \right) \tag{7.2}$$

The stress field along the crack line ($y = 0$) in terms of the final shape (ξ_f) is obtained by substituting the constants for uniaxial case in to Eq. 6.39-6.40 and solving as

$$\frac{2\sigma_{yy}}{S} = -e^{2\xi_f} \left[1 + \frac{\sinh(2\xi_f - \xi)}{\sinh \xi} \right] + \left(1 + e^{2\xi_f} \right) \coth \xi \left[1 + \frac{\sinh^2 \xi_f}{\sinh^2 \xi} \right] \tag{7.3}$$

$$\frac{2\sigma_{xx}}{S} = -e^{2\xi_f} \left[1 - \frac{\sinh(2\xi_f - \xi)}{\sinh \xi} \right] + \left(1 + e^{2\xi_f} \right) \coth \xi \left[1 - \frac{\sinh^2 \xi_f}{\sinh^2 \xi} \right] \tag{7.4}$$

The stress concentration factor at the crack-tip is

$$K_t^A = \frac{\sigma_{yy}^A}{S} = \frac{E}{S} \tag{7.5}$$

7.2.3 Plastic Zone Stress Field

In the plastic region the stress field is controlled by yield property of the material. The two most common yield criteria are due to Tresca and Von Mises. We consider Von Mises condition for yielding in the process zone, which is given by

$$\left(\frac{\sigma_{yy}+\sigma_{xx}}{2}\right)^2+3\left\{\left(\frac{\sigma_{yy}-\sigma_{xx}}{2}\right)^2+\sigma_{xy}^2\right\}=\sigma_Y^2 \tag{7.6}$$

where σ_Y is the Yield stress.

For a linear isotropic material, it is known that the stress function Φ must be real and bi-harmonic, and hence the sum of stresses given by $\sigma_{xx}+\sigma_{yy}=\frac{\partial^2\Phi}{\partial z\partial z^*}$ must be real and harmonic (section 6.2.3). This gives solutions of stress and displacement field using analytic functions ϕ and ψ. Suppose a particular choice of analytic function solves a given boundary value problem for an isotropic linear solid. Then analytic functions of same form can also be used to solve the problem of another isotropic linear solid under identical boundary conditions. Though the stress function formulation is commonly used to analyze a two dimensional plane elasticity problem relate to the crack induced stress field (Muskhelishvili 1975), Panayotounakos et al. (1989) has shown that the stress function formulation can be extended to solve the stress field for a rigid perfectly plastic material. In the case of elastic-perfectly-plastic material, the yield stress is constant and the stress strain curve is linear and isotropic in the plastic region. It is then reasonable to assume the sum of stresses $\sigma_{xx}+\sigma_{yy}$ is also analytic in the plastic region and can be expressed in terms of a single analytic function ϕ (Sahoo et al. 2007a, Sahoo et al. 2007b). However, the analytic function ϕ should be chosen such that the stress field it generates in conjunction with the yield criterion leaves the blunted crack surface free of traction.

Now let us choose the sum of stresses as harmonic function in the form of $\sigma_{xx}+\sigma_{yy} = 2\, f(x,y)\, \sigma_Y$, where $f(x,y)$ is an analytic function. Along crack line ($y = 0$), substituting $\sigma_{xy} = 0$ in to Eq. 7.6 and solving gives $\sigma_{yy}-\sigma_{xx} = \frac{2\ \sigma_Y}{\sqrt{3}}\sqrt{1-f(x)^2}$. This yields the stress field along crack line as

$$\sigma_{yy} = \sigma_Y \left(f(x) + \sqrt{\frac{1-f(x)^2}{3}} \right) \quad \text{and} \quad \sigma_{xx} = \sigma_Y \left(f(x) - \sqrt{\frac{1-f(x)^2}{3}} \right) \tag{7.7}$$

Note that classical approximate models for elastic-perfectly-plastic material assumes $f(x) = 1$ along the crack line (Anderson, 2005).

To generalize the solution, we choose a harmonic complex function for $\sigma_{xx}+\sigma_{yy}$ in the form

$$\sigma_{xx} + \sigma_{yy} = \sigma_Y\ \{\sin[p(z-x_0)] + \sin[p(z^*-x_0)]\} \tag{7.8}$$

where p and x_0 are real and unknown constants those would be determined satisfying the imposed boundary conditions. Eq. 7.8 can also be written in terms of cartesian co-ordinates as

$$\sigma_{xx} + \sigma_{yy} = 2\ \sigma_Y\ \ \sin[p(x-x_0)]\ \ \cosh(p\ y) \tag{7.9}$$

Along the crack line, $y = 0$, and thus

$$\sigma_{xx} + \sigma_{yy} = 2\ \sigma_Y\ \ \sin[p(x-x_0)] \tag{7.10}$$

It is apparent that in this proposed formulation the function $f(x)$ is chosen as $\sin[p(x-x_0)]$ and thus avoids the postulation constant value ($f = 1$) as taken in the approximate models (Anderson, 2005) for plastic zone analysis of elastic-perfectly-plastic material. Eq. 7.7 yields the following stress field along the crack

line

$$\sigma_{yy} = \sigma_Y \left\{ \sin[p(x - x_0)] + \frac{1}{\sqrt{3}} \cos[p(x - x_0)] \right\} \tag{7.11}$$

$$\sigma_{xx} = \sigma_Y \left\{ \sin[p(x - x_0)] - \frac{1}{\sqrt{3}} \cos[p(x - x_0)] \right\} \tag{7.12}$$

7.2.4 Elastic-Perfectly-Plastic Stress Field

The solution for an elastic-perfectly-plastic material can be obtained by reconciling elastic stress solution and plastic stress solution and satisfying all the necessary boundary condition. The boundary conditions are:

1. Inside the plastic zone, the effective stress field should equal to the yield stress of the material.

2. At the blunted crack tip the stress $\sigma_{xx} = 0$

3. At the elastic plastic interface along the crack line the solution should satisfy the continuity of the stress fields. In other words, the elastic stress field and plastic zone stress should be an unique value at the elastic plastic interface.

4. Load equilibrium condition should be maintained as explained in the Irwin's model (Anderson, 1995).

Now let us denote the deformed crack tip position and the elastic plastic interface along the crack line (y = 0) as $x = x_t$ and $x = x_Y$ or in elliptical co-ordinate $\xi = \xi_t$ $\xi = \xi_Y$, respectively (Fig. 7.3).

The elastic plastic interface along the crack line is the point where the effective elastic stress equals yield stress of the material. The point of elastic plastic interface

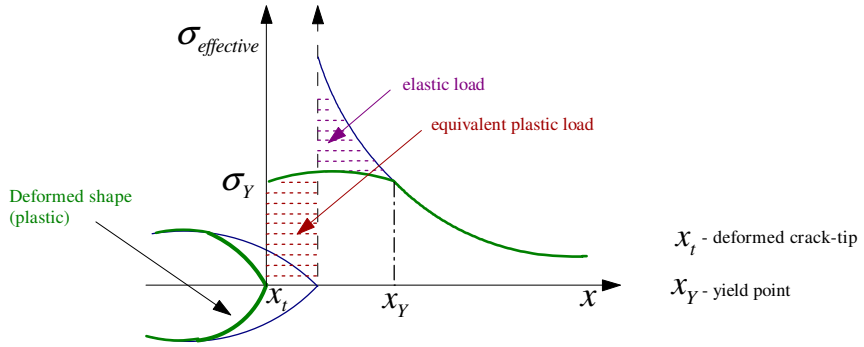

Figure 7.3: plastic zone

along crack line can be found out by solving the for ξ_Y which satisfy the Von Mises yield criterion

$$\sigma_{yy}^2 + \sigma_{xx}^2 - \sigma_{yy}\sigma_{xx} = \sigma_Y^2 \tag{7.13}$$

where σ_{yy} and σ_{xx} is defined by Eq. 7.3 and 7.4, respectively, with ξ replaced by ξ_Y.

To derive the constants p and x_0 and the deformed crack tip position, x_t, the following boundary conditions are used:

1. To reconcile the continuity between the plastic stress field and elastic stress field at the elastic plastic interface (i.e. at $x = x_Y$ and $\xi = \xi_Y$) along crack line, we have

$$\sigma_Y \left\{ \sin[p(x_Y - x_0)] + \frac{1}{\sqrt{3}} \cos[p(x_Y - x_0)] \right\} = C_1 \left[1 + \frac{\sinh(2\xi_f - \xi_Y)}{\sinh \xi_Y} \right] + C_2 \left[1 + \frac{\sinh^2 \xi_f}{\sinh^2 \xi_Y} \right] \coth \xi_Y \tag{7.14}$$

2. At the blunted crack tip, $\sigma_{xx} = 0$, is satisfied when

$$p(x_t - x_0) = \frac{\pi}{6} \tag{7.15}$$

3. The load equilibrium condition, provides the relation that the total load from the elastic solution between final crack length (a_f) and elastic plastic interface (x_Y) should be redistributed between the deformed crack tip (x_t) and elastic plastic interface (x_Y). This leads to

$$\begin{aligned}\sigma_Y \int_{x_t}^{x_Y} \left\{ \sin[p(u - x_0)] + \frac{1}{\sqrt{3}} \cos[p(u - x_0)] \right\} \, du = \\ C_1 \int_{a_f}^{x_Y} \left\{ 1 + \sinh 2\xi_f \frac{u}{\sqrt{u^2 - c^2}} - \cosh 2\xi_f \right\} \, du + \\ C_2 \int_{a_f}^{x_Y} \left\{ \frac{u}{\sqrt{u^2 - c^2}} + \sinh^2 2\xi_f \frac{c^2 \ u}{(u^2 - c^2)^{3/2}} - \cosh 2\xi_f \right\} \, du \end{aligned} \tag{7.16}$$

where $C_1 = \frac{-S}{2} e^{2\xi_f}$, $C_2 = \frac{S}{2}\left(1 + e^{2\xi_f}\right)$ and $c = \sqrt{a_f^2 - b_f^2}$. The above three equations (Eq. 7.14, 7.15 and 7.16) can be solved for three unknown constants p, x_0 and deformed crack tip position x_t. Once the constants are evaluated, the stress field along the crack line in the plastic zone can be obtained by substituting these constants into Eq. 7.11-7.12 and the stress field ahead of the plastic zone i.e. in the elastic region along the crack line can be obtained using Eq. 7.3-7.4. The length of the plastic zone is given as

$$l_p = x_Y - x_t \tag{7.17}$$

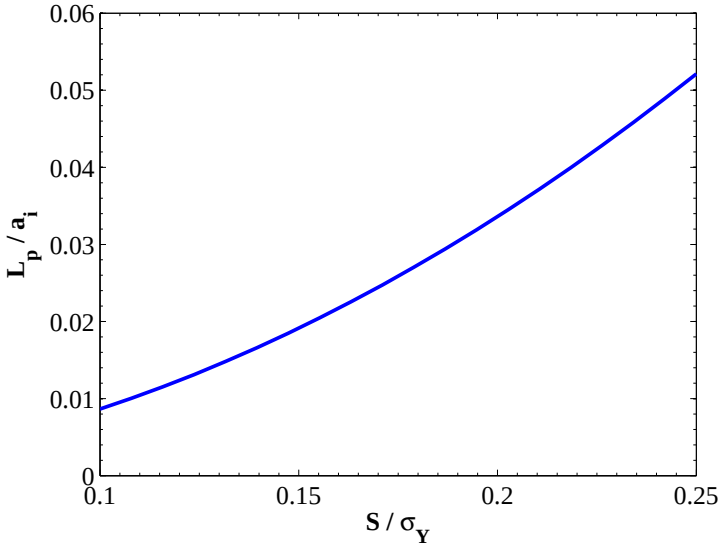

Figure 7.4: Plastic zone size

7.3 Results and Discussions

7.3.1 Plastic Zone Size

The plastic zone size (l_p) is calculated for different values of initial half crack length (a_i), far field stress (S), and yield stress σ_Y. The variation of l_p is plotted in figure 7.4. As shown in figure 7.4, the plastic zone size (l_p), increases almost linearly with the increase in the applied stress (S).

7.3.2 Stress Field in the Plastic Zone

The crack tip blunting, which takes place during loading, also affects the stress distribution in the vicinity of the crack tip. Typical stress components along the crack axis ($y = 0$) are shown in figure 7.5. For comparison, the LEFM based

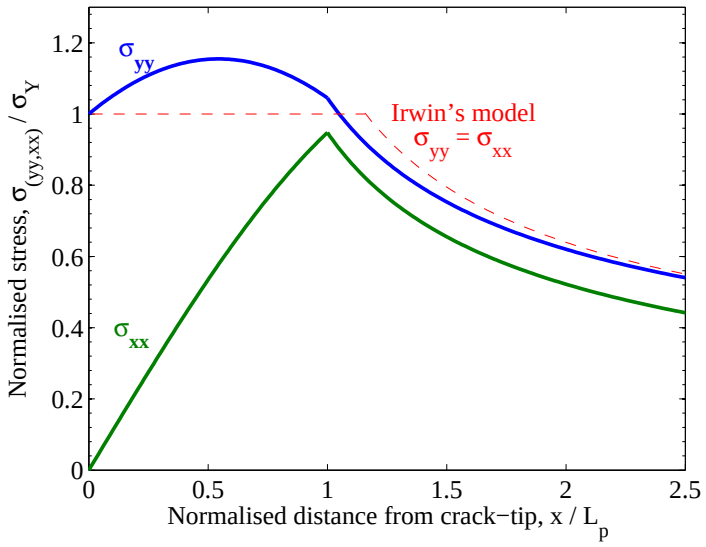

Figure 7.5: Stress distribution ahead of the crack-tip (y = 0)

classical Irwin's solution is also plotted.

It is apparent that the stress distribution is significantly different in nature and magnitude from the classical solutions. In the plastic region, the stress σ_{xx} tends to zero at the crack tip which is obvious for blunted crack tip and increases almost linearly up to the elastic-plastic boundary. The component σ_{yy} is equal to σ_Y at the crack-tip and gradually increases and then decreases. It has a distinct peak at some distance ahead of the crack-tip. Beyond elastic plastic interface stress components follow the elastic stress field solution.

The plastic zone size computed using the proposed model is smaller than the Irwin's result based on the classical LEFM solution. This is obvious, because the LEFM predicts infinite stress as the crack-tip approaches and hence the elastic load to be balance with the plastic load is larger compared to the proposed model.

The stress distribution inside plastic zone depends on the far field stress value

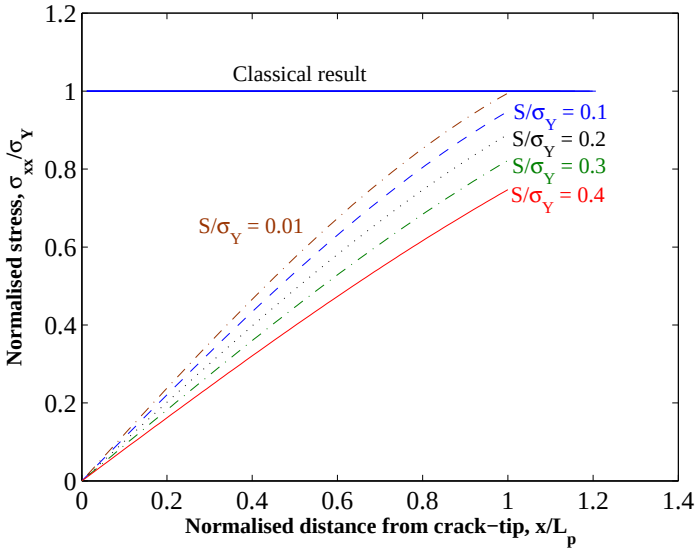

Figure 7.6: Stress component σ_{xx} ahead of the crack-tip (y = 0) inside the plastic zone

S. The stress component σ_{xx} and σ_{yy} inside plastic zone along crack line ($y = 0$) for different far field stress values are plotted in figure 7.6 and figure 7.7, respectively. Inside the plastic zone, σ_{xx} remains smaller than σ_Y (Fig. 7.6) while σ_{yy} remains larger than σ_Y (Fig. 7.7). The plastic zone size computed using the proposed model is smaller than the classical result. The stress component σ_{xx} at the elastic plastic interface is smaller than the yield limit of the material and the difference is prominent for larger far field stress values. Similarly, the stress component σ_{yy} at the elastic plastic interface is lager than the yield limit of the material and the difference is prominent for large far field stress values. However, LEFM based Irwin's model assumes constant stress equal to the yield limit of the material throughout the plastic zone.

For a small applied far field stress value (i.e. $S/\sigma_Y \leq 0.01$), the stress components (σ_{xx} and σ_{yy}) at the elastic plastic interface are almost equal to yield stress

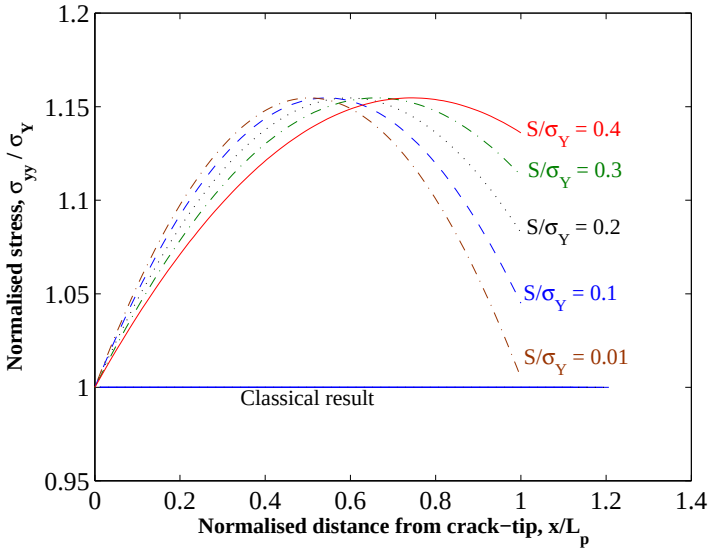

Figure 7.7: Stress component σ_{yy} ahead of the crack-tip (y = 0) inside the plastic zone

of the material. Thus, for small applied stress value, the classical argument that $\sigma_{xx} = \sigma_{yy} = \sigma_Y$ is valid at the elastic plastic interface.

As shown in figure 7.7, the resulting stress concentration factor is non-linear and it is interesting to note that the highest stress concentration is not at the crack-tip, but slightly away from the crack tip. However, the peak stress value is almost constant and depends on the yield stress of the material irrespective of the applied far field stress value.

7.4 Conclusions

This chapter presents a solution to stress and deformation field induced by a central crack in an infinite elastic-perfectly-plastic plate. The problem is solved by recon-

ciling the plastic zone stress field with the elastic stress field similar to classical Irwin's model. However, the effect of blunting and changes in the geometry due to the applied load is considered here. The plastic zone stress field is based on a stress function that satisfies the Von Mises yielding criterion. The elastic stress field is based on the elastically deformed crack geometry resulting from the application of the load. Since, a sharp crack in an elastic material deforms into the shape of an ellipse under applied load, the elastic stress field based on deformed geometry is used.

Analytical model is presented to predict the size of plastic zone and the stress distribution. The plastic zone size computed using the proposed model is smaller than the classical result. The proposed solution yields non-singular stress field at the crack tip and a non-linear variation of stress concentration factor inside the plastic zone. The stress distribution is found to be significantly different in nature and magnitude from the classical solutions. In the plastic region, the stress σ_{xx} tends to zero at the crack tip which is obvious for blunted crack tip and increases almost linearly up to the elastic-plastic boundary. The component σ_{yy} is equal to σ_Y at the crack-tip and gradually increases and then decreases. It has a distinct peak at some distance ahead of the crack-tip. Beyond elastic plastic interface stress components follow the elastic stress field solution. However, LEFM based Irwin's model assumes constant stress equal to the yield limit of the material throughout the plastic zone.

Inside the plastic zone, σ_{xx} remains smaller than σ_Y while σ_{yy} remains larger than σ_Y. The stress component σ_{xx} at the elastic plastic interface is smaller than the yield limit of the material and the difference is prominent for larger far field stress values. Similarly, the stress component σ_{yy} at the elastic plastic interface is lager than the yield limit of the material and the difference is prominent for large

far field stress values. For a small applied far field stress value (i.e. $S/\sigma_Y \leq 0.01$), the stress components (σ_{xx} and σ_{yy}) at the elastic plastic interface are almost equal to yield stress of the material. Thus, for small applied stress value, the classical argument that $\sigma_{xx} = \sigma_{yy} = \sigma_Y$ is valid at the elastic plastic interface.

Though the stress distribution inside plastic zone depends on the far field stress value S, the peak stress value (σ_{yy}^{peak}) is almost constant and depends only on the yield stress of the material.

The proposed approach generalizes the crack-tip plasticity models and presents a basis for condition assessment and reliability evaluations of cracked elements.

Chapter 8

Analytical Estimation of K_{IH}

8.1 Introduction

Zirconium alloy (Zr-2.5%Nb) is widely used in manufacturing PTs of CANDU reactors. The presence of hydrides in Zirconium alloy PTs may lead to a slow crack propagation referred to as DHC (Sawatzky et al. 2000). DHC is a serious form of degradation that can cause rupture of the PT resulting in adverse safety consequences. The subcritical crack growth of hydrided Zirconium alloy PT by DHC is characterized in terms of mode-I stress intensity factor (SIF) K_I, and the DHC growth rate is negligible so long as applied SIF, K_I, is less than a critical threshold value denoted as K_{IH}. This fact has important implications in the risk assessment and life cycle management of the reactor core. For example, if it can be demonstrated that an existing flaw is subjected to $K_I < K_{IH}$, the possibility of DHC initiation of the flaw can be discounted.

Modeling of DHC involves consideration of three distinct phenomena: diffusion, phase transformation and fracture. Diffusion models developed in the past

describes the behavior of cracking process (Satwazky et al. 2000, Coleman et al. 1966). Bahurmuz (1993) developed an empirical model to predict the hydrogen concentration profiles near rolled joints of Zirconium PTs. Satwatzky (1985) developed a mathematical model for estimating the time required for hydride blister formation based on the phenomenon of thermal diffusion of hydrogen in Zirconium. However, these models are not developed to predict the critical condition for crack initiation by DHC.

Based on the results of the experimental studies, the Canadian Standard (CSA N285.8 2005) suggests a lower bound value of $K_{IH} = 4.5$ MPa$\sqrt{m}$. The objective of this paper is to present an analytical model for the evaluation of K_{IH} so that the conservatism associated with a generic model can be minimized.

8.2 Analysis

8.2.1 DHC Initiation Criterion

The DHC process is influenced by the crack-tip stress field and the diffusion of hydrogen atoms to the proximity of the crack-tip. There is evidence to suggest that hydrogen accumulation in the process zone leads to the precipitation of hydride platelets at the peak stress location ahead of the crack-tip. The precipitation of hydrides increase the volume of zirconium alloy by forming the zirconium hydride, which in turn induces a compressive stress, σ^h, in the matrix (Coleman et al. 1966). The externally applied stress (σ_{yy}) and precipitation of hydride create a local stress within the hydride. The local stress in the hydride is assumed to be

linear superposition of these two components (Shi et al. 1994). Thus,

$$\sigma_{local} = \sigma_{yy} + \sigma^h \tag{8.1}$$

The DHC process is initiated (Sagat et al. 1994) when the local stress, σ_{local}, exceeds the fracture strength of the hydride, σ_f^h . The crack growth proceeds through fracturing of a hydride platelet and the cycle repeats at the new crack tip location.

Figure 8.1 shows a schematic of the stress field in the process zone ahead of the crack-tip. In this figure, X-coordinate measures distance from the center of the crack along its axis. Another horizontal coordinate, R-coordinate, is defined in which the distances are measured from the crack-tip. Some key variables are defined as follows: x_t is the distance of the crack-tip from the crack center, x_Y is the distance of the elastic and process zone interface from the crack center, and l_p is the process zone length, which is the distance of elastic and process zone interface from the crack-tip.

The hydride platelet normally covers the full process zone length (Shi et al. 1994) as shown in figure 8.1. Suppose that the peak mechanical stress (σ_{yy}^{peak}) occurs at a distance $r = r_c$ ahead of the crack-tip in the process zone. The location of the peak stress (r_c) becomes the site of DHC initiation (Shi et al. 1994, Kim et al. 2000) under the following condition

$$\sigma_{yy}^{peak} + \sigma^h(r_c) \geq \sigma_f^h \tag{8.2}$$

The threshold stress intensity factor (K_{IH}) is the stress intensity (K_I) associated with $\sigma_{local}(r_c) = \sigma_f^h$.

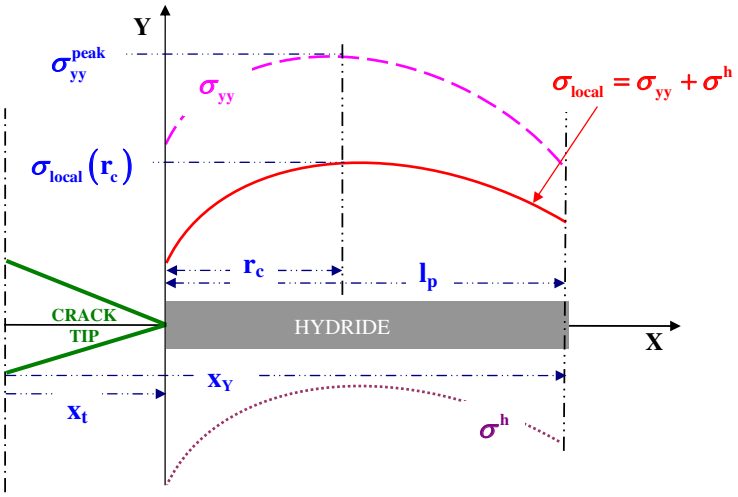

Figure 8.1: Schematic diagram showing crack tip hydride and stresses in the process zone

The determination of the distribution of the mechanical stress ahead of the crack-tip in the process zone is a key component of the analysis. This paper presents a refined analytical solution (section 8.2.2) to obtain the location and the magnitude of the peak stress. The hydride stress as a function of platelet thickness and temperature is obtained in section 8.2.3 using the models reported in the literature (Shi et al. 1994, Kim et al. 2000, Wappling 1997). The fracture strength of hydride is a material property and it can be estimated as shown in the reference (Shi et al. 1994).

8.2.2 Mechanical Stress in the Process Zone

In LEFM based classical Irwin's plastic zone model (Anderson 1995), the mechanical stress is assumed to remain constant and equal to the yield stress along the crack axis in the process zone i.e. $\sigma_{yy} = \sigma_{xx} = \sigma_Y$. Shi and Puls (1994) and Wappling et

al. (1997) assumed similar constant mechanical stress in their model. The critical distance, r_c, was assumed to be equal to twice the crack opening displacement (Shi et al. 1994).

These idealized assumptions are not validated by numerical and experimental studies. Numerical large deformation crack-tip stress analysis (McMeeking 1979) shows blunting of the crack-tip and the resulting mechanical stress is not constant along the crack line, rather it has a distinct peak at some distance ahead of the crack tip. This observation is also confirmed experimentally (Leitch et al. 1992).

In a recent study, Kim et al. (2000) suggested a cohesive zone model for estimation of stress and process zone length. In his model, the maximum stress was estimated assuming a linear increase in stress, and its location was obtained by balancing the load in the process zone. Models for K_{IH} reported in the literature are approximate in nature and sometimes they do not provide a qualitative agreement with the test data (Shi et al. 1994, Kim et al. 2000, Wappling 1997).

In the following, a more refined model is presented for the stress field inside the process zone to determine the peak stress value and its location. The proposed model is formulated by defining a stress function that satisfies the yield criteria, stress boundary conditions and continuity of stress field at the elastic plastic interface. The crack-tip blunting affect is incorporated in the analysis.

In chapter 7, the stress function approach is extended to derive stress field for elastic-perfectly-plastic material. In this chapter the same plastic zone formulation is followed. However, to get solution in terms of stress intensity factor K_I, the proposed plastic model is reconciled with classical LEFM solution (Sahoo et al. 2008). The Von Mises condition (Eq. 7.13) is considered as yielding criterion in the process zone. The following stress boundary conditions are satisfied:

1. Inside the plastic zone, the effective stress should equal to the yield stress of the material.

2. Experimental observations indicate blunting of the crack-tip in elastic-plastic materials. At the blunted crack-tip, (x_t), the normal stress component must be zero, i.e., $\sigma_{xx} = 0$. Thus, at the crack-tip the Von Mises yield criterion gives $\sigma_{yy} = \sigma_Y$.

3. At the elastic plastic interface along the crack line the solution should satisfy the continuity of the stress fields. In other words, the elastic stress field and plastic zone stress should have an unique value at the elastic-plastic interface. It is found from the analysis presented in chapter 7 that at the elastic plastic interface along the crack line, the stress σ_{yy} is slightly larger than σ_Y and the stress σ_{xx} is slightly smaller than σ_Y. However for small far field stress values $(S \ll \sigma_Y)$, the classical assumption of $\sigma_{xx} = \sigma_{yy} = \sigma_Y$ is valid. In present context, the LEFM solution is considered as the reference elastic solution and it is assumed that at the elastic-plastic interface (x_Y), $\sigma_{yy} = \sigma_{xx} = \sigma_Y$. This assumption is necessary to derive the peak stress magnitude and it's location in terms of stress intensity factor K_I.

4. Finally the load equilibrium condition should be maintained as explained in the Irwin's model (section 2.3.2).

Stress Field Solution

As discussed earlier, we consider the sum of stresses $\sigma_{xx} + \sigma_{yy}$ is analytic in the form

$$\sigma_{yy} + \sigma_{xx} = 2\ \sigma_Y\ f(x) \tag{8.3}$$

where $f(x)$ is any continuous function. The functional form of continuous function $f(x)$ is chosen similar to chapter 7 as

$$f(x) = \sin[p\ (x - x_0)] \tag{8.4}$$

where p and x_0 are real and unknown constants. Substituting Eq. 8.4 into Eq. 8.3 and using Von Mises yielding criterion (Eq. 7.13) gives

$$\sigma_{yy} = \sigma_Y \ \left\{ \sin[p(x - x_0)] + \frac{1}{\sqrt{3}} \cos[p(x - x_0)] \right\} \tag{8.5}$$

$$\sigma_{xx} = \sigma_Y \ \left\{ \sin[p(x - x_0)] - \frac{1}{\sqrt{3}} \cos[p(x - x_0)] \right\} \tag{8.6}$$

At crack-tip (x_t), substituting $\sigma_{xx} = 0$ and $\sigma_{yy} = \sigma_Y$ and solving gives

$$p(x_t - x_0) = \frac{\pi}{6} \tag{8.7}$$

At elastic-plastic interface (x_Y), substituting $\sigma_{xx} = \sigma_{yy} = \sigma_Y$ and solving gives

$$p(x_Y - x_0) = \frac{\pi}{2} \tag{8.8}$$

The size of plastic zone can be expresses in terms of constant p as

$$l_p = x_Y - x_t = \frac{p(x_Y - x_0) - p(x_t - x_0)}{p} = \frac{\pi}{3\ p} \tag{8.9}$$

To derive the value of p, the total load due to plastic stress in process zone is evaluated and equated with the total plastic zone load obtained from LEFM (sec-

tion 2.3.2) in terms of r_Y. $r_Y = x_Y - a_i$ and is given by the relation

$$r_Y = \frac{1}{2\pi}\left[\frac{K_I}{\sigma_Y}\right]^2 \tag{8.10}$$

where a_i = initial undeformed half crack length and $K_I = S\sqrt{\pi a}$. Thus, the total load is

$$P_y = \int_{x_t}^{x_Y} \sigma_{yy} dx = 2\ \sigma_Y\ r_Y \tag{8.11}$$

Substituting σ_{yy} from Eq. 8.5 into Eq. 8.11 and solving, we get

$$\frac{\sigma_Y}{p}\left\{\cos[p(x_t - x_0)] - \cos[p(x_Y - x_0)] + \frac{\{\sin[p(x_Y - x_0)] - \sin[p(x_t - x_0)]\}}{\sqrt{3}}\right\} = 2\sigma_Y r_Y \tag{8.12}$$

Now substituting Eq. 8.7 and 8.8 into Eq. 8.12 and using Eq. 8.10, we get

$$p = \frac{1}{\sqrt{3}\ r_Y} = \frac{2\pi}{\sqrt{3}}\left(\frac{\sigma_Y}{K_I}\right)^2 \tag{8.13}$$

Further substituting the value of p from Eq. 8.13 in to Eq. 8.9 and using Eq. 8.10, we obtain the length of the process zone as

$$l_p = \frac{\pi}{3\ p} = \frac{\pi}{\sqrt{3}} r_Y = \frac{1}{2\sqrt{3}}\left(\frac{K_I}{\sigma_Y}\right)^2 \tag{8.14}$$

Maximum stress

The peak stress value (σ_{yy}^{peak}) can be derived by differentiating σ_{yy} (Eq. 8.5) and equating to zero

$$\frac{\partial}{\partial x}\sigma_Y\left[\sin[p(x - x_0)] + \frac{1}{\sqrt{3}}\cos[p(x - x_0)]\right]\ dx = 0 \tag{8.15}$$

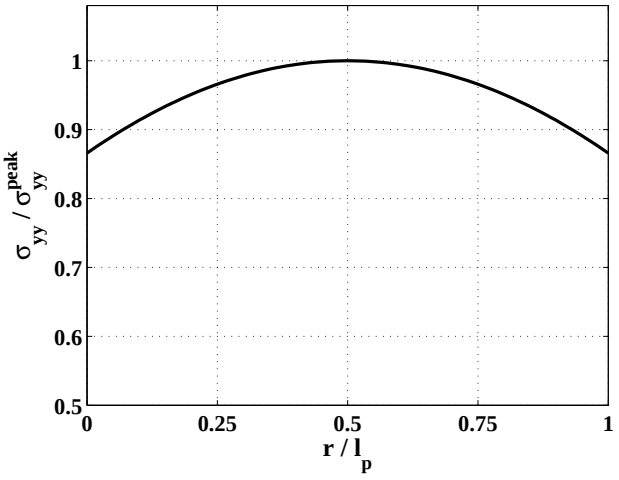

Figure 8.2: Variation of normalized stress ($\sigma_{yy}/\sigma_{yy}^{peak}$) with normalized distance (r/l_p) in the process zone demonstrating peak stress value and its location.

We assume that the peak stress occurs at $x = x_m$. Solving Eq. 8.15, we get $p(x_m - x_0) = \frac{\pi}{3}$, and substituting it back into the stress field, the peak stress value is derived as

$$\sigma_{yy}^{peak} = \sigma_Y \left\{ \sin\left(\frac{\pi}{3}\right) + \frac{1}{\sqrt{3}} \cos\left(\frac{\pi}{3}\right) \right\} = \frac{2}{\sqrt{3}} \sigma_Y \tag{8.16}$$

As we move from the crack tip to the elastic and process zone interface i.e. $x = x_t$ to $x = x_Y$, $p(x - x_0)$, the following variation is noted: $p(x_t - x_0) = \frac{\pi}{6}$ to $p(x_Y - x_0) = \frac{\pi}{2}$. Hence, the peak stress occurs at the center of the process zone ahead of the crack tip, and the critical distance is given by

$$r_c = \frac{l_p}{2} = \frac{1}{4\sqrt{3}} \left(\frac{K_I}{\sigma_Y} \right)^2 \tag{8.17}$$

Figure 8.2 shows the variation of stress (σ_{yy}) in the process zone.

8.2.3 Compressive Hydride Stress

Precipitation of hydrides in zirconium alloy increases the volume of the metal, which generates a compressive stress in the matrix. Zirconium hydride is formed in the vicinity of the crack-tip as platelets (Yuan 1982). In the absence of an externally applied stress, hydride platelets generate a stress free strain ($\epsilon_\perp$) normal to the disk shaped platelet while all other components being zero. This strain ($\epsilon_\perp$) is a material parameter (Eadie et al. 1989). A simple expression for the compressive hydride stress, σ^h is given by Shi and Puls (1994) and Wappling et al. (1997) as a function of distance from the crack-tip (r) as follows

$$\sigma^h(r) = -\frac{E\epsilon_\perp}{4\pi(1-\nu^2)}\frac{t}{r} \qquad r \geq 0.25t \tag{8.18}$$

where t is the thickness of hydride platelets.

8.2.4 Hydride Fracture Stress

Due to difficulty in experimentation, there are no data available to predict fracture stress of hydride and its dependence on the temperature. Leitch and Puls (1992) suggested a lower-bound value for the fracture stress of a hydride platelet ranging from 600 to 550 MPa between the ambient temperature and 100^0C, respectively. Shi and Puls (1994) assumed that the fracture strength of a brittle material like Zirconium hydride is related to its bond strength and hence related to the magnitude of modulus of elasticity (E). They provided a simple expression for fracture stress in terms of E as follows

$$\sigma_f^h = 7.357 \times 10^{-3} E \tag{8.19}$$

Since, we don't have any information about modulus of elasticity of solid Zirconium hydrides, we use the E as the modulus of elasticity of Zr-2.5%Nb alloy.

8.3 Derivation of K_{IH}

The threshold condition for DHC initiation is

$$\sigma_{yy}^{peak} + \sigma^h(r_c) = \sigma_f^h \tag{8.20}$$

where σ_{yy}^{peak} is the peak applied stress inside the process zone and it's value is given in Eq. 8.16. The compressive stress inside hydride at the critical distance (r_c) from the crack-tip is expressed in terms of stress intensity factor K_I by substituting Eq. 8.17 into Eq. 8.18.

$$\sigma^h(r_c) = -\frac{\sqrt{3}\ E\ \epsilon_\perp t}{\pi\ (1-\nu^2)} \left(\frac{\sigma_Y}{K_I}\right)^2 \tag{8.21}$$

and the effective local stress at critical location is then expressed substituting Eq. 8.16 and Eq. 8.21 into Eq. 8.1 as

$$\sigma_{local}(r_c) = \frac{2}{\sqrt{3}}\sigma_Y - \frac{\sqrt{3}\ E\ \epsilon_\perp t}{\pi\ (1-\nu^2)} \left(\frac{\sigma_Y}{K_I}\right)^2 \tag{8.22}$$

Figure 8.3 shows the effective local stress values for a range of of K_I and t. Other parameter used in the calculation are given in Table 8.1. It can be seen form figure 8.3 that, at low K_I and high t values, the effective local stress inside the hydride for a Zr-2.5%Nb alloy is below the fracture stress σ_f^h. Even effective local stress is negative for low K_I and high t value. When K_I increases and t decreases,

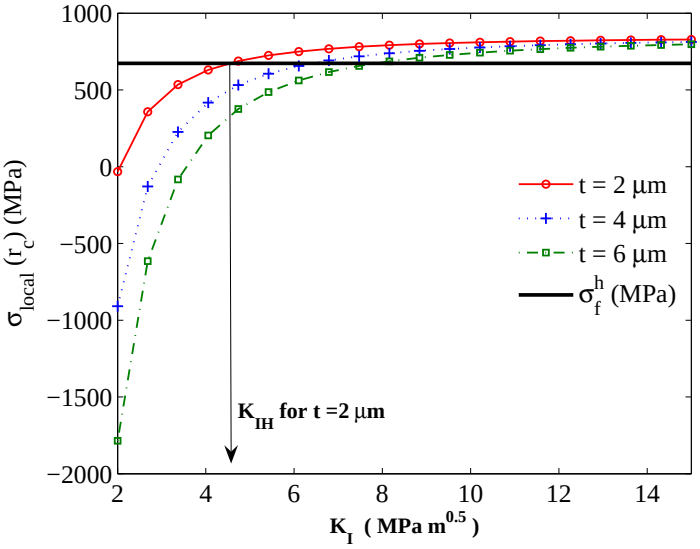

Figure 8.3: Variation of effective local stress with K_I and thickness of hydride platelet at 350^0K Temperature

the effective applied stress increases. At a constant t value for sufficiently high K_I, the maximum local stress reaches the point where σ_f^h is exceeded. This is the necessary condition for DHC initiation. At the threshold condition for DHC initiation ($K_I = K_{IH}$), Eq. 8.20 is satisfied. An analytical expression for the threshold stress intensity factor is derived satisfying the condition of local fracture criterion by substituting Eq. 8.22 and condition $K_I = K_{IH}$ at the threshold into Eq. 8.20 as follows

$$K_{IH} = \sigma_Y \sqrt{\frac{3\ E\ \epsilon_\perp\ t}{\pi(1-\nu^2)(2\sigma_Y - 12.7427 \times 10^{-3} E)}} \tag{8.23}$$

8.4 Results

Experimental results reported in the literature suggest that K_{IH} increases slightly with increasing temperature. On average, K_{IH} varies from 5 to 10 MPa$\sqrt{m}$ for

Table 8.1: Mechanical properties of Zr-2.5%Nb alloy (Shi et al. 1994, Eadie et al. 1989)

$E = 95900 - 57.4\{T(K) - 273\}$ MPa
$\nu = 0.436 - 4.8 \times 10^{-4}\{T(K) - 300\}$
$\epsilon_{\perp} = 0.072$
$\sigma_Y = 1088 - 1.02 \times T(K)$ MPa
$\sigma_f^h = 7.357 \times 10^{-3} \times E$

temperature ranging from 350 to 500 K (Sawatzky 2000, Shi et al. 1994).

From the proposed expressions for K_{IH} (Eq. 8.23), we infer that (1) K_{IH} increases as $\sqrt{t}$, and (2) K_{IH} dependent on the yield stress (σ_Y).

Shek et al. (1996) reported that the thickness of hydride increase with temperature. Therefore, the temperature dependent hydride thickness must be included in the analytical expression (Eq. 8.23) in predicting K_{IH}. Kim et al. (2000) suggested that the hydride thickness increases with decreasing yield stress and Young's modulus of elasticity or with an increasing temperature. We interpolated values of hydride thickness corresponding to different temperatures from (Kim et al. 2000) for plane stress condition, which are plotted in figure 8.4.

We considered the hydride thickness variation with temperature (Fig. 8.4) in Eq. 8.23. Finally, using the proposed model K_{IH} values as a function of temperature were computed, and results are presented in Table 8.2.

Experimental range of K_{IH} values is 5 to 10 $MPa\sqrt{m}$ at temperature ranging from 350 to 500 K is reported in the literature (Shi et al. 1994). The comparison of the proposed model with available experimental data (Shi et al. 1994) is shown in figure 8.5. It shows that the predicted K_{IH} values are in closer agreement with the data and they also exhibit qualitative relation between K_{IH} and temperature.

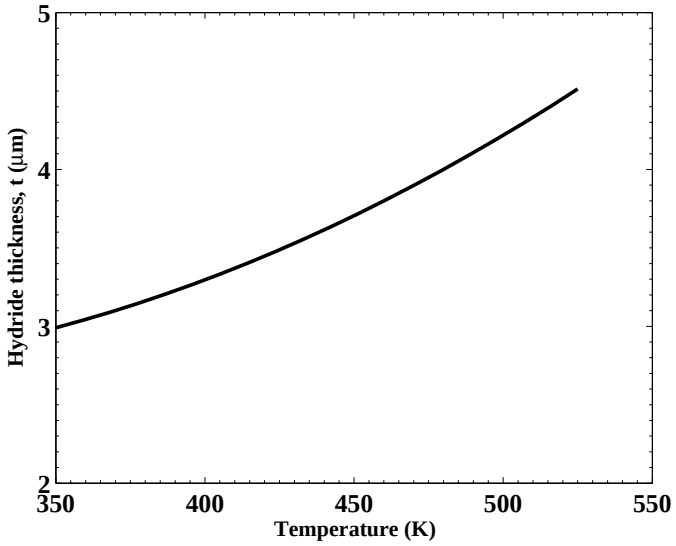

Figure 8.4: Temperature dependence of the hydride thickness precipitation in the process zone of un-irradiated Zr-2.5Nb alloys for plane stress condition

Table 8.2: Predicted K_{IH} as a function of temperature

Temperature (K)	K_{IH} $(MPa\sqrt{m})$
300	6.1446
350	6.3920
400	6.8810
450	7.7596
500	9.5271

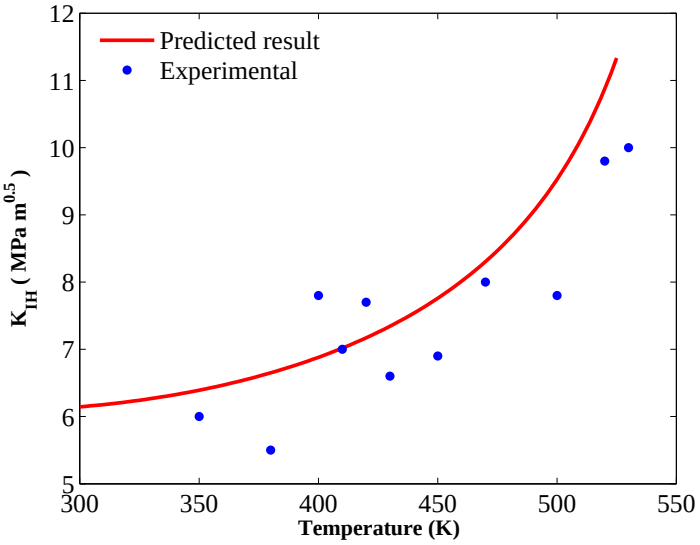

Figure 8.5: Comparison of predicted K_{IH} with experimental data

8.5 Conclusions

In this chapter, an analytical model is developed to predict threshold stress intensity factor (K_{IH}) for delayed hydride cracking initiation of Zr-2.5%Nb alloy. The model is derived by refining the derivation of plastic stress distribution in the process zone ahead of the crack-tip. Explicit analytical expression for K_{IH} is derived. The proposed solution depicts a relationship between K_{IH} and temperature that is consistent with experimental results. This model is expected to be useful in the probabilistic assessment of DHC initiation in PTs.

Chapter 9

Conclusions and Recommendations

9.1 Conclusions

The thesis presents probabilistic and stress field models for assessment of flaws in pressure tubes (PTs) that constitute the core of a CANDU reactors. The associated conservatism in a deterministic assessment procedure is discussed and probabilistic models are formulated. The sampling uncertainty associated with any probabilistic assessment procedure is investigated and a risk-informed approach is presented to investigate the required flaw sample size for inspection. In the later part of the thesis, the crack induced stress distribution is investigated considering the effect of blunting. The study covers both elastic and elastic-perfectly-plastic materials. The critical condition for DHC initiation from a flaw is also studied and an analytical model is formulated to derive the threshold stress intensity factor for DHC initiation.

The thesis formulates explicit limit state equations for probabilistic assessment of flaws in PTs. The probabilistic formulation covers DHC initiation assessment and Leak-Before-Break assessment. The proposed formulation of explicit limit state equation is helpful in employing first order reliability method for computation, which is highly efficient over the simulation method. In addition, important information regarding design point values of the variables is also obtained.

The thesis presents an innovative, semi-probabilistic method for DHC initiation and leak-before-break assessment that bridges the gap between a simple deterministic analysis and complex simulations. In the proposed method semi-probabilistic assessment equations corresponding to target reliability are formulated by using the corresponding calibrated partial factors. Partial factors are computed for a range of target probabilities of DHC initiation and break-before-leak. Since the calibration process accounts for interaction among random variables and their sensitivity to the assessment criterion, probabilistic bounds are consistent with a specified reliability level, whereas bounds chosen heuristically or based on experience will lack this consistency.

The CSA standard specifies the number of pressure tube samples to be inspected during a periodic in-service inspection without considering the possible sampling error. The thesis presents a risk informed strategy to flaw sample size determination during a scheduled in-service inspections. The sampling uncertainty associated with the probability computation is discussed and a two step (1) confirmatory and (2) explanatory approach is proposed to decide about the sample size requirement. The proposed approach is illustrated through an example of DHC initiation assessment. However, this approach can be followed for any other probabilistic assessment.

The thesis presents stress field models induced by a central notch in an infinite linear elastic plate subjected to generalized biaxial loading condition by using a

solution associated with the final deformed shape of the notch. The formulation allows the rotation near the notch-tip leading to blunting and displacement of the tip. The analysis yields non-singular crack-tip stress field and a non-linear variation of stress concentration factor. For sharp notches, the change in notch-tip curvature, during loading, is found to be significant. Thus, for sharp notches and cracks, the stress field relations in terms of final notch-tip geometry is recommended. For a sharp crack subjected to uniaxial loading, the crack tip stresses are found to be finite and constant i.e. $\sigma_{yy}^{A} = E$ irrespective of the initial dimension.

The thesis presents a solution to stress and deformation field induced by a central crack in an infinite elastic-perfectly-plastic plate considering the effect of blunting. The problem is solved by reconciling the plastic zone stress field with the elastic stress field similar to classical Irwin's model. The plastic zone stress field is formulated by defining an analytical function that satisfies the Von Mises yield criterion. The elastic stress field is based on the elastically deformed crack geometry. The plastic zone size computed using the proposed model is smaller than the classical result. The proposed model yields non-singular stress field at the crack-tip and a non-linear variation of stress concentration factor inside the plastic zone. However, LEFM based Irwin's model assumes constant stress equal to the yield limit of the material throughout the plastic zone. Though, the stress distribution inside plastic zone depends on the far field stress value S, the peak stress value (σ_{yy}^{peak}) is almost constant and depends only on the yield stress of the material.

The thesis presents an analytical model to predict threshold stress intensity factor (K_{IH}) for delayed hydride cracking initiation of Zr-2.5%Nb alloy. Explicit analytical expression for K_{IH} is derived. The proposed solution depicts a relationship between K_{IH} and temperature that is consistent with experimental results.

Although the probabilistic models presented in the thesis is based on specific cases of DHC and leak-before-break assessment, they are generic, and can be adopted to any other probabilistic assessment. The proposed stress field models generalizes the crack-tip stress distribution and the effects of plasticity. These models presents a basis for condition assessment and safety evaluations of any cracked elements.

9.2 Recommendations for Future Research

The probabilistic formulation of DHC initiation presented in the thesis is for planar flaws. Similar formulation can be done for assessment of volumetric flaws.

The probabilistic models developed in the thesis computes conditional probability assuming the presence of sufficient hydrogen required for DHC initiation from a flaw. Development of probabilistic model to compute the probability of critical hydrogen concentration in a pressure tube needs further research.

The semi-probabilistic assessment equations for leak-before-break assessment proposed in the thesis considers a deterministic initial penetration length of the flaw as recommended in CSA deterministic approach. However, the initial penetration length is expected to be a random variable. In future, this can be considered as a random variable and partial factors can also be assigned to it.

The stress field formulation presented in the thesis is for linear elastic and elastic-perfectly-plastic material. The model is based on the deformed configuration allowing crack-tip rotation and blunting. Based on similar reasoning, future research work is needed to investigate the flaw induced stress field for strain hardening materials.

References

Allen, T.M., Nowak, A.S. and Bathurst, R.J. (2005). "Calibration to determine load and resistance factors for geotechnical and structural safety." TRB Circular E-C079, *Trasportation Research Board*, Washington, D.C.

Anderson, T.L. (1995). *Fracture Mechanics: Fundamentals and Applications*. CRC Press, Second edition.

Ang, A.H.-S. and Tang, W.H. (1975). *Probability Concepts in Engineering Planning and Design, Vol. II, Decision Risk and Reliability*. John Wiley & Sons.

Ayyub, B.M. and Beach, R.H. (1995). "Methodology for the development of reliability based design criteria for surface ship structures." *Naval Engineers Journal*, ASNE 107 (1), pp. 45-61.

Bahurmuz, A.A., White, A.J., Urbanic, V.F. and McDougall, G.M. (1993). "Modeling Deuterium Buildup in the Rolled Joint Region of CANDU Fuel Channels." *International conference on Expanded and Rolled joint Technology*, Toronto, Canada.

Barenblatt, G.I. (1962). "The Mathmatical Theory of Equilibrium Cracks in Brittle Fracture." *Advances in Applied Mechanics*, Vol. VII, Academmic Press, pp. 55-129.

Barlow, R.E. and Proschan, F. (1981). *Statistical Theory of Reliability and Life Testing: Probablity Models To Begin With.* Silver Spring.

Benjamin, J.R., Cornell, C.A. (1970). *Probability, Statistics and Decision for Civil Engineers.* McGraw-Hill Book company.

Burdekin, F.M., Stone, D.E.W (1966). "The Crack Opening Displacement Approach to Fracture Mechanics in Yielding Materials." *Journal of Strain Analysis*, Vol. 1, pp .145-153.

Castanier, B., Grall, A. and Berenguer, C. (2005). "A Condition-based Maintenance Policy with Non-periodic Inspections for a Two-unit series system." *Reliability Engineering and System Safety*, Vol. 87, pp. 109-120.

CAN/CSA-N285.4 (1994). "Periodic inspection of CANDU Nuclear power plant components."

CAN/CSA-N285.8 (2005). "Technical requirements for in-service evaluation of Zirconium alloy pressure tubes in CANDU reactors."

Christodoulou, N., Causey, A.R., Holt, R.A., Tome, C.N., Badie, N., Klassen, R.J., Sauve, R. and Woo, C.H. (1996). "Modeling In-Reactor Deformation of Zr-2.5 Nb Pressure Tubes in CANDU Power Reactors." *Zirconium in the Nuclear Industry: Eleventh International Symposium*, ASTM STP 1295, American Society for Testing and Materials, pp. 518-537.

Creager, M., Paris, P.C. (1967). "Elastic field equations for blunt cracks with reference to stress corrosion cracking." *Int. J. of Fracture Mechanics*, Vol. 3, pp. 247-251.

Coleman, C.E. and Hardie, D. (1966). 'The hydrogen embrittlement of $_{\alpha}$-Zirconium - A review." *Journal of less-common metals II*, pp. 168-185.

Daniel, W.W. (1990). *Applied Nonparametric Statistics.* Advanced series in statistics and Decision sciences, PWS-KENT Publishing company, Boston, Second edition.

Desu, M.M., Raghavrao, D. (1990). *Sample size methodology.* Academic press Inc, Sandiego, CA.

Desu, M. M., Raghavrao, D. (2004). *Nonparametric Statistical Methods for Complete and Censored Data.* Chapman & Hall, New York Washington D.C.

Ditlevsen, O. (1979). "Narrow Reliability Bounds for Structural Systems." *Journal of Structural Mechanics*, Vol. 7 (4), pp. 435-451.

Dubey, R.N. and Sauve, R.G. (1992) "Numerical investigation of rate constitutive equations under finite deformation." *Nuclear Engineering and Design*, Vol. 135, pp. 249-266.

Dugdale, D.S. (1960). "Yielding in Steel Sheets Containing Slits." *Journal of Mechanics and Physics of Solids*, Vol. 8, pp. 100-104.

Eadie, R.L. and Ellyin, F. (1989). "The effect of hydride precipitation on the stresses near the crack tip in a delayed hydride crack in Zirconium-2.5% Niobium." *Scripta Mettalurgica*, Vol. 23, pp. 585-592.

Freudenthal, A.M. (1947). "The safety of strucutres." *Transactions ASCE*, Vol. 112, pp 125-180.

Gertsbakh, I.B. (2000). *Reliaibility Theory with Application to Preventive Maintenance*. Springer-Verlag, Berlin.

Gertsbakh, I.B. (1989). *Statistical Reliability Theory*. Marcel Dekker, NY.

Glinka, G. (1985). "Calculation of inelastic notch-tip strain-stress histories under cyclic loading." *Engineering Fracture Mechanics*, Vol. 22, pp. 839-854.

Griffith, A.A. (1920). "The Phenomena of Rupture and Flow in Solids." *Philosophical Transactions*, series A, Vol. 221, pp. 163-198.

Gupta, A. and Choi, B. (2003). "Reliability-based load and resistance factor design for piping: an explanatory case study." *Nuclear Engineering and Design*, Vol. 224, pp. 161-178.

Han, B.K. and Ang, A.H.-S. (1998). "Serviceability design load factors and reliability assessments for reinforced concrete containment structures." *Nuclear Engineering and Design*, Vol. 179, pp. 201-208.

Hohenbichler, M. and Rackwitz, R. (1983). "First Order Concepts in System Reliability." *Journal of structural safety*, Vol. 1, pp. 177-188.

Hoyland, A., Rausand, R. (1994). *System Reliability Theory: Models and Statistical Methods*. John Wiley & Sons Inc.

Hutchinson, J.W. (1968). "Singular Behavior at the End of a Tensile Crack Tip in a Hardening Material." *Journal of Mechanics and Physics of Solids*, Vol. 16, pp. 13-31.

Inglis, C.E. (1913). "Stresses in a Plate Due to the Presence of Cracks and Sharp Corners." *Trans. of the Institute of Naval Architects*, Vol. 55, pp. 219-241.

IAEA (1998). *Assessment and Management of Ageing of Major Nuclear Power Plant Components, Important to Safety: CANDU Pressure Tubes*. International Atomic Energy Agency, IAEA-TECDOC-1037.

IAEA (2001). *Assessment and Management of Ageing of Major Nuclear Power Plant Components, Important to Safety: CANDU Reactor Assemblies*. International Atomic Energy Agency, IAEA-TECDOC-1197.

International Atomic Energy Agency (2004). *Delayed Hydride Cracking in Zirconium Alloy Pressure Tube in Nuclear Reactors*. IAEA-TECDOC-1410.

Irwin, G.R. (1957). "Analysis of Stresses and Strains near the end of a Crack Traversing a Plate." *Journal of Applied Mechanics*, Vol. 24, pp. 361-364.

Jiao, G., and Moan, T. (1992). "Relaibility-based fatigue and fracture design criteria for welded offshore structures." *Engineering Fracture Mechanics*, Vol. 41 (2), pp. 271-282.

Johnson, N., and Kotz, S. (1972). *Distributions in statistics: continuous multivariate distributions*. New York, John Wiley & Sons Inc.

Kapur, K.C., Lamberson, L.R. (1977). *Reliability in Engineering Design*. John Wiley & sons, New York.

Kim, Y.S., Matvienko, Y.G., Cheong, Y.M. and Kwon, S.C. (2000). "A model of the threshold stress intensity factor, K_{IH}, for delayed hydried cracking of Zr-2.5Nb alloy." *Journal of Nuclear Materials*, Vol. 278, pp. 251-257.

Kwak, S.L., Lee, J.S., Kim, Y.J. and Park, Y.W. (2005). "Sensitivity Analysis of Input Parameters for Pressure Tube Integrity Evaluation." *Nuclear Engineering and Design*, Vol. 235, pp. 1909-1918.

Lawless, J.F. (2003). *Statistical Models and Methods for Life time Data*. John Wiley and Sons, Second edition.

Leitch, B.W. and Puls, M.P. (1992). "Finite element calculations of the accommodation energy of a misfitting precipitate in an elastic-plastic matrix." *Metallurgical Transactions* A, Vol. 23, pp. 797-806.

Luo, L.G., Embury, J.D. (1988). "An investigation of crack blunting processes under plane strain conditions." *Engineering Fracture Mechanics*, Vol. 30, pp. 177-190.

Love, A.E.H. (1927). *A treatise on the mathematical theory of elasticity*. 4th edition, Cambridge.

Madsen, H.O., Krenk, S., and Lind, N.C. (1986). *Methods of Structural Safety*. Prentice-Hall.

Maugis, D. (1992). "Stresses and displacements around cracks and elliptical cavities:Exact solutions." *Engineering Fracture Mechanics*, Vol. 43, pp. 217-255.

McMeeking, R.M. and Parks, D.M. (1979). "On Criteria for J-Dominance of Crack Tip Fields in Large-Scale Yielding." ASTM STP 668, *American Society for Testing of Materials*, Philadelphia, pp. 175-194.

Meeker, W.Q. and Escobar, L.A. (1998). *Statistical Methods for Reliability Data*. John Wiley & Sons.

Melchers, R.E. (1999). *Structural Reliability Analysis and Prediction.* John Wiley & Sons, Chichester, Second edition.

Mirza, S.A. (1996). "Reliability based design of reinforced concrete columns." *Structural Safety*, Vol. 18, pp. 179-194.

Moan, G.D., Coleman, C.E., Price, E.G., Rodgers D.K. and Sagat, S. (1990). "Leak-Before-Break in the Pressure Tubes of CANDU Reactors." *International Journal of Pressure Vessel and Piping*, Vol. 43, pp. 1-21.

Mori, Y. and Kato, T. (2003). "Multi-normal Integrals by Importance Sampling for Series System Reliability." *Journal of Structural Safety*, pp. 363-378.

Muskhelishvili, N.I. (1975). *Some Basic Problems of the Mathematical Theory of Elasticity.* Noordhoff, Leyden.

Nowak, A.S. (1983). "Risk analysis for code calibration." *Structural Safety*, Vol. 1, pp. 289-304.

Nowak, A.S. (1995). "Calibration of LRFD bridge code." *Journal of Structural Engineering*, Vol. 121, No. 8, pp. 1245-1251.

Nowak, A.S. and Collins, K.R. (2000). *Reliability of structures.* McGraw-Hill, New York, 2000.

Nowak, A.S. and Eamon, C.D. (2005). "Load and resistance factor calibration for wood bridges." *Journal of Bridge Engineering*, Vol. 10, No. 6, pp. 636-642.

Nowak, A.S. and Lind, N.C. (1979). "Practical procedures for code calibration." *Canadian Journal of Civil Engineering*, Vol. 6, pp. 112-119.

Nowak, A.S., Park, C.-H. and Ojala, P. (2001). "Calibration of design code for buried structures." *Canadian Journal of Civil Engng.*, Vol. 28, pp. 574-582.

Ochi, M.K. (1989). *Applied Probability and Stochastic Processes: In engineering and Physical Sciences.* Wiley series in probability and mathematical statistics, John Wiley & Sons.

Pachener, J. (2002). "Overview of IAEA Project on Safety Aspects of NPP Ageing." *IAEA Technical Meeting on Enhanced NPP Safety, Performance and Life Extension through Effective ageing Management*, Vienna.

Panayotounakos, D.E. and Zisis, B. (1989). "Closed-form solutions of the nonlinear prtial differential equations governing the stress-field in a rigid, perfectly-plastic body." *SIAM J. of Applied Mathematics*, Vol. 49 (5), pp. 1374-1389.

Pandey, M.D. (1998). "An Effective Approximation to Evaluate Multi-normal Integrals." *Journal of Structural Safety*, Vol. 20, pp. 51-67.

Pandey, M.D. and Sahoo, A.K. (2009). "A Risk-Informed Approach to Leak Before Break Assessment of Pressure Tubes in CANDU Reactors." *Journal of Pressure Vessel Technology*, American Socity of Mechanical Engineers. (Accepted)

Park, Y.W., Kang, S.S. and Han, B.S. (2002). "Structural Integrity Assessment of Pressure Tubes for Wolsong Unit-1 Based on Operational Profile." *Nuclear Engineering and Design*, Vol. 212, pp. 41-48.

Parker, A.P. (1981). *The Mechanics of Fracture and Fatigue: An Introduction.* E. & F. N. Spon. Ltd.

Puls, M.P. (1997). "Assessment of Aging of Zr-2.5Nb Pressure Tubes in CANDU Rectors." *Nuclear Engineering and Design*, Vol. 171, pp. 137-148.

Puls, M.P., Wilkins, B.J.S., Rigby, G.L., Mistry, J.K. and Sedran, P.J. (1998). "A Probabilistic Method for Leak-before-break Analysis of CANDU Reactor Pressure Tubes." *Nuclear Engineering and Design*, Vol. 185, pp. 241-248.

Ramachandran, K. (1984). "System Bounds: A Critical Study." *Journal of Civil Engineering Systems*, 1984, Vol. 1, pp. 123-128.

Ranganathan, R. (1999). *Structural Reliability Analysis and Design*. Jaico Publishing house, Mumbai.

Rice, J.R. (1968). "A Path Independent Integral and the Approximate Analysis of Strain Concentration by Notches and Cracks." *Journal of Applied Mechanics*, Vol. 35, pp. 379-386.

Rice, J.R., and Rosengren, G.F. (1968). "Plane Strain Deformation near a Crack Tip in a Power law Hardening Material." *Journal of Mechanics and Physics of Solids*, Vol. 16, pp. 1-12.

Sagat, S., Shi, S.Q. and Puls, M.P. (1994). "Crack initiation criterion at notches in Zr-2.5Nb alloys." *Materials Science and engineering*, Vol. A176, pp. 237-247.

Sagat, S., Chow, C.K., Puls, M.P. and Coleman, C.E. (2000). "Delayed Hydride Cracking in Zirconium Alloys in a Temperature Gradient." *Journal of Nuclear Materials*, Vol. 279, pp. 107-117.

Sahoo, A.K., Pandey, M.D. (2005). "Risk based component importance measure for life cycle management of infrastructure systems." *International Conference*

on Reliability and Safety Engineering, INCRESE 05, Bhubaneswar, India, pp. 635-644.

Sahoo, A.K., Dubey, R.N. and Pandey, M.D. (2006). "Crack-tip plasticity and its effects on stress and deformation field in an ideal elastic, rigid-plastic material." *International Conference on Mathmatical Modeling and Computer Simulation*, ICMMACS 06, LNMIIT, Jaipur, India.

Sahoo, A.K., Dubey, R.N. and Pandey, M.D. (2007a). "Crack-tip stress and deformation model for elastic, rigid-plastic material." *International Symposium on Plasticity and Impact Mechanics*, IMPLAST 07, Ruhr-University Bochum, Germany, pp. 401-408.

Sahoo, A.K., Dubey, R.N. and Pandey, M.D. (2007b). "Crack tip stress and deformation field." *19th International Conference on Structural Mechanics in Reactor Technology*, Transactions, SMiRT 19, Paper # B02/2, Toronto, Canada, pp. 1-8.

Sahoo, A.K., Pandey, M.D. (2009). "A Risk-Informed Approach to the Assessment of DHC Initiation in Pressure Tubes." *30th Annual Conference of the Canadian Nuclear Society* , CNS 2009, Calgary, Alberta, Canada. (Accepted)

Sahoo, A.K., Pandey, M.D. and Dubey, R.N. (2008). "An analytical model of the threshold stress intensity factor (K_{IH}) for DHC." *3rd Canadian Conference on Nonlinear Solid Mechanics*, CanCNSM 2008, Toronto, Canada, pp. 273-282.

Santhanam, A.T. and Bates, R.C. (1979). "The influence of notch-tip geometry on the displacement of stress and strain." *Material Science and Engineering*, Vol. 41, pp. 243-250.

Sawatzky, A. and Ells, C.E. (2000). "Understanding hydrogen in zirconium." *Twelfth international symposium*, ASTM STP 1354, pp. 32-48.

Sawatzky, A. (1985). "Formation of Hydride Blister in Zirconium Alloy Pressure Tubes." *Canadian Metallurgical Quarterly*, Vol. 3, pp. 227-234.

Schijve, J. (1980). "Stress gradient around notches." *Materials and Structures*, Vol. 3, pp. 325-338.

Sehgal, R., Tiwari, A. and Sood, V. (1985). "A study on fitness-for-service assessment for crack-like defects and corrosion in nuclear reactor pressure tubes." *Reliability Engineering and System Safety*, Vol. 89, pp. 227-235.

Shi, S.Q. and Puls, M.P. (1994). "Criteria for fracture initiation at hydrides in zirconium alloys I. Sharp crack tip." *Journal of Nuclear materials*, Vol. 208, pp. 232-242.

Shek, G.K., Jovanovic, M.T., Seahra, H., Ma, Y., Li, D. and Eadie, R.L. (1996). "Hydride morphology and striation formation during delayed hydride cracking in Zr-2.5% Nb." *Journal of Nuclear Materials*, Vol. 231, pp. 221-230.

Singh, M.N.K., Dubey, R.N., Glinka, G. (1994). "Notch and Crack analysis as a moving boundary problem." *Engineering Fracture Mechanics*, Vol. 47 (4), pp. 479-492.

Singh, R.N., Kumar, N., Kishore, R., Roychaudhury, S., Sinha, T.K., and Kashyap, B.P. (2002). "Delayed Hydride Cracking in Zr-2.5 Nb Pressure Tube Material." *Journal of Nuclear Materials*, Vol. 304, pp. 189-203.

Singh, R.N., Kishore, R., Sinha, T.K., and Kashyap, B.P. (2002). "Hydride Blister Formation in Zr-2.5 wt % Nb Pressure Tube Alloy." *Journal of Nuclear materials*, Vol. 301, pp. 153-164.

Sneddon, I.N. (1946). "The distribution of Stress in the Neighbourhood of a Crack in an Elastic Solid." *Proceedings of Royal Society of London*, Vol. A-187, pp. 229-260.

Stevenson, A.C. (1945). "Complex potentials in two-dimensional analysis." *Proceedings of Royal Society*, Vol. A184, pp. 129-179.

Song, J. and Der Kiureghian, A. (2002). "Bounds on System Reliability by Linear Programming." *Journal of Engineering Mechanics*, Vol. 129 (6), pp. 627-636.

Tang, L. K. and Melchers, R. E. (1987). "Improved Approximation of Multinormal Integral." *Journal of Structural Safety*, Vol. 4, pp. 81-93.

Theocaris, P.S. (1986). "The exact form and properties of the deformed transverse internal elastic crack." *Engineering Fracture Mechanics*, Vol. 23, pp. 851-862.

Theocaris, P.S., Pazis, Z., Konstantellos, B.D. (1986). "The exact shape of a deformed internal slant crack under biaxial loading." *International Journal of Fracture*, Vol. 30, pp. 135-153.

Theocaris, P.S., Pazis, Z., Konstantellos, B.D. (1989). "Elastic displacements along the flanks of internal cracks in rubber." *Experimental Mechanics*, Vol. 29, pp. 32-39.

Thoft-Christensen, P. and Baker, M. J. (1982). *Structural Reliability and its Applications*. Springer-Verlag.

Timoshenko, S.P. and Goodier, J.N. (1970). *Theory of elasticity.* 3rd edition, McGraw-Hill, New York.

Walker, J.R. (1990). "A Probabilistic Approach to Leak-before-break in CANDU Pressure Tubes." *International Journal of Pressure Vessel and Piping*, Vol. 43, pp. 229-239.

Wäppling, D., Massih, A.R. and Ståhle, P. (1997). "A model for hydride-induced embrittlement in zirconium-based alloys." *Journal of Nuclear Materials*, Vol. 249, pp. 231-238.

Wells, A.A. (1961). "Unstable Crack Propagation in Metals: Cleavage and Fast Fracture." *Proceedings of the Crack Propagation Symposium*, Vol. 1, Paper 84, Cranfield, UK.

Wells, A.A. (1963). "Application of Fracture Mechanics at and Beyond General Yielding." *British Welding Journal*, Vol. 10, pp. 563-570.

Westergaard, H.M. (1939). "Bearing Pressure and Cracks." *Journal of Applied Mechanics*, Vol. 6, pp. 49-53.

Williams, M.L. (1957). "On the Stress Distribution at the Base of a Staionary Crack." *Journal of Applied Mechanics*, Vol. 24, pp. 109-114.

Wong, H. W., Bajaj, V. K., Moan, G. D., Huterer M. and Poidevin, C. O. (1990). "The Role of Leak-Before Break in Assessments of Flaws Detected in Candu Pressure Tubes." *International Journal of Pressure Vessel and Piping*, Vol. 43, pp. 23-37.

Yuan, X.Q. and Tangri, K. (1982). "Metallographic observations on the developing hydride morphology at the crack tip during hydrogen induced delayed cracking in a Zr-2.5Nb alloy." *Journal of Nuclear Materials*, Vol. 105, pp. 310-317.

Yuan, X. -X., Pandey, M. D. and Bickel, G. A. (2006). "A probabilistic degradation model for the estimation of the remaining life distribution of feeders." Nuclear Energy: A World of Service to Humanity, *27th Annual Conference of Canadian Nuclear Society*, Toronto, Ontario, Canada, June 11-14.